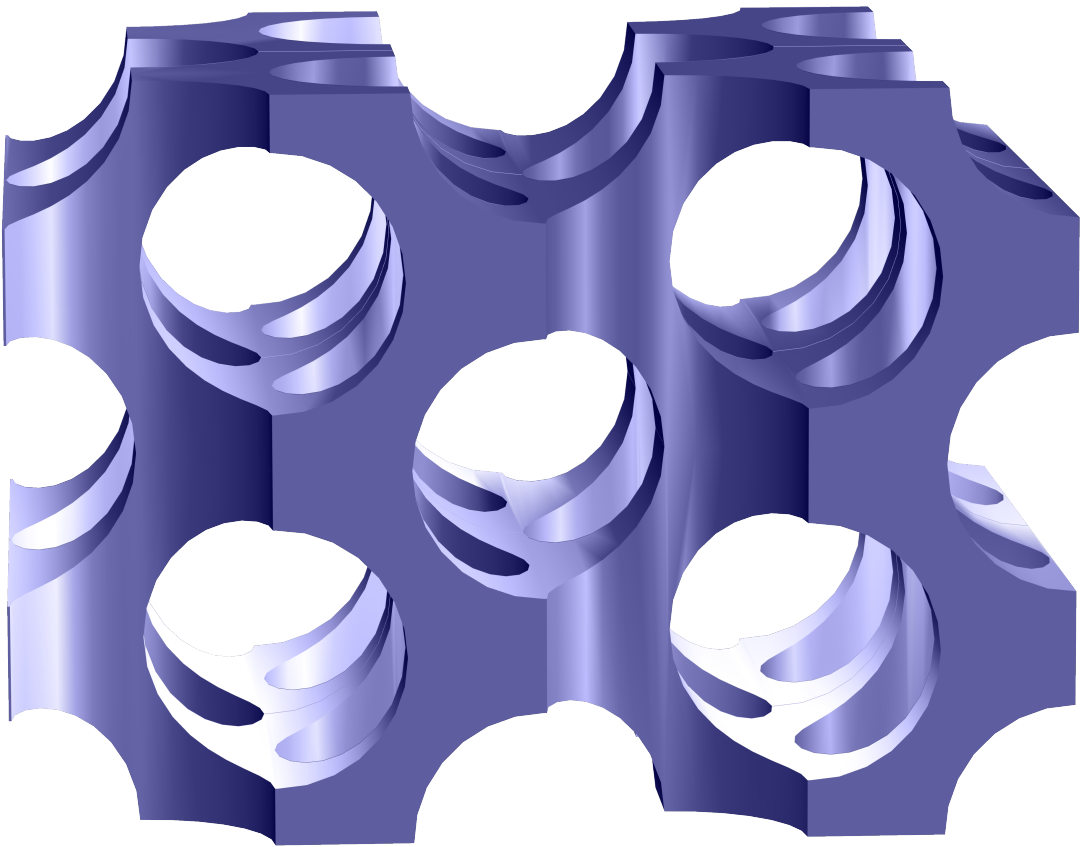# 3D
periodic photonic nanostructures with disrupted symmetries

Devashish

3D periodic photonic nanostructures with disrupted symmetries

3D periodieke fotonische nanostructuren met verstoorde symmetrieën

Cover
Schematic illustration of the $2 \times 2 \times 2$ supercell of a 3D inverse woodpile photonic crystal, which is a 3D periodic photonic nanostructure with disrupted symmetry. The cover is designed by Devashish.

Graduation Committee

Chairman   Prof. Dr. P.M.G. Apers (University of Twente)

Supervisors   Prof. Dr. Ir. J.J.W. van der Vegt (University of Twente)
                     Prof. Dr. W.L. Vos (University of Twente)

Members   Prof. Dr. K. Busch (Humboldt-Universität zu Berlin)
                     Prof. Dr. Ir. B. Koren (TU Eindhoven)
                     Prof. Dr. A. Lagendijk (University of Twente)
                     Prof. Dr. P.W.H. Pinkse (University of Twente)
                     Dr. G.H.L.A. Brocks (University of Twente)

3D PERIODIC PHOTONIC NANOSTRUCTURES WITH DISRUPTED SYMMETRIES

PROEFSCHRIFT

ter verkrijging van
de graad van doctor aan de Universiteit Twente,
op gezag van de rector magnificus,
Prof. Dr. T.T.M. Palstra,
volgens besluit van het College voor Promoties
in het openbaar te verdedigen
op vrijdag 15 december 2017 om 10.45 uur

door

Devashish

geboren op 17 januari 1990
te Muzaffarpur, Bihar, INDIA.

Dit proefschrift is goedgekeurd door de promotoren:

Prof. Dr. Ir. J.J.W. van der Vegt
Prof. Dr. W.L. Vos

To Mommy, who personifies the quote:
"You may see me struggle, but you will never see me quit".

Contents

CHAPTER 1

Introduction

1.1 Photonics

Light transcends all barriers, including those of geography, gender, age, culture, and racial origin [1]. It is a fundamental necessity for the existence of life on earth via photosynthesis. From the first ray of the sun shining into our eyes in the morning to the lamps eradicating the darkness at night, light is omnipresent [2, 3]. Light has been the cynosure of scientific research for centuries. Sir Isaac Newton discovered in the 17th century that white light actually consists of many colors of light [4] (*e.g.*, colors of the rainbow). To quote the Swiss painter Johannes Itten: *Color is life; for a world without color appears to us as dead. Colors are primordial ideas, the children of light.*

In the 20th century, Max Planck [5] and later Albert Einstein [6] proposed a theory for light with the dual nature of an electromagnetic wave as well as of a particle, which raised numerous eyebrows over how light can have two totally distinct characters simultaneously! This dual nature of light has been many times confirmed with experiments. The elementary particles of light are called "photons" and hence the science of light is known as Photonics. Photonics comprises the generation, control, and detection of light waves and photons. Photonics explores a wider variety of wavelengths from gamma rays to radio waves, called the electromagnetic spectrum, which includes X-rays, ultraviolet, visible light, infrared, and microwaves. Today, photonics is indispensable [1]: from electronics (barcode scanners, DVD players, television remote control, optical integrated circuits) to modern telecommunications (optical fibers for fast internet), to the health sector [7] (eye surgeries and medical instruments), to the manufacturing sector (laser cutting and 3D printing), to security (infrared camera and remote sensing), to entertainment (holography and laser show), and the list goes on.

1.2 Nanophotonics

Light propagation inside a homogeneous medium with a constant refractive index, such as in air or in a silicon wafer is described using the principles of geometrical optics, where light follows a rectilinear plane wave propagation [8]. However, an ensemble of microscopic pieces broken of a silicon wafer has a spatially rapidly changing refractive index and hence the light propagation strongly deviates from the rectilinear propagation due to optical interference [9]. The optical proper-

ties of these composite materials are now immensely different to those of the separate constituents. Composite dielectric optical materials, which have a spatially varying refractive index on length scales comparable to the wavelength of light, are known as complex or nanophotonic media [10–12]. Nanophotonic media uniquely define light propagation and control light-matter interactions because of their unique dispersion characteristics [13–18].

Two broad classifications of nanophotonic media distinguish disordered nanophotonic media, *i.e.*, a random arrangement of the constituent materials, from ordered nanophotonic media, *i.e.*, a periodic arrangement of the constituent materials. For daily household devices, disordered materials [19, 20] are used as the textured optical sheets in solar cells [21], phosphor plates in a white LED [22], or the diffuser glass window in bathroom.

Light propagation in ordered nanophotonic systems bears a strong resemblance to the wave propagation of a conducting electron in a crystalline solid [23–25]. Photonic crystals are a class of ordered nanophotonic structures and an optical analogue of semiconductors [25]. In photonic crystals, the refractive index varies spatially with a periodicity on length scales comparable to the wavelength of light. A careful selection of geometry, topology, and high-index backbone dielectric materials determines the optical properties of photonic crystals. Due to the long-range periodic order, the photonic dispersion relations are organized in bands, analogous to electron bands in a semiconductor [24]. When there is sufficient contrast between the refractive indices of the constituent materials in a photonic crystal and minimal absorption, then the interference of light from different interfaces can exhibit a similar phenomenon for photons (light modes) that the atomic potential produces for electrons [25]. For an infinite photonic crystal, light cannot propagate in a certain direction when the frequency is in a stop gap, as a result of Bragg diffraction [24]. Of prime significance to infinite photonic crystals is the emergence of a photonic band gap, a frequency range for which light is forbidden for all wave vectors and all polarizations [16, 17, 25]. There is a worldwide interest in three-dimensional (3D) photonic crystals that radically control both the propagation and emission of light [13, 16–18, 25, 27–29]. The application of 3D photonic crystals with a 3D photonic band gap includes controlling spontaneous emission of embedded quantum emitters [30–33] and cavity quantum electrodynamics (QED) [34, 35], controlling thermal emission [36, 37], realizing efficient miniature lasers [38], efficient photoelectric conversion in solar cells [39, 40], and cloaking [41].

1.3 3D inverse woodpile photonic crystals

Our research group fabricates and experimentally studies an important class of photonic crystals called 3D inverse woodpile photonic crystals, which have fascinated the nanophotonics community on account of their theoretically broad photonic band gap [42–44] typical of diamond structures. Such a broad 3D band gap is robust to disorder and fabrication imperfections, and the structure allows for conceptually convenient fabrication [45–52]. A 3D inverse woodpile crystal
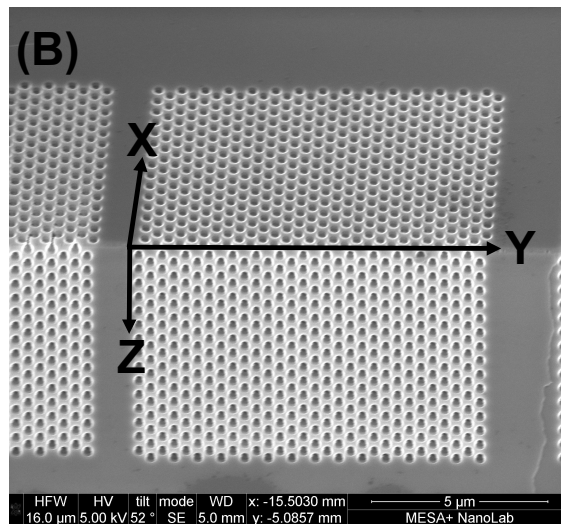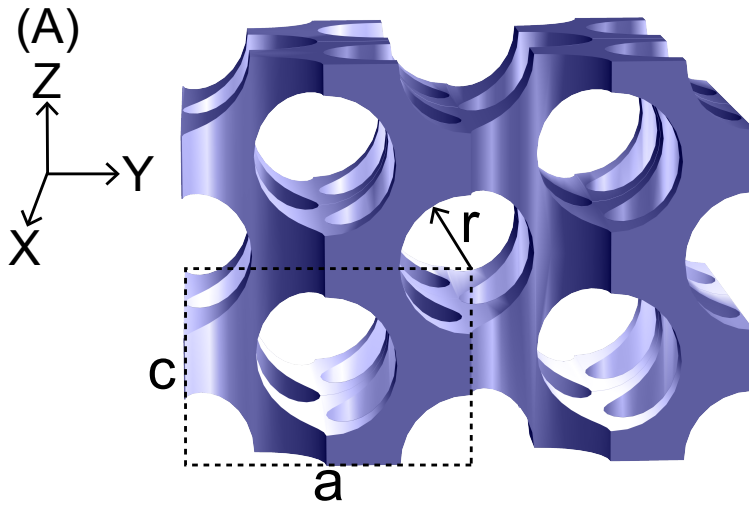
Figure 1.1: (A) Schematic illustration of the $2\times2\times2$ supercell of a 3D inverse woodpile photonic crystal with the XYZ coordinate axes. Two 2D arrays of identical pores with radius r are parallel to the X and Z axes. The lattice parameters for a tetragonal primitive unit cell are c and a. The lattice parameters have a ratio $\frac{a}{c} = \sqrt{2}$ and the pore radius is $\frac{r}{a} = 0.245$. The blue color indicates the high-index backbone of the crystal and the white color represents air. (B) Scanning electron microscopy (SEM) image of a 3D inverse woodpile photonic crystal fabricated in silicon. The typical radius of the pore is $r = 160$ nm and the lattice constant is $a = 680$ nm. The scale bar is shown in the image. SEM image courtesy of Cock Harteveld.

structure consists of two 2D arrays of identical pores with radius r, running in two orthogonal directions X and Z [42], as illustrated in the crystal design in Fig. 1.1 (A) and the real fabricated crystal in Fig. 1.1 (B). Each 2D array has a centered-rectangular lattice with lattice parameters c and a corresponding to $\{hkl = 110\}$ lattice planes in the conventional diamond structure [24]. When the lattice parameters have a ratio $\frac{a}{c} = \sqrt{2}$, the diamondlike structure is cubic. A cubic silicon inverse woodpile crystal with a high-index backbone having a dielectric permittivity $\epsilon = 12.1$, typical for silicon in the near infrared and telecom ranges [44, 53], has a broad maximum band gap width $\Delta\omega/\omega_c = 25.3\%$ relative to the central band gap frequency ω_c for pores with a relative radius $\frac{r}{a} = 0.245$ [43, 49]. Consequently, inverse woodpiles can potentially act as a broadband back reflector in a solar cell to enhance the distance light travels through internal reflections [54].

For a cubic inverse woodpile with lattice parameters c and a, Fig. 1.2 (i) shows the tetragonal primitive unit cell for the pore radius $\frac{r_1}{a} = 0.245$. This unit cell is periodic in all three directions X, Y, and Z. However, Fig. 1.2 (ii) reveals subtle "crescents" appearing at the front and the back interfaces in the XY view of the unit cell for the pore radius $\frac{r_1}{a} = 0.275$. Once the pore radius exceeds $\frac{r}{a} \geq 0.245$, the adjacent pores intersect with each other and hence these crescents are needed to preserve the periodicity of the unit cell.

Figure 1.2 (bottom) shows the calculated volume fraction of air (and silicon) in the inverse woodpile crystal versus the relative pore radius $\frac{r}{a}$. We employ a volume integration routine of the finite element method [55] for the numerical calculation. To preserve periodicity of the numerically approximated unit cell, we consider the primitive unit cell in (i) for a pore radius between $\frac{r}{a} = 0$ and $\frac{r}{a} = 0.245$ and the modified unit cell in (ii) for a pore radius between $\frac{r}{a} = 0.245$ and $\frac{r}{a} = 0.30$. Our numerical calculation agrees within $\sim 10^{-6}\%$ with the analytical calculation for all pore radii. Therefore, our numerically approximated unit cell, employed for all calculations in this thesis, converges to the analytically designed unit cell. Since an inverse woodpile crystal consists of nearly 80% air by volume fraction at the optimal pore radius $\frac{r}{a} = 0.245$, it is an extremely light-weight candidate for photovoltaic applications, when compared to a bulk silicon of comparable thickness .

A resonant cavity, formed by intentionally embedding a point defect in an infinite 3D photonic band gap crystal, provides an ultimate confinement of light. Since there is no leakage of light in any dimension, the cavity acts as a "3D cage" or a "nanobox" of light [25, 56]. For an array of resonant cavities inside a 3D photonic band gap crystal, light can either remain confined in multiple 3D cages or "hop" from one cavity to another in a radical contrast with the Bloch wave propagation of light [57], as illustrated in the artistic impression in Fig. 1.3 (A). Therefore, an array of cavities inside a 3D photonic band gap crystal, as shown in the real fabricated crystal in Fig. 1.3 (B), is a photonic analogue of the Nobel prize winning "Anderson model" that portrays electronic and spin excitations [58].

1
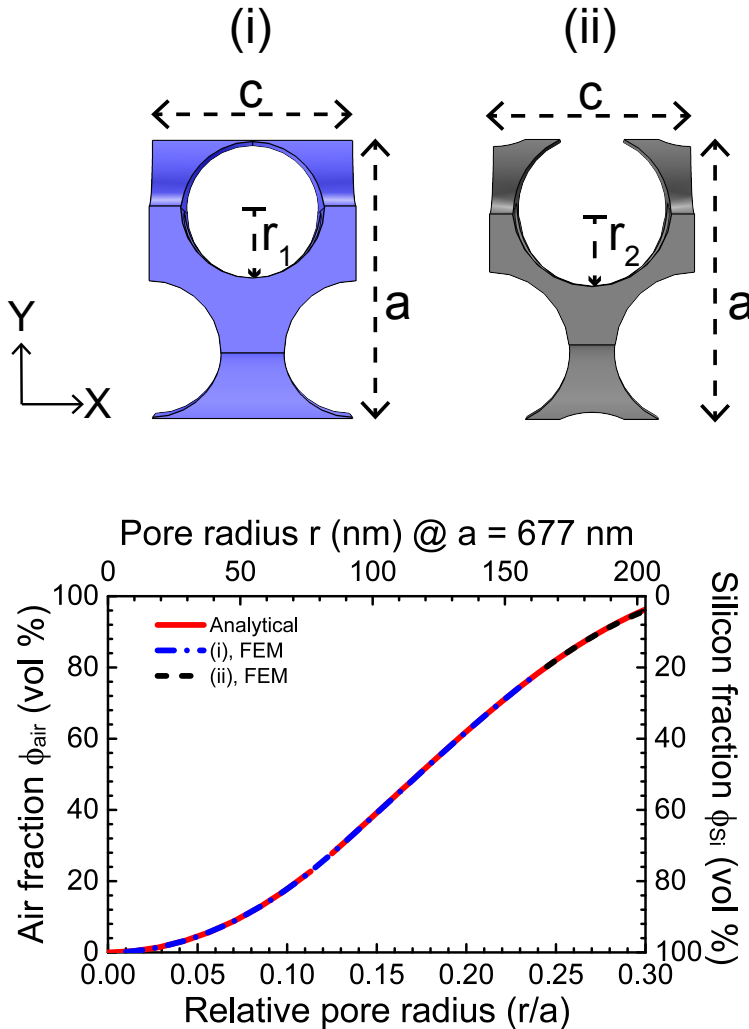
Figure 1.2: Top: (i) The tetragonal primitive unit cell of the cubic inverse woodpile photonic crystal structure along the Z axis with lattice parameters c and a and the pore radius $\frac{r_1}{a} = 0.245$, (ii) unit cell adapted to a large pore radius $\frac{r_2}{a} = 0.275$. The blue and black colors in (i) and (ii), respectively, indicate the high-index backbone of the crystal. The white color represents air. Bottom: Volume fraction of air in the 3D inverse woodpile photonic crystal versus the relative pore radius $\frac{r}{a}$. The blue dashed-dotted curve indicates the numerical result for a pore radius between $\frac{r}{a} = 0$ and $\frac{r}{a} = 0.245$ using the primitive unit cell in (i). The black dashed curve indicates the numerical result for a pore radius between $\frac{r}{a} = 0.245$ and $\frac{r}{a} = 0.30$ using the modified unit cell in (ii). The red solid curve represents unpublished analytical results by Femius Koenderink (2001).
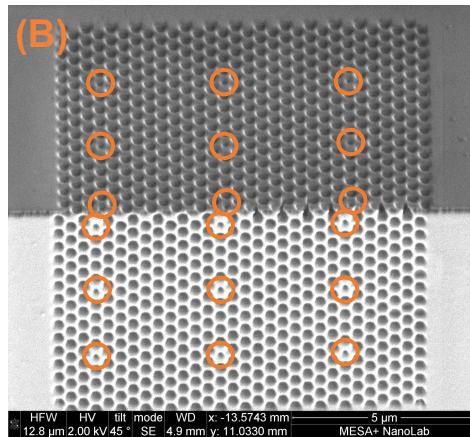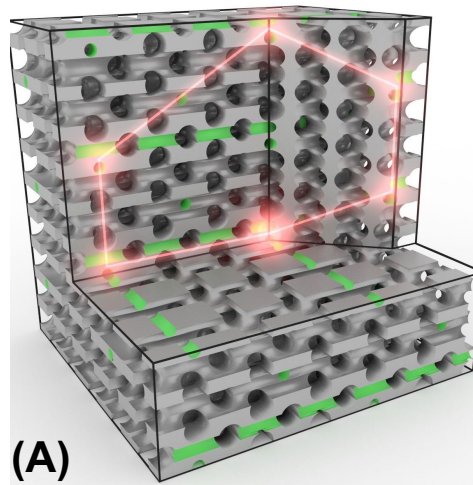
Figure 1.3: (A) Artistic impression of an array of cavities inside a 3D photonic band gap crystal. The point defect acting as a cavity is formed in the proximal region of two orthogonal pores with a radius that is smaller (green) from the ones in the bulk of the crystal. Bright lines represent the exotic hopping transport of light from one cavity to another in a radical contrast with the Bloch wave propagation of light. (B) SEM image of an array of $3 \times 3 \times 3$ cavities in a 3D inverse woodpile photonic crystal fabricated in silicon. Smaller pores, which are marked with orange circles, form cavities inside the structure. The scale bar is shown in the image. SEM image courtesy of Cock Harteveld.

1.4 Numerical simulations for disrupted symmetries: a bridge between theory and experiments

The ubiquitous laws of nature are expressed in terms of equations that cannot be solved analytically for nanophotonic systems [59]. Therefore, one has to postulate a theory that provides a description of these systems using approximations like infinite extension and perfect symmetry. As the French scientist Blaise Pascal said: *Symmetry is what we see at a glance.*

In order to validate these approximate theories, we compare them directly with experiments on real systems. However, real systems have disrupted symmetries [60]. For 3D periodic photonic nanostructures, we distinguish two kinds of symmetry-disruption: (i) unintentional symmetry-disruption, *e.g.*, finite size, material absorption, tapered pores, monoclinic deformation, and surface roughness, and (ii) intentional symmetry-disruption, *e.g.*, a point defect acting as a resonant cavity, and a photonic crystal waveguide. Therefore, theory for infinite perfect crystals can not predict the complete outcome of experiments on real systems. Up to date, theories for finite crystals are limited and address only few properties, *e.g.*, densities of states [61, 62]. Here, numerical simulations act as an optimal experiment designed to test the predictions of theories and improve its approximations. Hence, a simulation can show that a particular theoretical model captures the essential physics that is needed to reproduce a given phenomenon in an experiment [26]. Thus, numerical simulations act as a bridge between theory and experiments. Significantly, exact results from a known analytical model are an essential tool to test whether a particular numerical simulation works correctly: if simulation results disagree with an exact theoretical result, then the simulation is imprecise [59].

Experimental research in the field of nanophotonics is rapidly accelerating due to improvements in sophisticated fabrication methods and novel characterization tools. However, these experiments are very challenging, costly, and endure physical limitations. Hence, numerical simulations play a pivotal role to support experiments [26, 59]. Numerical simulations are frequently used to predict the material properties under certain optimal conditions that are difficult to achieve in controlled experiments (*e.g.*, very high temperatures or pressures). Moreover, numerical simulations act as a purely exploratory tool by predicting *apriori* the properties of materials even before physically fabricating them [63]. Therefore, numerical simulations support the planning of a research project by finding appropriate systems and geometries and thereafter performing proofs of concepts without being constrained by physical limitations [26]. After fabrication of these systems, numerical simulations are employed to ascertain the quality of fabrication and to optimize the system parameters for the performance enhancement. Since a simulation can perform independent investigation of various physical effects and assess quantities inaccessible in experiments, it simplifies the interpretation of the underlying physics. This acts as a feedback for future designs of the systems.

In order to maintain the numerical-simulation bridge between theory and experiments, numerical scientists should follow the simulation etiquette: by em-

ploying well defined reduced units and providing a convenient conversion to the experimentally employed units [63]. It is important to note that the numerical solution itself offers no more understanding of the system rather than some numbers. Therefore, it is essential to understand the underlying physics behind the numerical findings and then relate with experiments.

1.5 Overview of this thesis

This thesis describes three ways in which the symmetry of a 3D photonic band gap crystal is disrupted. We investigate the unintentionally disrupted symmetry due to (i) finite size and (ii) material absorption as well as the intentionally disrupted symmetry due to (iii) a point defect acting as a resonant cavity. Each symmetry-disruption forms the basis of an extensive study to understand the physics of light propagation in certain nanophotonic media and hence investigate its significance in reality. We validate our numerical models with respect to analytical models and interpret our numerical findings using fundamental theories of physics. We present all our results in well defined reduced units as well as their corresponding experimentally employed units. Finally, we describe the mathematics of a cutting-edge computational tool to accurately model the light propagation at nanoscale for complex photonic systems. This thesis has the following arrangement:

In Chapter 2, we study numerically the reflectivity of 3D photonic band gap crystals with finite support. We assess previously invoked experimental limitations to the reflectivity, such as crystal thickness, angle of incidence, and Bragg attenuation length. We observe that the stop band hardly changes with incident angle, which supports the experimental notion that strong reflectivity peaks measured with a large numerical aperture gives a faithful signature of the 3D band gap. We observe an intriguing hybridization of the Fabry-Pérot resonances and the Brewster angle in our calculations, which seems a characteristic property of 3D photonic band gap crystals. From the intense reflectivity peaks, we infer that the maximum reflectivity observed in the experiments is not limited by the finite size of the crystal. Consequently, the comparison between angle-independent numerical calculations and experimental results provides an improved interpretation of reflectivity as a signature of a complete 3D photonic band gap.

In Chapter 3, we study a 3D photonic band gap crystal with finite support as a back reflector to a thin silicon film in the visible regime. To make our calculations relevant to experiments, we consider a dispersive (wavelength-dependent) complex refractive index obtained from experiments. We compare the photonic crystal back reflector to a perfect metallic back reflector and assess the absorption enhancement without the additional length of a back reflector. Our numerical study reports a nearly 2.6 times enhanced frequency-, angle-, polarization-averaged absorption between $\lambda = 680$ nm and $\lambda = 890$ nm compared to a thin silicon film only. Aiming beyond just reporting a giant enhancement, we identify the responsible physical mechanisms apart from a standard back reflector to understand the underlying physics.

1

In Chapter 4, we study the reflectivity and absorption of a 3D photonic band gap crystal with finite support and with an intentional point defect. We identify five cavity resonance troughs in reflectivity for a finite crystal and their field patterns. We confirm the localization of these cavity resonances in real space by verifying their angle-dependency. We find a large electric-field energy enhancement due to these resonances. We study resonances existing below the 3D band gap of a perfect crystal and investigate the effect of the resonant cavity on the linear regime of the band structure. Our results indicate that 3D photonic band gap crystals with resonant cavities are interesting candidates for the absorbing medium of a solar cell in order to enhance the photovoltaic efficiency. Therefore, our analysis provides a numerical signature of cavity resonances appearing due to the locally disrupted lattice symmetry in a 3D inverse woodpile photonic crystal and signifies their potential application in photovoltaics.

In Chapter 5, we investigate and implement a novel numerical method to provide an accurate model of light propagation in the nanophotonic media. Starting with the macroscopic Maxwell equations, we provide an extensive description of the discontinuous Galerkin finite element method (DGFEM) solver for the time-harmonic Maxwell equations. We highlight the significance of explicitly incorporating the divergence constraint ($\nabla \cdot E = 0$) that is often neglected. Consequently, we present the k shifted eigenvalue problem formulation with an explicitly enforced divergence condition for periodic dielectric materials, which is well equipped for efficient photonic band structure calculations.

Finally, we summarize the results of this thesis in Chapter 6 and present an outlook for further studies.

Bibliography

[1] "International year of light and light-based technologies 2015," available on *http://www.light2015.org/Home/WhyLightMatters/What-is-Photonics.html.* 11

[2] Euclid, *"Optica,"* (the English translation is available as: H. E.Burton, "The Optics of Euclid"), J. Opt. Soc. Am. **25**, 5 (1945). 11

[3] C. Hyugens (translated by S.P. Thompson, 1912), *"Treatise on Light,"* Project Gutenberg (2005). 11

[4] I. Newton, *"Opticks: or, a treatise of the reflexions, refractions, inflexions and colours of light,"* 4th edition, (Dover Publications, New York, 1952) (Opticks was originally published in 1704). 11

[5] M. Planck, *"Eight Lectures on Theoretical Physics,"* translated by A. P. Wills, (Dover Publications, New York, 1915). 11

[6] A. Einstein, "Über einen die Erzeugung und Verwandlung des Lichtes betreffenden heuristischen Gesichtspunkt," ("On a heuristic point of view concerning the production and transformation of light,") Annalen der Physik **17**, 132 (1905). 11

[7] S.H. Yun and S.J.J. Kwok "Light in diagnosis, therapy and surgery," Nat. Biomed. Eng. **1**, 0008 (2017). 11

[8] E. Hecht, *"Optics,"* (Addison-Wesley, 2002). 11

[9] L. Novotny and B. Hecht, *"Principles of nano-optics,"* (Cambridge University Press, Cambridge, 2006). 11

[10] A. F. Koenderink, *"Emission and transport of light in photonic crystals,"* PhD thesis (2003). 12

[11] S. R. Huisman, *"Light control with ordered and disordered nanophotonic media,"* PhD thesis (2013). 12

[12] O. S. Ojambati, *"Stirring the propagation and the absorption of light in complex nanophotonic systems,"* PhD thesis (2016). 12

[13] V. P. Bykov, "Spontaneous emission in a periodic structure," Soviet Phys. JETP **35**, 269 (1972). 12

[14] M. P. van Albada and A. Lagendijk, "Observation of weak localization of light in a random medium," Phys. Rev. Lett. **55**, 2692 (1985). 12

[15] P. -E. Wolf and G. Maret, "Weak localization and coherent backscattering of photons in disordered media," Phys. Rev. Lett. **55**, 2696 (1985). 12

[16] E. Yablonovitch, "Inhibited spontaneous emission in solid-state physics and electronics," Phys. Rev. Lett. **58**, 2059 (1987). 12

[17] S. John, "Strong localization of photons in certain disordered dielectric superlattices," Phys. Rev. Lett. **58**, 2486 (1987). 12

[18] J. D. Joannopoulos, P. R. Villeneuve, and S. Fan, "Photonic crystals: putting a new twist on light," Nature (London) **386**, 143 (1997). 12

[19] A. Lagendijk, B. van Tiggelen, and D. S. Wiersma, "Fifty years of Anderson localization," Physics Today **62**, 24 (2009). 12

[20] D. S. Wiersma, "Disordered photonics," Nat. Photon. **7**, 188 (2013). 12

[21] E. Yablonovitch and G. Cody, "Intensity enhancement in textured optical sheets for solar cells," IEEE Trans. Electron Devices **29**, 300 (1982). 12

[22] E. F. Schubert, *"Light-emitting diodes,"* (Cambridge University Press, 2003). 12

[23] F. Bloch, "Über die Quantenmechanik der Elektronen in Kristallgittern", Z. f. Physik **52**, 555 (1928). 12

[24] N. W. Ashcroft and N. D. Mermin, *"Solid state physics,"* (Holt, Rinehart and Winston, New York NY, 1976). 12, 14

[25] J. D. Joannopoulos, S. G. Johnson, J. N. Winn, and R. D. Meade, *"Photonic crystals: Molding the flow of light,"* (Princeton University Press, Princeton NJ, 2008). 12, 14

[26] K. Busch, M. König, and J. Niegemann, "Discontinuous Galerkin methods in nanophotonics," Laser Photon. Rev. **5**, 773 (2011). 17

[27] C. Lopez, "Materials aspect of photonic crystals", Adv. Mater. **15**, 1679 (2003). 12

[28] J. M. Lourtioz, H. Benisty, V. Berger, J. -M. Gérard, D. Maystre, and A. Tchelnokov, *"Photonic crystals: towards nanoscale photonic devices,"* (Springer, Heidelberg, 2005). 12

[29] Edited by M. Ghulinyan and L. Pavesi, *"Light Localisation and Lasing: Random and Pseudorandom Photonic Structures,"* (Cambridge Univ. Press, Cambridge, 2015). 12, 22

[30] A. F. Koenderink, L. Bechger, H. P. Schriemer, A. Lagendijk, and W. L. Vos, "Broadband fivefold reduction of vacuum fluctuations probed by dyes in photonic crystals," Phys. Rev. Lett. **88**, 143903 (2002). 12

[31] S. Ogawa, M. Imada, S. Yoshimoto, M. Okano, and S. Noda, "Control of Light Emission by 3D Photonic Crystals," Science **305**, 227 (2004). 12

[32] P. Lodahl, A. F. van Driel, I. S. Nikolaev, A. Irman, K. Overgaag, D. Vanmaekelbergh, and W. L. Vos, "Controlling the dynamics of spontaneous emission from quantum dots by photonic crystals," Nature (London) **430**, 654 (2004). 12

[33] M. D. Leistikow, A. P. Mosk, E. Yeganegi, S. R. Huisman, A. Lagendijk, and W. L. Vos, "Inhibited spontaneous emission of quantum dots observed in a 3D photonic band gap," Phys. Rev. Lett. **107**, 193903 (2011). 12

[34] N. Vats, S. John, and K. Busch, "Theory of fluorescence in photonic crystals," Phys. Rev. A **65**, 043808 (2002). 12

[35] W. L. Vos and L. A. Woldering, in Ref. 29 Chapter 8, pp. 180-214, also available from: http://arxiv.org/abs/1504.06803. 12

[36] J. G. Fleming, S. -Y. Lin, I. El-Kady, R. Biswas, and K. M. Ho, "All-metallic three-dimensional photonic crystals with a large infrared bandgap," Nature (London) **417**, 52 (2002). 12

[37] S. E. Han, A. Stein, and D. J. Norris, "Tailoring self-assembled metallic

photonic crystals for modified thermal emission," Phys. Rev. Lett. **99**, 053906 (2007). 12

[38] A. Tandaechanurat, S. Ishida, D. Guimard, M. Nomura, S. Iwamoto, and Y. Arakawa, "Lasing oscillation in a three-dimensional photonic crystal nanocavity with a complete bandgap," Nat. Photon. **5**, 91 (2011). 12

[39] P. Bermel, C. Luo, L. Zeng, L. C. Kimerling, and J. D. Joannopoulos, "Improving thin-film crystalline silicon solar cell efficiencies with photonic crystals," Opt. Express **15**, 25 (2007). 12

[40] D. Zhou and R. Biswas, "Photonic crystal enhanced light-trapping in thin film solar cells," J. Appl. Phys. **103**, 093102 (2008). 12

[41] T. Ergin, N. Stenger, P. Brenner, J. B. Pendry, and M. Wegener, "Three-dimensional invisibility cloak at optical wavelengths," Science **328**, 337 (2010). 12

[42] K. M. Ho, C. T. Chan, C. M. Soukoulis, R. Biswas, and M. Sigalas, "Photonic band gaps in three dimensions: new layer-by-layer periodic structures," Solid State Commun. **89**, 413 (1994). 12, 14

[43] R. Hillebrand, S. Senz, W. Hergert, and U. Gösele, "Macroporous-silicon-based three-dimensional photonic crystal with a large complete band gap," J. Appl. Phys. **94**, 2758 (2003). 12, 14

[44] L. A. Woldering, A. P. Mosk, R. W. Tjerkstra, and W. L. Vos, "The influence of fabrication deviations on the photonic band gap of three-dimensional inverse woodpile nanostructures," J. Appl. Phys. **105**, 093108 (2009). 12, 14

[45] J. Schilling, J. White, A. Scherer, G. Stupian, R. Hillebrand, and U. Gösele, "Three-dimensional macroporous silicon photonic crystal with large photonic band gap," Appl. Phys. Lett. **86**, 011101 (2005). 12

[46] F. García-Santamaría, M. Xu, V. Lousse, S. Fan, P. V. Braun, and J. A. Lewis, "A germanium inverse woodpile structure with a large photonic band gap," Adv. Mater. **19**, 1567 (2007). 12

[47] A. Hermatschweiler, A. Ledermann, G. A. Ozin, M. Wegener, and G. von Freymann, "Fabrication of silicon inverse woodpile photonic crystals," Adv. Funct. Mater. **17**, 2273 (2007). 12

[48] B. Jia, S. Wu, J. Li, and M. Gu, "Near-infrared high refractive-index three-dimensional inverse woodpile photonic crystals generated by a sol-gel process," J. Appl. Phys. **102**, 096102 (2007). 12

[49] L. A. Woldering, R. W. Tjerkstra, H. V. Jansen, I. D. Setija, and W. L. Vos, "Periodic arrays of deep nanopores made in silicon with reactive ion etching and deep UV lithography," Nanotechnology **19**, 145304 (2008). 12, 14

[50] J. M. van den Broek, L. A. Woldering, R. W. Tjerkstra, F. B. Segerink, I. D. Setija, and W. L. Vos, "Inverse-woodpile photonic band gap crystals with a cubic diamond-like structure made from single-crystalline silicon," Adv. Func. Mat. **22**, 25 (2012). 12

[51] T. Tajiri, S. Takahashi, Y. Ota, J. Tatebayashi, S. Iwamoto, and Y. Arakawa, "Demonstration of a three-dimensional photonic crystal nanocavity in a < 110 >-layered diamond structure," Appl. Phys. Lett. **107**, 071102 (2015). 12

[52] D. A. Grishina, C. A. M. Harteveld, L. A. Woldering, and W. L. Vos, "Method to make a single-step etch mask for 3D monolithic nanostructure,"

Nanotechnology **26**, 505302 (2015). 12

[53] S. R. Huisman, R. V. Nair, L. A. Woldering, M. D. Leistikow, A. P. Mosk, and W. L. Vos, "Signature of a three-dimensional photonic band gap observed with silicon inverse woodpile photonic crystals," Phys. Rev. B **83**, 205313 (2011). 14

[54] D. Devashish, S. B. Hasan, J. J. W. van der Vegt, and W. L. Vos, "Reflectivity calculated for a three-dimensional silicon photonic band gap crystal with finite support," Phys. Rev. B **95**, 155141 (2017). 14

[55] "COMSOL Multiphysics® v. 5.2. www.comsol.com, COMSOL AB, Stockholm, Sweden". 14

[56] L. A. Woldering, A. P. Mosk, and W. L. Vos, "Design of a three-dimensional photonic band gap cavity in a diamondlike inverse woodpile photonic crystal," Phys. Rev. B. **90**, 115140 (2014). 14

[57] S. A. Hack, J. J. W. van der Vegt, and W. L. Vos, "Cartesian light: unconventional propagation of light in a 3D crystal of photonic-band-gap cavities," Unpublished (2017). 14

[58] P. W. Anderson, "Absence of diffusion in certain random lattices," Phys. Rev. **109**, 1492 (1958). 14

[59] D. Frenkel and B. Smit, *"Understanding molecular simulation from algorithms to applications,"* (Academic Press, San Diego CA, 2002). 17

[60] P. W. Anderson, "More is different," Science **177**, 393 (1972). 17

[61] F. Yndurain, J. D. Joannopoulos, M. L. Cohen, and L. M. Falicov, "New theoretical method to study densities of states of tetrahedrally coordinated solids," Solid State Commun. 15, 617 (1974). 17

[62] S. B. Hasan, E. Yeganegi, A. P. Mosk, A. Lagendijk, and W. L. Vos, "Finite size scaling of density of states in photonic band gap crystals," arXiv:1701.01743 (2017). 17

[63] D. Frenkel, "Simulations: The dark side," Eur. Phys. J. Plus **128**, 1 (2013). 17, 18

CHAPTER 2

Reflectivity calculated for a 3D silicon photonic band gap crystal with finite support

2.1 Introduction

The experimental demonstration of a 3D photonic band gap remains a major challenge. By definition, a 3D band gap corresponds to a frequency range where the density of optical states (DOS) vanishes. To probe the DOS, spectra or dynamics are studied of emitters positioned inside the crystal [1–4]. Such experiments are difficult and require sources as well as detection methods. On the other hand, a band gap is indicated by the overlap of stop bands for all directions of incidence, as shown by a peak in reflectivity or a trough in transmission [5–11] for ideally all directions. A peak in reflectivity or a trough in transmission may also occur, however, when incident waves do not couple to a field mode inside the crystal [12–14]. Thus, experimentally observed stop bands are typically interpreted by comparing to stop gaps calculated from band structures. As band structures pertain only to infinite and perfect crystals, features related to finite-size or to unavoidable deviations from perfect periodicity are not considered.

Recently, several experimental studies of powerful silicon woodpile and silicon inverse woodpile photonic crystals were reported [10, 11, 15]. In these three studies, a maximum reflectivity was found in the range from 40% to 60%, and the deviations from ideal 100% were attributed to various reasons, mostly experimental ones. It was asserted that intense reflection peaks measured with a large numerical aperture provide a faithful signature of the 3D photonic band gap. The limited reflectivity was attributed to the limited crystal thickness in comparison to the Bragg attenuation length and to surface roughness, although no theoretical or numerical support was offered for these notions.

Therefore, in the present article we study numerically the reflectivity of 3D photonic band gap crystals with disrupted symmetries due front and back interfaces. We apply the finite element method to calculate reflectivity of crystals with the cubic diamond-like inverse woodpile structure that have a broad 3D photonic band gap [16–18]. Inverse woodpile photonic crystals have been realized in several different backbone materials using various techniques [19–22]. Our research group has fabricated 3D inverse woodpile photonic crystals from
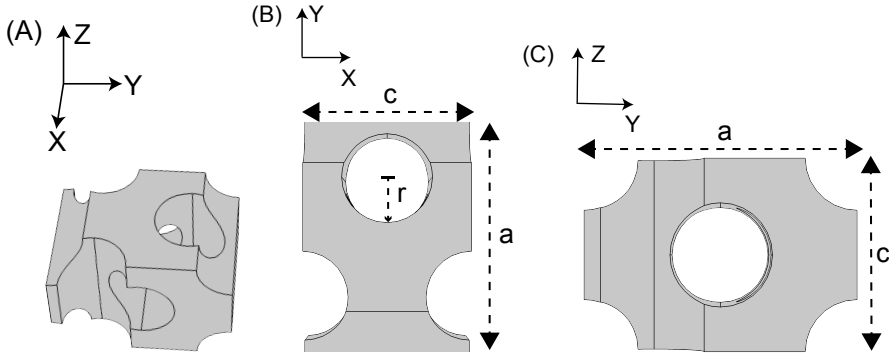
Figure 2.1: The tetragonal primitive unit cell of the cubic inverse woodpile photonic crystal structure. (A) Perspective view of the unit cell with the XYZ coordinate system. The two sets of pores are parallel to the X and the Z-axes. (B) View of the unit cell along the Z-axis with the lattice parameters a and c, and the pore radius $\frac{r}{a} = 0.19$. (C) View of the unit cell along the X-axis.

silicon using several CMOS-compatible methods [23–25]. The high-index backbone of the crystals has a dielectric function similar to silicon. We investigate crystals with thicknesses up to ten unit cells. Since the crystals are surrounded by vacuum, they have a finite support as in the experiments. We assess previously invoked limitations to the reflectivity, such as crystal thickness, angle of incidence, and Bragg attenuation length. Consequently, our numerical study provides an improved interpretation of reflectivity as a signature of a complete 3D photonic band gap.

2.2 Methods

The primitive unit cell of the cubic inverse woodpile photonic structure is illustrated in Fig. 2.1. The crystal structure consists of two 2D arrays of identical pores with radius r running in two orthogonal directions X and Z [16]. Each 2D array has a centered-rectangular lattice with lattice parameters c and a. When the lattice parameters have a ratio $\frac{a}{c} = \sqrt{2}$, the diamond-like structure is cubic. In terms of the conventional non-primitive cubic unit cell of the diamond structure, the (X, Y, Z) coordinate system shown in Fig. 2.1(A) has the X-axis unit vector $a_1 = \frac{1}{\sqrt{2}}[1\ 0\ 1]$, the Y-axis $a_2 = [0\ 1\ 0]$, and the Z-axis $a_3 = \frac{1}{\sqrt{2}}[\bar{1}\ 0\ 1]$ in the coordinate frame of the conventional cubic unit cell [26]. Cubic inverse woodpile photonic crystals with $\epsilon = 11.68$ [27]- typical of silicon - have a broad maximum band gap width $\Delta\omega/\omega_c = 23.7$ % relative to the central band gap frequency ω_c for pores with a relative radius $\frac{r}{a} = 0.245$ [17, 18]. To compare our calculations with experimental results [24], we choose the pore radius to be $\frac{r}{a} = 0.19$ and the lattice parameter to be $a = 677$ nm [28]. To compute the dispersion relations for infinitely extended crystals, we employed the MPB plane-wave expansion method [29]. Figure 2.2 (A, B) shows the band structure and the first

Brillouin zone for an inverse-woodpile crystal with optimal pore size $\frac{r}{a} = 0.245$. A broad photonic band gap with a 23.7 % relative width appears between reduced frequency $\tilde{\omega}_1 = 0.52$ (bounded by the 3rd and 4th bands) and $\tilde{\omega}_2 = 0.66$ (5th band) [30]. The band structure shows two stop gaps in the ΓZ direction. Since the ΓX stop gap is symmetry-related to the ΓZ stop gap, we effectively consider both stop gaps in the present study. The lowest-frequency narrow stop gap appears between $\tilde{\omega} = 0.421$ and $\tilde{\omega} = 0.433$ and closes when moving in the ZU direction. The second stop gap between $\tilde{\omega} = 0.52$ and $\tilde{\omega} = 0.70$ is part of the complete 3D photonic band gap and has a broad 29.5 % relative bandwidth. In the low-frequency limit $\omega \to 0$, we derive from the slope of the bands the effective refractive index of the crystal to be $n_e = 1.68$.

To accurately model the reflectivity and transmission spectra of photonic band gap crystals with finite support, we employ the commercial COMSOL finite-element (FEM) solver to solve for the time-harmonic Maxwell equations [31]. Figure 3.2(A) illustrates the computational cell along the X direction. The incident fields emanate from a plane at the left that is separated from the crystal by an air layer. The plane rather represents a boundary condition than a true current source since it also absorbs the reflected waves [32]. The incident plane waves have either s polarization (electric field normal to the plane of incidence) or p polarization (magnetic field normal to the plane of incidence), and have an angle of incidence between 0° and 80°. To mimic infinite space by minimizing the back reflections, absorbing boundaries are employed in the $-Z$ and $+Z$ directions, where the crystal is finite in size. We employ Bloch-Floquet periodic boundaries in the $\pm X$ and the $\pm Y$ directions to describe a crystal slab [12]. Figure 3.2(B) illustrates the finite element mesh used to subdivide the 3D computational cell. We used tetrahedra as basic elements in our finite element mesh. An upper limit of $\Delta l \leq \frac{\lambda_0}{8\sqrt{\epsilon}}$ is imposed to the edge length Δl on any tetrahedron, with λ_0 the shortest wavelength of the incident plane waves in vacuum, leading to a finite element mesh of 27852 tetrahedra per unit cell. A refined mesh is used at the interface between the high-index material and the low-index material to reduce dispersion errors. For computational efficiency, we apply the MUMPS direct solver that is fast, multi-core capable, and cluster capable. For a single frequency and a single angle of incidence, the computational time is 35 s on a Intel Core i7 machine with a single processor of 4 cores. We found that the computational time increases sub-linearly with respect to the number of frequency steps and the number of angle of incidence steps.

2.3 Results

2.3.1 Angle- and frequency-resolved reflectivity

Figure 2.4 shows the angle-resolved and frequency-resolved reflectivity spectra for an inverse-woodpile crystal with a thickness $L = 4c$ for angles of incidence up to 80° off normal and for optimal pore radius $\frac{r}{a} = 0.245$. Near $\tilde{\omega} = 0.6$ we observe broad stop bands with nearly 100% reflectivity for both polarizations. The stop bands agree very well with the stop gaps for the infinite crystal (see Fig. 2.2(A)).
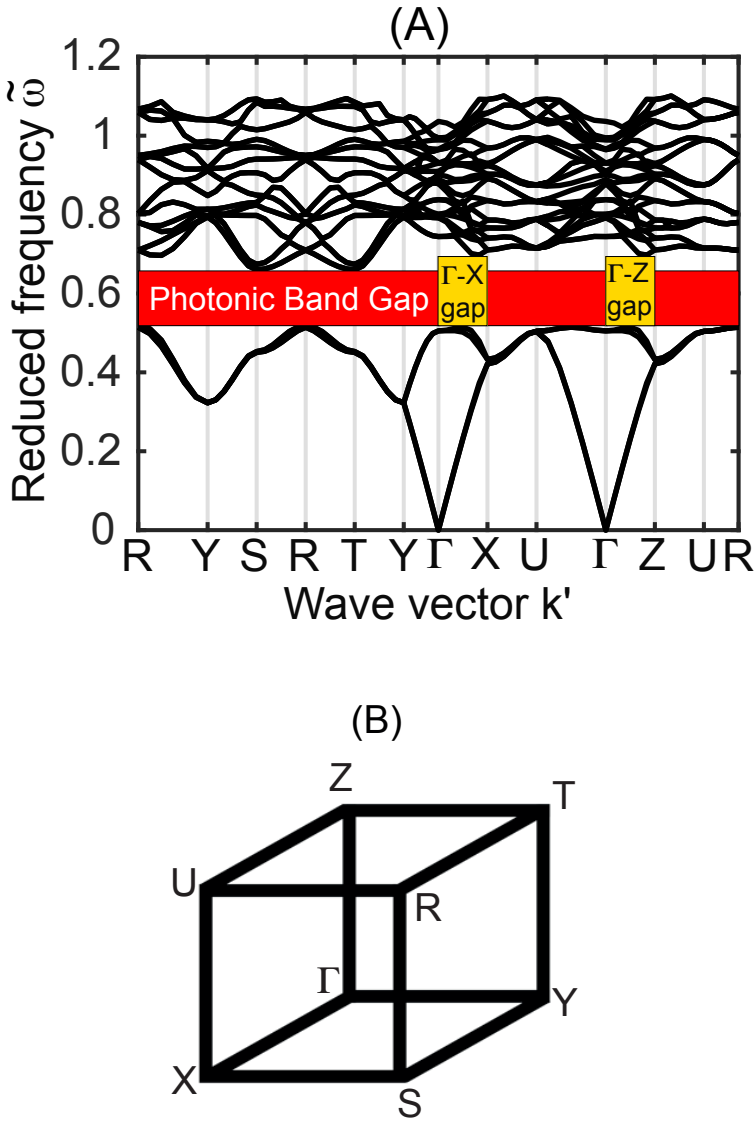
Figure 2.2: (A) Photonic band structure for the 3D inverse woodpile photonic crystal with $\frac{r}{a} = 0.245$ and $\epsilon_{Si} = 11.68$. The reduced frequency [30] $\tilde{\omega}$ is expressed in units of (a/λ), with a the lattice parameter. The wave vector is expressed as $k' = (ka/2\pi)$. The red bar marks the 3D photonic band gap, and the yellow bars mark stop gaps in the ΓX and ΓZ directions. (B) First Brillouin zone showing the high symmetry points and the origin at Γ.

We observe that the frequency range of the stop bands hardly changes with angle of incidence, which is plausible since the stop bands are part of the 3D band gap. This result supports the experimental notion that intense reflectivity
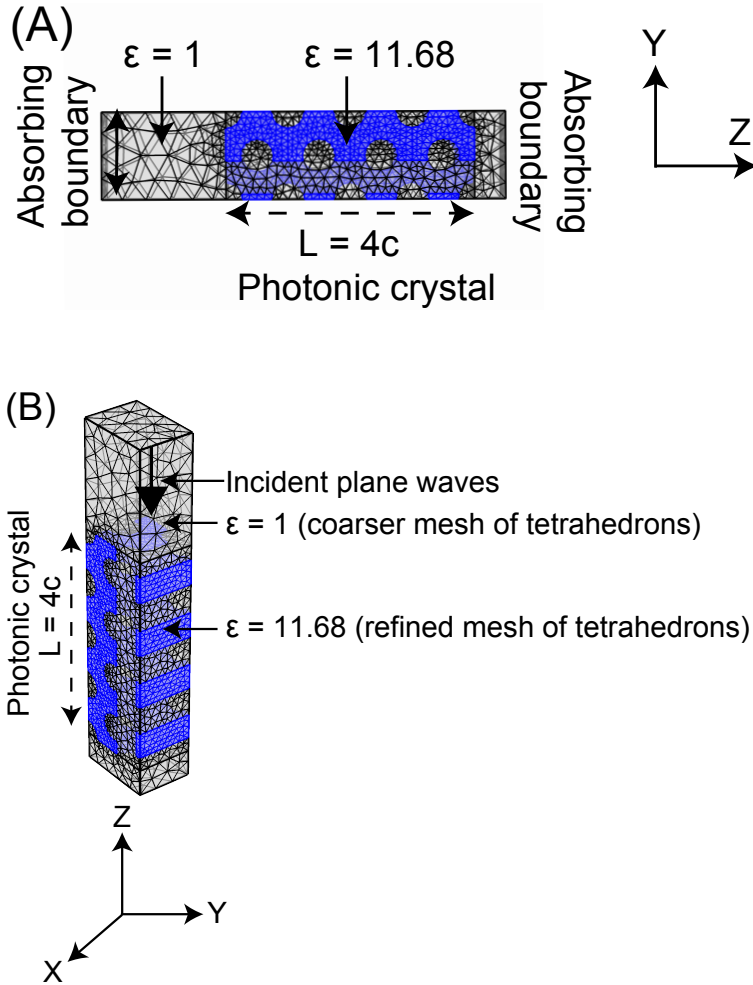
Figure 2.3: Illustration of the computational cell for a photonic crystal with thickness $L = 4c$. (A) View along the X direction [101]. The source of plane waves is at the left, and is separated by an air layer from the crystal. The computational cell is bounded by absorbing boundaries at $-Z$ and $+Z$, and by periodic boundary conditions on $\pm X$ and $\pm Y$. The blue color represents the high-index backbone of the crystal having dielectric function similar to silicon. (B) Perspective view of the computational cell.
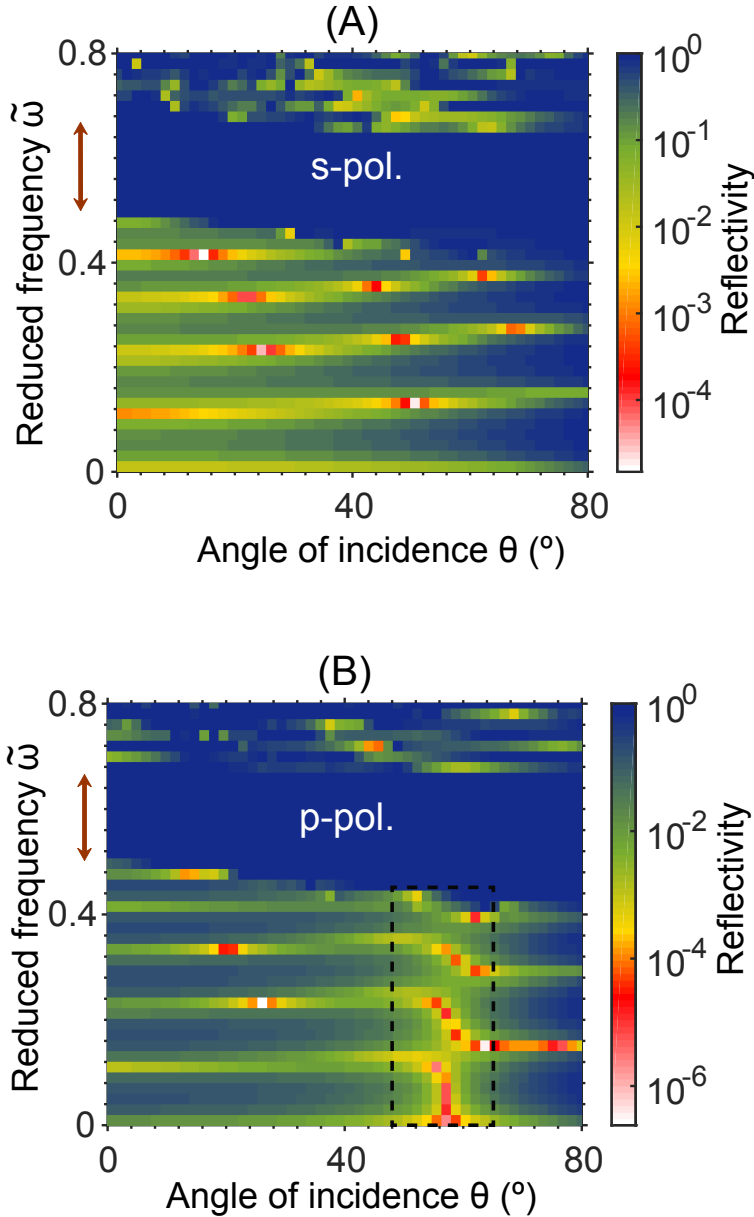
Figure 2.4: Calculated angle- and frequency- resolved reflectivity spectra in the ΓZ direction for a crystal with thickness $L = 4c$ for (A) s polarization and (B) p polarization. The dark blue color represents high reflectivity that occurs in the stop band at all angles. The white color represents near 0% reflectivity that occurs in the Fabry-Pérot fringes, at the Brewster angle, and in their hybridization in the range $54° \leq \theta \leq 61°$. The brown double arrow represents the stop gap in the ΓZ direction (from Fig. 2.2). The black box indicates the region of high-resolution results shown in Fig. 2.5.
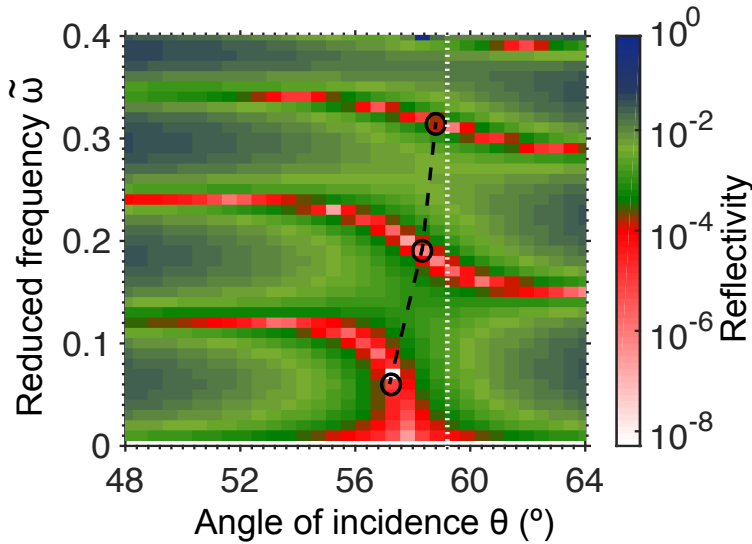
Figure 2.5: Hybridization of the Fabry-Pérot resonances and the Brewster angle, shown by angle- and frequency- resolved calculated reflectivity spectra in ΓZ direction for p polarization. The black dashed line is a guide to the eye that connects the mid-points (circles) of the bends in the fringes. The white dotted line indicates the Brewster angle θ_B.

peaks collected with an objective with a large numerical aperture give a *bona fide* signature of the 3D band gap [15].

The spectra in Fig. 2.4 ((A), (B)) reveal Fabry-Pérot fringes at frequencies below the band gap that correspond to standing waves in the finite crystal slab. For p polarization, Fig. 2.4 reveals an intriguing hybridization of the resonance condition ($R = 0$) of the Fabry-Pérot fringes and of the Brewster angle, which has not yet been observed in experiments. Moreover, reflectivity inside the p-stop band is not affected by the Brewster angle, unlike a 1D Bragg stack as shown in Ref. 33. In order to characterize this feature, we calculated reflectivity spectra using a higher resolution in frequency and angle of incidence, shown in Fig. 2.5. We note that the Fabry-Pérot fringes have a constant frequency for angles of incidence up to $\theta = 54°$ before bending. Beyond $\theta = 61°$, the fringes have shifted down in frequency to nearly the frequency of the lower order one at $\theta \leq 54°$, *e.g.*, the $n = 2$ fringe at $\tilde{\omega} = 0.24$ ($\theta \leq 54°$) shifts to $\tilde{\omega} = 0.15$ ($\theta > 61°$), which is close to the frequency of the $n = 1$ fringe at $\theta \leq 54°$. From the effective refractive index ($n_e = 1.68$), we derive the Brewster angle $\theta_B = 59.2°$, which matches the range ($54° \leq \theta \leq 61°$) of the hybridization. Therefore, we conclude that the hybridization occurs between the Fabry-Pérot resonances and the Brewster angle.

Figure 2.5 shows that the midpoint of each bend in a fringe increases with increasing frequency and fringe order. We surmise that this shift is the result of an increasing effective index with frequency as a result of increasing band
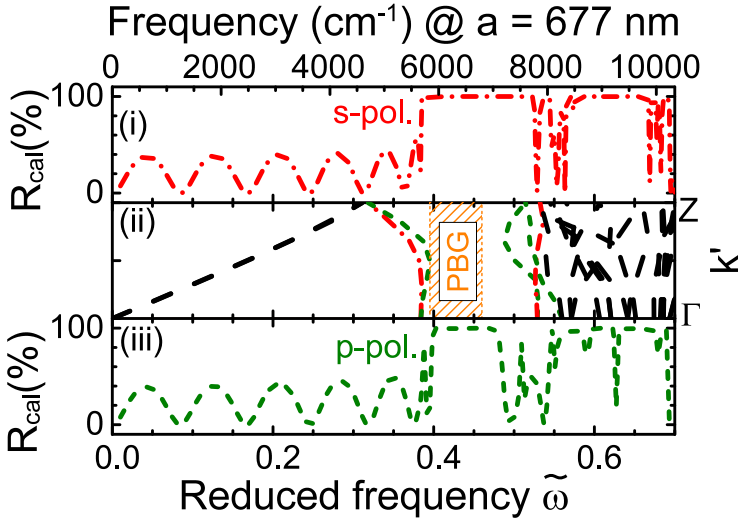
Figure 2.6: Calculated reflectivity spectra for a Si inverse woodpile photonic band gap crystal along the ΓZ high symmetry direction in wave vector space. The red curve in panel (i) and the green curve in panel (iii) are reflectivity spectra calculated for s and p polarization, respectively. The corresponding band structure for the ΓZ direction is shown in panel (ii), where the 3D band gap is shown in orange. The wave vector is expressed as $k' = (ka/2\pi)$. The polarization character of bands near the gap is assigned in Fig. 2.7. The frequency ranges of the s- and p-stop bands agree excellently with corresponding stop gaps in the photonic band structure.

flattening in the approach of a stop gap or band gap, see Fig. 2.2. We note that at the lowest frequency the midpoint occurs at a smaller angle than θ_B obtained from n_e in the limit $\omega \to 0$. This difference is currently puzzling, since both angles are expected at the same angle at low frequency where no band bending occurs. We speculate that the hybridization probes another effective index than the one derived from the bands at $\omega \to 0$. The radius of curvature of a bend increases while approaching the stop band. A possible cause may be the approach of the 3D photonic band gap that prevents light from entering at a Brewster angle.

For comparison, we have analytically computed the angle- and frequency-resolved reflectivity spectra of a thin film for p polarization (see Appendix 2.B). We find that the Brewster angle is constant with frequency. We also observe that the Fabry-Pérot fringes have a constant frequency at all angles and do not bend near the Brewster angle. These observations on a thin film also pertain to a 1D Bragg stack as shown in Ref. 34. Therefore, the hybridization between the Fabry-Pérot resonances and the Brewster angle appears to be a characteristic property of the 3D photonic crystal that remains to be observed experimentally.

(A) Frequency (cm⁻¹) @ a = 677 nm

(B) Frequency (cm⁻¹) @ a = 677 nm
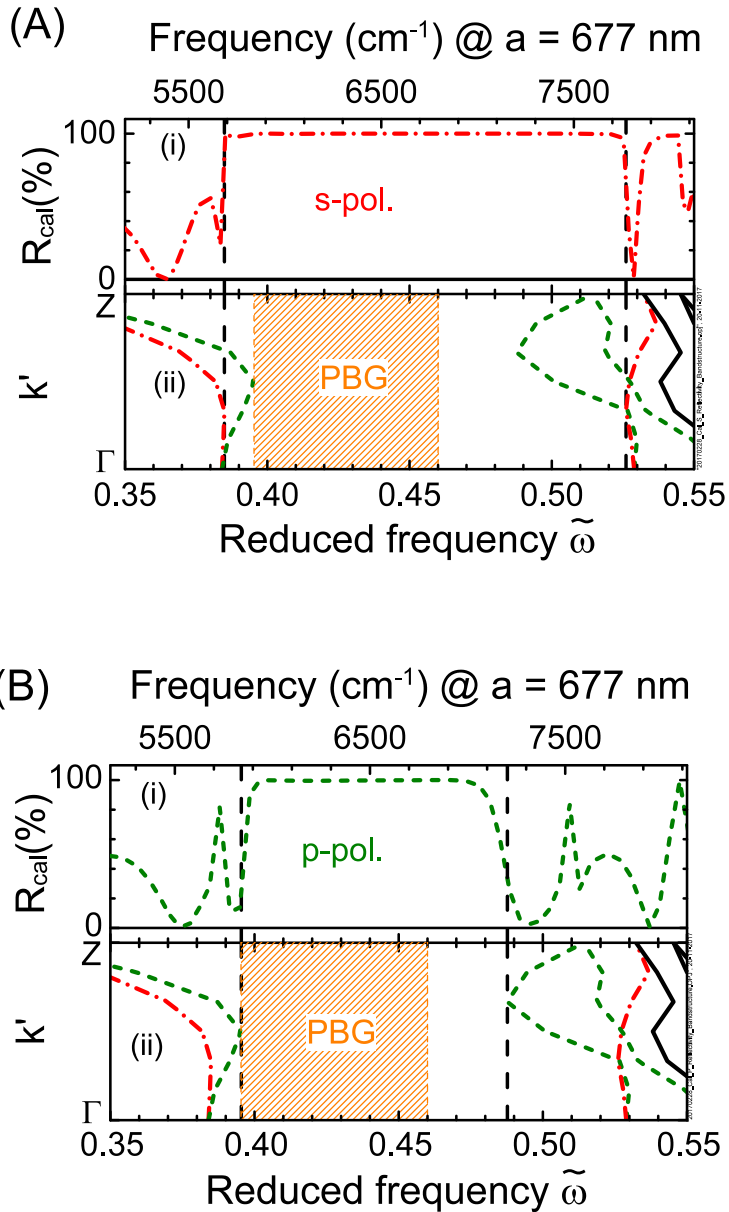
Figure 2.7: Reflectivity near the stop band for (A) *s*- and (B) *p*-polarized light for Si inverse woodpile crystals. In panels (i), red dashed-dotted and green dashed curves are calculated results, as in Fig. 2.6. Panels (ii) show the band structures for (A) *s*- and (B) *p*-polarized light, where the 3D band gap is shown in orange. The wave vector is expressed as $k' = (ka/2\pi)$. The vertical black dashed lines indicate the edges of the stop band (i) and the matching stop gap edges (ii). Near the stop gap edges, we identify *s* bands (red dashed-dotted curves) and *p* bands (green dashed curves).

2.3.2 Frequency-resolved reflectivity at normal incidence

We have performed an extensive set of polarization-resolved (s or p) reflectivity calculations at normal incidence to the photonic crystal slab that corresponds to a typical experimental geometry [6–9, 11, 15, 35, 36] and since this high-symmetry geometry facilitates data interpretation. Since similar inverse woodpile structures were studied in our group [15], we tuned the parameters to this study, namely a smaller pore radius ($\frac{r}{a} = 0.19$) and a dielectric permittivity $\epsilon = 12.1$, typical for silicon in the near infrared and telecom ranges [15, 18]. Figure 2.6 shows spectra for a thin crystal with a thickness $L = 4c$. Fabry-Pérot fringes are visible for both polarizations in Fig. 2.6 ((i), (iii)) corresponding to standing waves in the finite crystal. The strong reflectivity peaks near $\tilde{\omega} = 0.45$ indicate stop bands for both s and p polarizations. The stop bands at normal incidence appear at a lower frequency than in Fig. 2.4 since the air fraction is less and hence the average index of the crystal is greater. The p-stop band appears between $\tilde{\omega} = 0.395$ and $\tilde{\omega} = 0.488$ with a broad relative bandwidth 21 %. The s-stop band appears between $\tilde{\omega} = 0.385$ and $\tilde{\omega} = 0.526$ and it is about $1.5\times$ broader (relative bandwidth 31 %) than the p-stop band. At frequencies beyond $\tilde{\omega} = 0.55$ several bands of high reflectivity appear. In these frequency bands the band structures reveal extremely complex couplings of multiple Bragg conditions [37] that lead to complex band structures that are sometimes also referred to as "*spaghetti-like*" behavior. Thus these apparent stop bands can be caused by the uncoupled modes of plane waves outside crystals, or by modes whose dispersion relation restricts impedance matching to waves outside the crystal.

The frequency ranges of the s- and the p-stop bands agree very well with corresponding stop gaps in the photonic band structure. Such a comparison allows us to assign the polarization character without need to compute eigen functions. Since the 3rd photonic band at the lower stop gap edge (near $\tilde{\omega} = 0.385$) agrees with the lower boundary of the s-stop band, we conclude that this band has dominantly s character. Furthermore, the 4th band is located inside the s-stop band and agrees with the lower edge of the p-stop band at $\tilde{\omega} = 0.395$. Therefore, we conclude that this band must have dominantly p character. Near the upper gap edge, the 7th band near $\tilde{\omega} = 0.526$ agrees with the upper s-stop band edge and is thus likely an s band. The 5th and 6th bands between $\tilde{\omega} = 0.49$ and $\tilde{\omega} = 0.526$ are situated well inside the s-stop band and can therefore only have p character; indeed, these bands lie outside the p-stop band. This assignment of bands 5, 6, and 7 is further supported by the observation that band 7 crosses bands 5 and 6 at $\tilde{\omega} = 0.526$, without revealing avoided crossings.

2.3.3 Frequency-resolved reflectivity through a numerical aperture

A recent experimental study by our group reported the signature of a 3D photonic band gap in silicon inverse woodpile crystals [15]. The signature consists of observing overlapping stop bands for a large solid angle of $(1.76 \pm 0.18)\pi$. The experiments were performed on crystals with an extent of $L^3 = 12^3$ unit cells on
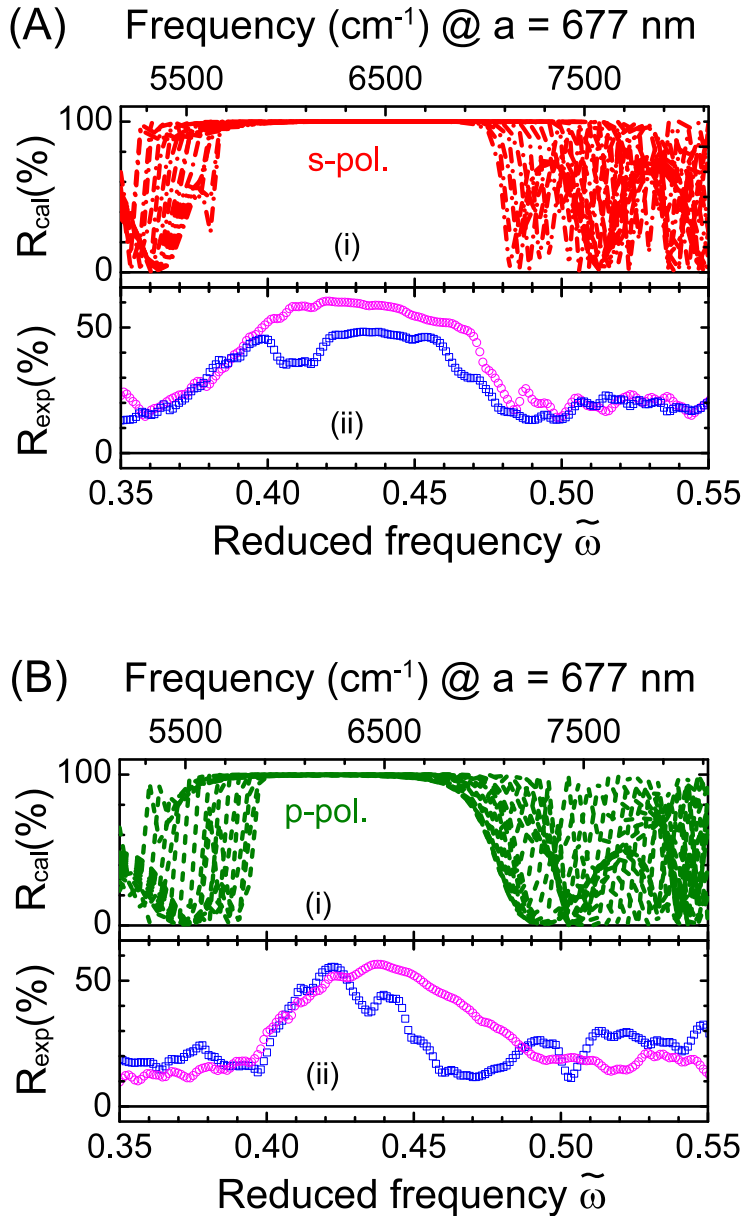
**Figure 2.8:** Comparison between numerical calculations and experimental results for the reflectivity peaks near the stop band for (A) *s*- and (B) *p*-polarized light for Si inverse woodpile crystals. Panels (i) show the calculated results, where red dashed-dotted and green dashed curves are reflectivity spectra for angles of incidence from 6° to 40° off normal in the ΓZ direction as well as in the equivalent ΓX direction. In panels (ii), blue squares are measurements from Ref. 15 in the ΓZ direction, and magenta circles in the equivalent ΓX direction. The top ordinate shows the frequency in wavenumbers (cm^{-1}) for a lattice parameter $a = 677$ nm as in the experiments.

top of bulk silicon. Polarization-resolved reflectivity spectra were measured using a reflecting objective with NA = 0.65 and Obscuration = 13.3%. Thus, the incident light has an angular spread from about 6° to 40° off normal. To accurately mimic the NA of a microscopic objective in an experiment, calculations should be performed for all wave vectors within the solid angle of the conical incident beam. Moreover, one should calculate fields and add these coherently to mimic the focusing by the objective, before taking the absolute square to obtain the intensity as in the experiments [15]. Since this procedure is currently prohibitively computer expensive, we approximate this angular spread of the incident and collected light without an attempt to average. We calculated reflectivity spectra for angles of incidence from 6° to 40° off normal in the YZ plane for each polarization, see Fig. 2.8. We observe strong angle-dependent reflectivity variations near the lower and the upper edges of the stop band. The intense angle-independent reflectivity peaks near $\tilde{\omega} = 0.45$ indicate the stop bands for both s and p polarizations. A comparison between the angle-independent high reflectivity ranges (Fig. 2.8) and the angle-resolved reflectivity spectra centered at 0° (Fig. 2.7) shows that there are shifts and changes in stop band widths. For s polarization, the stop band edge at half height shifts from $\tilde{\omega} = 0.385$ to 0.383 (lower edge) and from $\tilde{\omega} = 0.526$ to 0.48 (upper edge), hence the stop band center shifts down from $\tilde{\omega} = 0.455$ to 0.432, and the width narrows from $\Delta\tilde{\omega} = 0.141$ to 0.097.

We now compare the measured spectra for the stop bands in the ΓX and the ΓZ directions with the angle-independent calculated intense reflectivity peak, as shown in Fig. 2.8. In particular, we discuss the central frequency, the band width, and the maximum reflectivity. In the ΓX and the ΓZ directions, the central frequencies for s polarization and p polarization in the calculation and in the experiment agree well to nearly within both error bars [38]. From the Bragg diffraction condition [26], the central frequency ω_c in terms of the effective index is

$$\omega_c = \frac{1}{n_e}\frac{m\pi c}{L}, \tag{2.1}$$

with m the integer diffraction order. From the good agreement of the central frequencies, we deduce from Eq. 2.1 that n_e in the calculations ($n_e = 2.28$) is close to the one in the experiments. Therefore, we conclude that the total volume fraction of the high-index material (Si) in the calculations matches with the experimental one.

Figure 2.8 (A) shows that for s polarization, the bandwidths in the calculation and in the experiment in the ΓX direction agree well to nearly within both error bars. The comparison of the band widths in the calculation and in the experiment in the ΓZ direction exhibits a small difference for s polarization, which is outside the specified error bars [39]. Figure 2.8 (B) shows that for p polarization, in the ΓX direction the calculated band width agrees well to the measured band width to nearly within both error bars. In the ΓZ direction, the comparison of bandwidths in the calculation and in the experiment a exhibits small difference for p polarization, outside the specified error bars [40]. Therefore, the calculated band width and the measured band width agree in ΓX direction, but disagree in ΓZ direction for both polarizations. The experimental results in Fig. 2.8 show

that the band width for the ΓZ direction is smaller than the band width for the ΓX direction. The band width for 3D silicon inverse woodpile photonic crystals increases with increasing pore radius to a maximum at pore radius $\frac{r}{a} = 0.245$ in the gap map in Ref. 15. Therefore, the band width for the ΓZ direction can be smaller than the band width for the ΓX direction if the pore radius in the ΓZ direction is smaller than the one in the ΓX direction for these crystals. The fabrication process could result in different pore radii $\frac{r}{a}$ in the ΓZ and the ΓX directions. We surmise that the $\frac{r_{\Gamma Z}}{a}$ ratio is smaller than $\frac{r}{a} = 0.19$, whereas the $\frac{r_{\Gamma X}}{a}$ ratio is larger than $\frac{r}{a} = 0.19$, but smaller than optimal optimal pore size $\frac{r}{a} = 0.245$ [15]. Simultaneously, the total volume fraction is apparently constant in view of the central frequencies above. Therefore, we hypothesize that the difference in measured reflectivity spectra for two symmetry-related directions ΓX and ΓZ is due to the fabrication process resulting in different pore radii for these directions. Hence, our calculations reveal that an angle-independent strong reflectivity spectrum over an angular spread of the incident light for a certain experiment provides an improved interpretation of the reflectivity measurements and an insight in the crystal structure.

Figure 2.8 shows marked differences between the maximum reflectivity in calculations and in experiments. In the experimental work, the limited maximum reflectivity (67%) was attributed to the finite thickness of the crystal, to angle of incidence, and to surface roughness, although no theoretical or numerical support was offered for these notions. In reflectivity spectra shown in Fig. 2.6 and Fig. 2.9 (explained below in section 2.3.4), we observe strong reflectivity peaks even for thin crystals. This implies that the finite size is not a critical limiting factor for reflectivity. Fig. 2.4(A) and Fig. 2.4(B) show that the observed stop bands hardly change with angle of incidence. This observation supports the experimental assertion that intense reflectivity peaks measured with an objective with a large numerical aperture provide a faithful signature of the 3D photonic band gap. Extensive numerical studies are called for in order to ascertain the impact of roughness of the crystal-air interface, as well as roughness inside the pores.

2.3.4 Finite-size effects: Bragg attenuation length

To investigate the effect of finite thickness of the crystal, we calculated the transmission for thicknesses between $L = 1c$ to $10c$. Figure 2.9 shows that for a given frequency inside the stop gap, the transmission decays exponentially for both s and p polarizations. For frequencies below or above the stop gap, the transmission is nearly constant, with some small variations with crystal thickness as a result of the Fabry-Pérot fringes that vary with crystal thickness, as is well-known for 1D Bragg stacks [33, 41].

Inside a stop gap the complex wave vector k has a nonzero imaginary component $\mathbb{Im}(k)$ since the waves are damped by Bragg diffraction interference [8, 33, 42]. Thus, we write the transmission T in a stop band as [43–45]

$$T(\omega, L) = exp\left(-\frac{L}{L_B(\omega)}\right),\qquad(2.2)$$

with L_B the Bragg attenuation length equal to

$$L_B(\omega) = \frac{1}{2\mathbb{Im}(k)(\omega)} \qquad (2.3)$$

that gives the distance covered by incident light until it has exponentially decayed to a fraction $1/e$. Figure 2.9 reveals that even inside the stop band the transmission shows modulations, as was previously identified in $1D$ stacks [33, 41]. The reason is that transmission also contains the effects of both front and back crystal surfaces.

The Bragg attenuation length is usually expressed in terms of the distance between lattice planes d_{hkl}. Therefore, we reduce the Bragg length to the $\{hkl = 220\}$ lattice spacing d_{220} that equals $d_{220} = c/2$. The s-polarized data in Fig. 2.9 agree well with Eq. (2.2) with a slope that yields a Bragg attenuation length $L_B = 0.74d_{220}$. For the p-polarized data in Fig. 2.9, we obtain a Bragg attenuation length $L_B = 1.21d_{220}$ at the gap center, which is about $1.5\times$ larger than for s polarization at the gap center. This observation agrees quantitatively with the reflectivity spectrum where the s-polarized stop band is also $1.5\times$ broader than the p-polarized stop band (see Fig. 2.6). This behavior can be understood as follows: The Bragg attenuation length at the center frequency of a stop gap of a Bragg stack satisfies [46]

$$L_B = \frac{2d}{\pi S} \simeq \frac{2d}{\pi} \frac{\omega_c}{\Delta\omega}. \qquad (2.4)$$

The photonic interaction strength S is defined as the polarizability per volume of a unit cell [47, 48] and is estimated from the relative frequency band width of the stop band for a dominant reciprocal lattice vector as $S \approx \frac{\Delta\omega}{\omega_c}$ [46]. We find that the Bragg lengths are shorter by a factor 6 to 9 than the earlier experimental estimate in Ref. 15 that was derived from the width of the stop bands. Hence, crystals with a thickness of 12 unit cells studied in these experiments are effectively in the thick crystal limit since $\frac{L}{L_B} = 5$ to 8. Regarding the reason why the Bragg length obtained from the stop band width (Eq. (2.4)) differs from the Bragg length determined from the thickness-dependent transmission (Eq. (2.2)), we speculate that Eq. (2.4) pertains to a simple stop gap typical of a Bragg stack with only one band below and one band above the gap whose Bloch-state repulsion yields a gap at wave vectors equal to the Brillouin zone boundary,[26] in notable absence of multiple Bragg diffraction [50]. In contrast, Figure 2.7(A,B) show that the dominant stop gap is bounded by multiple Bragg behavior, as is apparent from the pertinent elevated Miller indices (see section 2.4.1), and since the gap is bounded by bands at wave vectors inside the Brillouin zone (not the zone boundary). Since multiple Bragg diffraction is known to lead to frequency and wave vector shifts of gaps, as well as changes of gap widths, it is quite conceivable that in this situation Eq. (2.4) is not equivalent anymore to Eq. (2.2).
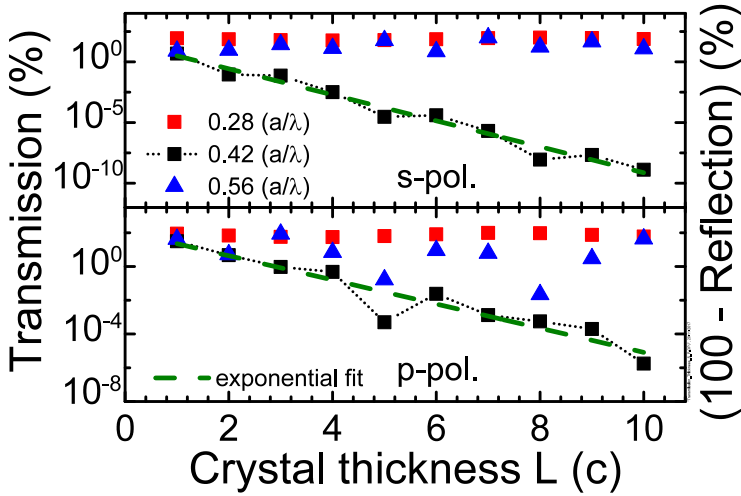
Figure 2.9: Transmission versus thickness for a silicon inverse woodpile photonic crystal in the ΓZ direction for s (top) and p polarizations (bottom). Red squares, black circles and blue triangles pertain to frequencies below, inside, and above the stop gap, respectively. The green dashed lines are the exponential decay of transmission with crystal thickness at frequencies in the stop gap (Eq. (2.2)). The black dashed line is a guide to the eye that shows modulations in the stop band.

2.4 Discussion

2.4.1 Role of geometrical structure factor

The polarization-resolved reflectivity spectra for the cubic diamond-like inverse woodpile structure in Fig. 2.6 reveal Fabry-Pérot fringes that correspond to standing waves in the periodically layered finite crystal. There are three corollaries based on theory for a periodic layered Bragg reflector with a thickness of N unit cells [33]. First, a reflectivity peak occurs at the center of the stop gap. Second, between any two stop gaps there are exactly $(N-1)$ troughs in the reflectivity spectra. Third, there are exactly $(N-2)$ side lobes to the reflectivity peak.

The band structure in Fig. 2.6 (ii) shows two stop gaps in the ΓZ direction. A narrow stop gap appears near $\tilde{\omega} = 0.311$ and the broad stop gap appears near $\tilde{\omega} = 0.39$. We now interpret the spectra in Fig. 2.6 (i), (iii) for $N = 4$ unit cells in terms of the 3 corollaries above. For s polarization reflectivity in Fig. 2.6 (i), we observe a peak near $\tilde{\omega} = 0.45$, at the center of the second stop gap. Surprisingly, there is no peak near the center of the first stop gap at variance with the 1st corollary. This spectrum reveals 4 troughs between zero frequency and the first stop gap, the 5th trough near the center of the first stop gap and 2 troughs between the first and second order stop gap; which seems mutually inconsistent and at variance with the 2nd corollary. For p-polarized reflectivity in Fig. 2.6 (iii), we observe a reflectivity peak near the $\tilde{\omega} = 0.45$, which corresponds

to the center of the second stop gap. Also, no reflectivity peak appears near the center of the first stop gap, at variance with the 1st corollary. In this spectrum, there are 4 troughs between zero frequency and the first stop gap, and 3 troughs between the first and second order stop gap; which seems mutually inconsistent and at variance with the 2nd corollary. Therefore, the above observations for p-polarization do not agree with the observations for s-polarization.

To remedy this seeming disagreement, we consider the geometrical structure factor $S_{\mathbf{K}}$ that indicates the degree to which interference of waves scattered from identical ions within the crystal basis inside the unit cell affect the intensity of a Bragg peak associated with reciprocal lattice vector $\mathbf{K}$ [26]. Since the intensity of the Bragg peak is proportional to the square of the absolute value of $S_{\mathbf{K}}$, the Bragg peak vanishes when $S_{\mathbf{K}}$ vanishes. For a conventional cubic unit cell of the monatomic diamond structure, $S_{\mathbf{K}} = 0$ if the sum of Miller indices equals twice an odd number n: $h + k + l = 2n$. In Fig. 2.6, the stop gap near $\tilde{\omega} = 0.31$ in ΓZ direction corresponds to a first-order stop gap for $\{hkl = 110\}$ lattice planes in the conventional diamond structure [26]. Since the sum of Miller indices in $\{110\}$ is twice the odd number 1, the first-order stop gap in the cubic inverse woodpile photonic structure has zero geometrical structure factor ($S_{\mathbf{K}} = 0$) and hence zero associated Bragg reflection. If the sum of Miller indices ($h + k + l$) is twice an even number, $S_{\mathbf{K}}$ is maximum and equals $S_{\mathbf{K}} = 2$. The stop gap near $\tilde{\omega} = 0.4$ in Fig. 2.6 is a second-order stop gap for $\{hkl = 110\}$ and corresponds to $\{hkl = 220\}$ defined using X-ray diffraction in a conventional cubic diamond structure [26]. Since the sum of Miller indices in $\{220\}$ equals twice an even number, the second-order stop gap has $S_{\mathbf{K}} \neq 0$. Therefore, the second-order stop gap has a maximal structure factor. Hence, only the second-order stop gap in a cubic diamond-like inverse woodpile structure reveals appreciable Bragg reflection and should therefore be considered for the analysis of the observed Fabry-Pérot fringes in the reflectivity spectra.

The distance between lattice planes equals $d_{220} = c/2$ for the dominant second-order stop gap with Miller indices $\{hkl = 220\}$. Therefore, the $L = 4c$ crystal thickness used in the computational cell in Fig. 2.6 corresponds to a thickness $L = N d_{220} = 8 d_{220}$ in terms of a periodic layered medium (a Bragg stack) [33]. In Fig. 2.6, we observe reflectivity peaks near $\tilde{\omega} = 0.45$ for s and p polarizations, which are at the center of the s- and p-stop gaps. This satisfies the first corollary for the periodic layered medium. Secondly, there are exactly $(N - 1) = 7$ troughs in the reflectivity spectra between zero frequency and the main stop gap corresponding to $N = 8$ lattice planes in the crystal, in agreement with the second corollary above. Thirdly, there are $(N - 2) = 6$ side lobes in the reflectivity spectra, again agreeing with $N = 8$ lattice planes by the third corollary. These three corollaries confirm that the number of Fabry-Pérot fringes in our reflectivity spectra agrees with the theory for a Bragg reflector [33]. Moreover, this episode reminds us that it is the number of lattice planes that is fundamental in the thickness of a finite crystal, rather than the number of unit cells.

2.4.2 Comparison to other inverse woodpiles and woodpiles

The silicon inverse woodpile photonic crystal studied in Ref. 10 has a 3D structure consisting of two interpenetrating hexagonal pore sets that corresponds to an orthorhombic symmetry. Therefore, the first Brillouin zone is distorted compared to the Brillouin zone of an fcc lattice. This study reported reflectivity spectra in one high-symmetry direction using unpolarized light. The strong reflectivity peak denotes the stop band along the z-direction. The stop band is shown to agree with the stop gap obtained from the band structure. Since the crystal has orthorhombic symmetry, the ΓX stop gap is not symmetry related in k-space to the ΓZ stop gap. Therefore, the stop band is representative for a limited range of solid angles. The limited reflectivity was attributed to the numerical aperture, to surface roughness, and to roughness at the pore walls.

The silicon woodpile photonic crystals studied in Ref. 11 has lattice parameters in a ratio $\frac{c}{a} = 1.15$, hence the crystals are not cubic but tetragonal. This study reports reflectivity spectra in one high symmetry direction. To mimic the angular spread of the incident light in the experiments, reflectivity spectra were calculated for many incident angles in the relevant range and averaged over the obtained results. It is unknown whether this average includes the coherent field addition and the NA-filling that is needed to compare to experiments (see section 2.3.3). A qualitative agreement between the stop band observed in experiment, the stop band identified from calculation, and the stop gap calculated from the band structure is found. The maximum observed reflectivity is accredited to measurement limitations, to unspecified deviations from perfect periodicity and to surface roughness. Since the crystal is not cubic, the ΓX stop gap is not symmetry-related to the ΓZ stop gap. Therefore, the stop band is representative for a limited range of solid angles. The polarization of the light used in the calculation of reflectivity spectra is unspecified, so polarization character cannot be attributed to the bands by comparing reflectivity spectra with the band structure. Nevertheless, the calculated reflectivity spectra reveal Fabry-Pérot fringes at wavelengths above the stop band that correspond to standing waves in the finite-sized crystal, as also seen in Fig. 2.4. The number of unit cells in the structure is unspecified, so it is not feasible to verify the theory for a periodic layered Bragg reflector for the number of Fabry-Pérot fringes. The calculations were reported for a fixed crystal thickness, so the Bragg attenuation length was not deduced. Since the calculated reflectivity spectra are angle averaged, a possible Brewster angle is not visible. Our calculations have shown that the finite size deviation from the perfect periodicity is not responsible for the limited maximum reflectivity. Thus, we conclude that the the maximum observed reflectivity is likely limited by the invoked measurement limitations and surface roughness.

2.4.3 Back reflector for solar cells

The efficiency of silicon photovoltaic cells critically depends on efficient ways to trap and absorb light [51, 52]. It remains a challenge to have thin film c-Si solar cells trap a significant part of solar energy [12]. Increasing wafer thickness results in longer diffusion lengths, but increases costs. Traditionally, light trapping in

solar cells rest on controlling light ray paths using geometrical optics, *e.g.*, by scattering incident light via surface texturing and back reflection into the solar cells via a reflector. In practice, perfect scattering and reflection are difficult to obtain, which limits the attainable efficiency and power generation of solar cells. Recently, it has been shown that the light trapping approaches based on wave optics outperform all geometrical optics approaches for a certain range of frequencies [53]. One can employ specially nanodesigned structures, such as 3D photonic crystals, notably those with a complete 3D photonic band gap.

The results in Fig. 2.9 reveal that a reflectivity in excess of $R > 99$ % (hence $T < 1$ %) is found inside the stop band already for thin 3D silicon photonic band gap crystals, with a thickness as small as $L \geq 2c$ for s polarization, and $L \geq 3c$ for p polarization. In addition, by combining Figs. 2.4(A) and 2.4(B), we note that an angle- and polarization-independent range of high reflectivity appears between $\tilde{\omega} = 0.4962$ and $\tilde{\omega} = 0.6379$ with a broad 25% relative bandwidth, much more than is predicted for (even thicker) 1D Bragg stacks [33]. Hence, our calculations support the assertion that a 3D silicon photonic crystal could serve as an efficient back reflector in a solar cell in order to enhance the efficiency.

2.5 Conclusions

We have studied by numerical simulation the reflectivity of 3D photonic crystals with a $3D$ complete photonic band gap, to interpret recent experiments. We employed the finite element method to study crystals with the cubic diamond-like inverse woodpile structure, with a dielectric function similar to silicon. The crystals are surrounded by vacuum, and thus have a finite support as in the experiments. We observe that the stop band hardly changes with incident angle, which supports the experimental notion that strong reflectivity peaks measured with large numerical aperture gives a faithful signature of the 3D band gap. We observe an intriguing hybridization of the Fabry-Pérot resonances and the Brewster angle in our calculations, which seems a characteristic property of 3D photonic band gap crystals. From the intense reflectivity peaks, we infer that the maximum reflectivity observed in the experiments is not limited by finite size of the crystal. Our calculated polarization-resolved reflectivity spectra show that the frequency ranges of the s- and p- stop bands agree well with the corresponding stop gaps in the photonic band structure. From the comparison we assign bands in the band structure near these stop bands to have dominantly s or $p$character. The comparison between angle-independent numerical calculations and experimental results provides an improved interpretation of the reflectivity measurements and a new insight in the crystal structure (unequal pore sizes in different directions). We find that the Bragg attenuation lengths in the stop bands are smaller than the earlier estimates based on the width of the stop band by a factor of 6 to 9. Our results indicate that 3D silicon photonic band gap crystals merit study as possible candidates for back reflectors in a solar cell in order to enhance the photovoltaic efficiency.
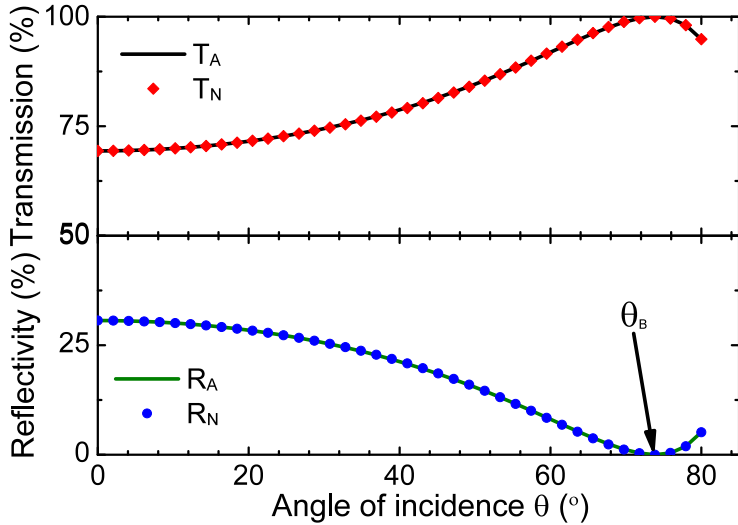
Figure 2.10: Analytical calculation versus numerical computation for reflection and transmission spectra of semi-infinite dielectric medium for p polarization. The medium has dielectric permittivity $\epsilon = 12.1$. The analytically calculated reflectivity (R_A) and transmission (T_A) are shown in green and black lines, respectively. Blue circles and red diamonds represent the numerically computed reflectivity (R_N) and transmission (T_N), respectively. θ_B denotes the Brewster angle.

2.A Analytical validation of the numerical scheme with a semi-infinite homogeneous medium

To validate our numerical scheme, we calculate reflectivity spectra of a system that can be analytically analyzed using Fresnel's equations, namely a homogeneous dielectric medium [54]. We consider p-polarized plane waves at a single frequency with a range of angles of incidence. We replace the photonic crystal and the air layer on the right in Fig 3.2 (A) with a medium with dielectric permittivity $\epsilon = 12.1$. This results in a semi-infinite homogeneous medium that is separated from the source by an air layer. The finite element mesh used in the numerical calculation consists of 18732 tetrahedra per crystal unit cell (unit cell defined in terms of the lattice parameter c), somewhat less than the number of tetrahedra in the finite element mesh used for the 3D photonic crystal. The angular resolution is $2°$.

In Fig. 2.10, we show the calculated reflectivity and transmission spectra of a semi-infinite homogeneous medium for the above defined computational cell. We note that the numerical calculation agrees very well with the analytical calculation. We observe the Brewster angle at $\theta_B = 74°$, which matches the value obtained from an analytical calculation [54]. To calculate the relative error δT_{rel} between the numerical calculation and the analytical result, we employ the defi-
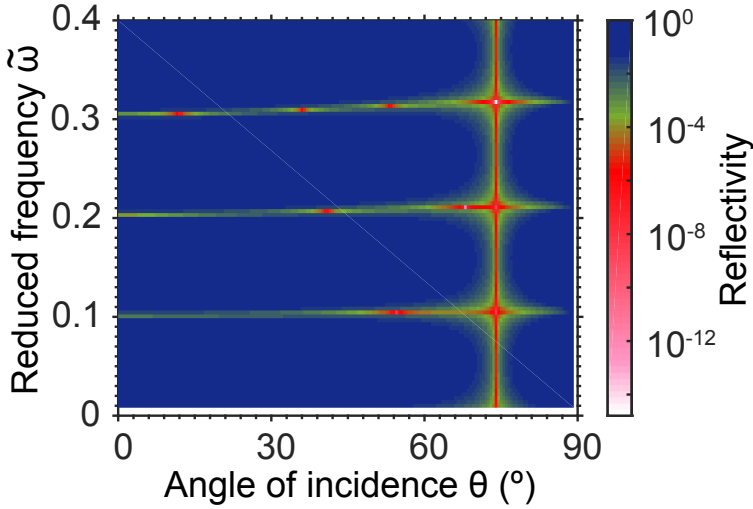
Figure 2.11: Analytically calculated angle- and frequency-resolved reflectivity spectra
of a thin dielectric film for p polarization. The film has a dielectric permittivity $\epsilon = 12.1$.
The Brewster angle at $\theta_B = 73°$ is constant with frequency.

nition

$$\delta T_{rel} \equiv \frac{1}{n} \sqrt{\left(\sum_{i=1}^{n} \left(\frac{(T_{A,i} - T_{N,i})^2}{T_{A,i}^2} + \frac{(R_{A,i} - R_{N,i})^2}{R_{A,i}^2} \right) \right)} \qquad (2.5)$$

with $(T_{N,i}, R_{N,i})$ the numerical transmission and reflectivity, and $(T_{A,i}, R_{A,i})$ the
analytical transmission and reflectivity. For the solution shown in Fig. 2.10, the
error is only about $\delta T_{rel} = 6 \times 10^{-4}$, hence we consider the calculation to be
converged.

2.B Brewster angle for a thin film

To find the dependence of the Brewster angle on frequency, we have analytically
calculated the angle-resolved and frequency-resolved spectra for a thin film [55].
We consider p-polarized incident waves for angles of incidence up to 89° off the
normal. Figure 2.11 shows Fabry-Pérot fringes corresponding to the standing
waves in the thin dielectric film. We note that the Fabry-Pérot fringes have a
nearly constant frequency for all angles of incidence. We observe a Brewster angle
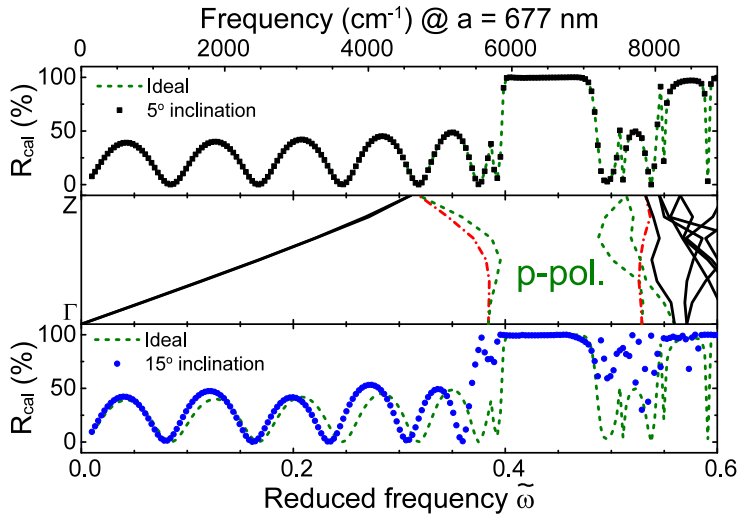at $\theta_B = 73°$ that is independent of frequency, as expected for a dispersionless
film.

Figure 2.12: Reflectivity spectra for a 3D inverse woodpile photonic band gap crystal with one set pores in the X direction and a second set of pores at an angle θ off the normal in the Z direction. Black squares in panel (i) and blue circles in (iii) are calculated at normal incidence for p polarization for $\theta = 5°$ and $\theta = 15°$, respectively. Green dashed curves in (i) and (iii) are reflectivity spectra calculated for an ideal crystal. The corresponding band structure of an ideal crystal for the ΓZ direction is shown in panel (ii). The wave vector is expressed as $k' = (ka/2\pi)$. The polarization character of bands near the gap is assigned in Fig. 2.7.

2.C Monoclinic deformation of a 3D inverse woodpile photonic crystal

During the fabrication of 3D inverse woodpile photonic crystals, the second set of pores can be angularly misaligned with respect to the already fabricated first set of pores, *e.g.*, due to the misaligned sample with respect to the focused ion beam [18]. Thus, there will be two 2D arrays of non-orthogonal pores in the crystal structure. Ref. 18 studied the influence of fabrication deviations on the photonic band gap by calculating the band structures for periodic structures. The long-range periodic order of the three-dimensional inverse woodpile is disrupted for non-orthogonal pores and hence Ref. 18 could not determine the impact on the photonic band gap.

To investigate the impact of the monoclinic deformation on a 3D inverse woodpile crystal with finite support, we calculate frequency-resolved p-polarized reflectivity spectra for a structure with one set of pores in the X direction and a second set of pores at an angle θ off the normal in the Z direction, which happens to be the direction of the incident plane wave in Fig. 3.2.

Building on our calculations for ideal crystals in Section 2.3.2, we compare in Fig. 2.12 the reflectivity spectra with and without inclination of the set of pores in

the Z direction. We observe below $\tilde{\omega} = 0.4$ in the top panel of Fig. 2.12 that the reflectivity spectrum for a photonic crystal with an inclination $\theta = 5°$ matches very well with the one for an ideal photonic crystal. However, a comparison between the spectrum for a photonic crystal with an inclination $\theta = 15°$ and for an ideal crystal shows that there are shifts and changes in the stop band widths. The $p-$stop band edge at half height shifts from $\tilde{\omega} = 0.395$ to 0.388 (lower edge), the stop band center shifts down from $\tilde{\omega} = 0.442$ to 0.438, and the width slightly widens from $\Delta\tilde{\omega} = 0.093$ to 0.1. Remarkably, the upper edge of the stop band remains invariant even with an inclination $\theta = 15°$. We note below $\tilde{\omega} = 0.39$ that the inclination $\theta = 15°$ changes amplitudes of existing Fabry-Pérot fringes and shifts them to lower frequencies. Since the deformation in fabrication for a 3D inverse woodpile photonic crystal typically remains below $\theta = 5°$ [18], we surmise that the effect of the monoclinic deformation on the stop band will be negligible.

A plane wave incident in the Z direction of a 3D inverse woodpile photonic crystal experiences a dielectric contrast, which is major due to the pores in the X direction and minor due to the pores in the Z direction. However, periodic boundaries employed in $-X$ and $+X$ directions of our computational cell prohibit the reflectivity calculation with pores inclined off the normal in X direction. Therefore, we need to employ the supercell method to study the monoclinic deformation of the pores orthogonal to incident plane wave, which remains open for future studies.

Bibliography

[1] A. F. Koenderink, L. Bechger, H. P. Schriemer, A. Lagendijk, and W. L. Vos, "Broadband fivefold reduction of vacuum fluctuations probed by dyes in photonic crystals," Phys. Rev. Lett. **88**, 143903 (2002). 25

[2] S. Ogawa, M. Imada, S. Yoshimoto, M. Okano, and S. Noda, "Control of Light Emission by 3D Photonic Crystals," Science **305**, 227 (2004). 25

[3] P. Lodahl, A. F. van Driel, I. S. Nikolaev, A. Irman, K. Overgaag, D. Vanmaekelbergh, and W. L. Vos, "Controlling the dynamics of spontaneous emission from quantum dots by photonic crystals," Nature (London) **430**, 654 (2004). 25

[4] M. D. Leistikow, A. P. Mosk, E. Yeganegi, S. R. Huisman, A. Lagendijk, and W. L. Vos, "Inhibited spontaneous emission of quantum dots observed in a 3D photonic band gap," Phys. Rev. Lett. **107**, 193903 (2011). 25

[5] J. G. Fleming, and S. -Y. Lin, "Three-dimensional photonic crystal with a stop band from 1.35 to 1.95 μm," Opt. Lett. **24**, 49 (1999). 25

[6] A. Blanco, E. Chomski, S. Grabtchak, M. Ibisate, S. John, S.W. Leonard, C. Lopez, F. Meseguer, H. Miguez, J. P. Mondia, G. A. Ozin, O. Toader, and H. M. van Driel, "Large-scale synthesis of a silicon photonic crystal with a complete three-dimensional bandgap near 1.5 micrometres," Nature (London) **405**, 437 (2000). 25, 34

[7] S. Noda, K. Tomoda, N. Yamamoto, and A. Chutinan, "Full three-dimensional photonic bandgap crystals at near-infrared wavelengths," Science **289**, 604 (2000). 25, 34

[8] Y. A. Vlasov, X. Bo, J. C. Sturm, and D. J. Norris, "On-chip natural assembly of silicon photonic bandgap crystals," Nature (London) **414**, 289 (2000). 25, 34, 37

[9] G. Subramania and S. -Y. Lin, "Fabrication of three-dimensional photonic crystal with alignment based on electron beam lithography," Appl. Phys. Lett. **85**, 5037 (2004). 25, 34

[10] J. Schilling, J. White, A. Scherer, G. Stupian, R. Hillebrand, and U. Gösele, "Three-dimensional macroporous silicon photonic crystal with large photonic band gap," Appl. Phys. Lett. **86**, 011101 (2005). 25, 41

[11] I. Staude, M. Thiel, S. Essig, C. Wolff, K. Busch, G. Von Freymann, and M. Wegener, "Fabrication and characterization of silicon woodpile photonic crystals with a complete bandgap at telecom wavelengths" Opt. Lett. **35**, 1094 (2010). 25, 34, 41

[12] J. D. Joannopoulos, S. G. Johnson, J. N. Winn, and R. D. Meade, *"Photonic crystals: Molding the flow of light,"* (Princeton University Press, Princeton NJ,

2008). 25, 27, 41

[13] W. M. Robertson, G. Arjavalingam, R. D. Meade, K. D. Brommer, A. M. Rappe, and J. D. Joannopoulos, "Measurement of photonic band structure in a two-dimensional periodic dielectric array," Phys. Rev. Lett. **68**, 2023 (1992). 25

[14] K. Sakoda, "Symmetry, degeneracy, and uncoupled modes in two-dimensional photonic lattices," Phys. Rev. B **52**, 7982 (1995). 25

[15] S. R. Huisman, R. V. Nair, L. A. Woldering, M. D. Leistikow, A. P. Mosk, and W. L. Vos, "Signature of a three-dimensional photonic band gap observed with silicon inverse woodpile photonic crystals," Phys. Rev. B **83**, 205313 (2011). 25, 31, 34, 35, 36, 37, 38

[16] K. M. Ho, C. T. Chan, C. M. Soukoulis, R. Biswas, and M. Sigalas, "Photonic band gaps in three dimensions: new layer-by-layer periodic structures," Solid State Commun. **89**, 413 (1994). 25, 26

[17] R. Hillebrand, S. Senz, W. Hergert, and U. Gösele, "Macroporous-silicon-based three-dimensional photonic crystal with a large complete band gap," J. Appl. Phys. **94**, 2758 (2003). 25, 26

[18] L. A. Woldering, A. P. Mosk, R. W. Tjerkstra, and W. L. Vos, "The influence of fabrication deviations on the photonic band gap of three-dimensional inverse woodpile nanostructures," J. Appl. Phys. **105**, 093108 (2009). 25, 26, 34, 45, 46

[19] F. García-Santamaría, M. Xu, V. Lousse, S. Fan, P. V. Braun, and J. A. Lewis, "A germanium inverse woodpile structure with a large photonic band gap," Adv. Mater. **19**, 1567 (2007). 25

[20] A. Hermatschweiler, A. Ledermann, G. A. Ozin, M. Wegener, and G. von Freymann, "Fabrication of silicon inverse woodpile photonic crystals," Adv. Funct. Mater. **17**, 2273 (2007). 25

[21] B. Jia, S. Wu, J. Li, and M. Gu, "Near-infrared high refractive-index three-dimensional inverse woodpile photonic crystals generated by a sol-gel process," J. Appl. Phys. **102**, 096102 (2007). 25

[22] T. Tajiri, S. Takahashi, Y. Ota, J. Tatebayashi, S. Iwamoto, and Y. Arakawa, "Demonstration of a three-dimensional photonic crystal nanocavity in a < 110 >-layered diamond structure," Appl. Phys. Lett. **107**, 071102 (2015). 25

[23] L. A. Woldering, R. W. Tjerkstra, H. V. Jansen, I. D. Setija, and W. L. Vos, "Periodic arrays of deep nanopores made in silicon with reactive ion etching and deep UV lithography," Nanotechnology **19**, 145304 (2008). 26

[24] J. M. van den Broek, L. A. Woldering, R. W. Tjerkstra, F. B. Segerink, I. D. Setija, and W. L. Vos, "Inverse-woodpile photonic band gap crystals with a cubic diamond-like structure made from single-crystalline silicon," Adv. Func. Mat. **22**, 25 (2012). 26, 49

[25] D. A. Grishina, C. A. M. Harteveld, L. A. Woldering, and W. L. Vos, "Method to make a single-step etch mask for 3D monolithic nanostructure," Nanotechnology **26**, 505302 (2015). 26

[26] N. W. Ashcroft and N. D. Mermin, *"Solid state physics,"* (Holt, Rinehart and Winston, New York NY, 1976). 26, 36, 38, 40

[27] H. H. Li, "Refractive index of silicon and germanium and its wavelength and

temperature derivatives," J. Phys. Chem. Ref. Data **9**, 561 (1993). 26

[28] From scanning electron microscopy the lattice parameter was found to be $a = 693 \pm 10$ plus the error margin of the SEM that amounts to 2% to 3%.[24] Therefore, we take $a = 677$ nm, which shows the best match of the central frequencies in the calculations and in the experiments, see Fig. 2.8. Moreover, for $a = 677$ nm, experimental stop bands agree best with the calculated photonic band gap, see Fig. 2.8. 26

[29] S. G. Johnson and J. D. Joannopoulos, "Block-iterative frequency-domain methods for Maxwell's equations in a planewave basis," Opt. Express **8**, 3 (2001). 26

[30] Throughout this chapter, we express frequency as a reduced frequency $\tilde{\omega} = \omega a/(2\pi c')$), with ω the frequency, a the lattice parameter, c' the speed of light that is not to be confused with the lattice parameter c. In this definition, the reduced frequency $\tilde{\omega}$ is expressed in units of (a/λ). 27, 28

[31] "COMSOL Multiphysics® v. 5.2. www.comsol.com, COMSOL AB, Stockholm, Sweden". 27

[32] J.M. Jin, *"The finite element method in electromagnetics,"* (Wiley-IEEE Press, New York, 2000). 27

[33] A. Yariv and P. Yeh, *"Optical waves in crystals: propagation and control of laser radiation,"* (Wiley, New York NY, 1980), Chapter 6, pp. 155-219. 31, 37, 38, 39, 40, 42

[34] Y. Shen, D. Ye, I. Celanovic, S. G. Johnson, J. D. Joannopoulos, and M. Solijačić, "Optical broadband angular selectivity," Science **343**, 6178 (2014). 32

[35] J. G. Fleming, S. -Y. Lin, I. El-Kady, R. Biswas, and K. M. Ho, "All-metallic three-dimensional photonic crystals with a large infrared bandgap," Nature (London) **417**, 52 (2002). 34

[36] S. E. Han, A. Stein, and D. J. Norris, "Tailoring self-assembled metallic photonic crystals for modified thermal emission," Phys. Rev. Lett. **99**, 053906 (2007). 34

[37] W. L. Vos and H. M. van Driel, "Higher order Bragg diffraction by strongly photonic fcc crystals: onset of a photonic bandgap," Phys. Lett. A **272**, 101 (2000). 34

[38] For s-polarization, the calculated central frequency is $6374 \pm 25\ cm^{-1}$, while the measured central frequency was reported to be $6355 \pm 32\ cm^{-1}$ in the ΓX direction and $6288 \pm 32\ cm^{-1}$ in the ΓZ direction. For p-polarization, the calculated central frequency is $6436 \pm 51\ cm^{-1}$, while the measured central frequency was reported to be $6500 \pm 32\ cm^{-1}$ in the ΓX direction and $6285 \pm 32\ cm^{-1}$ in the ΓZ direction. 36

[39] For s-polarization, the calculated band width is $1433 \pm 25\ cm^{-1}$ (namely from $5657\ cm^{-1}$ to $7090\ cm^{-1}$), while the measured band width was reported to be $1410 \pm 32\ cm^{-1}$ (namely from $5650\ cm^{-1}$ to $7060\ cm^{-1}$) in the ΓX direction and $1325 \pm 32\ cm^{-1}$ (namely from $5625\ cm^{-1}$ to $6950\ cm^{-1}$) in the ΓZ direction. 36

[40] For p-polarization, the calculated band width is $1190 \pm 51\ cm^{-1}$ (namely from $5841\ cm^{-1}$ to $7031\ cm^{-1}$), while the measured band width was reported

to be 1150 ± 32 cm^{-1} (namely from 5925 cm^{-1} to 7075 cm^{-1}) in the ΓX direction and 730 ± 32 cm^{-1} (namely from 5920 cm^{-1} to 6650 cm^{-1}) in the ΓZ direction. 36

[41] E. Yeganegi, A. Lagendijk, A. P. Mosk, and W. L. Vos, "Local density of optical states in the band gap of a finite one-dimensional photonic crystal," Phys. Rev. B **89**, 045123 (2014). 37, 38

[42] C. Tserkezis, "Effective parameters for periodic photonic structures of resonant elements," J. Phys.: Condens. Matter **21**, 155404 (2009). 37

[43] Yu. A. Vlasov, V. N. Astratov, O. Z. Karimov, A. A. Kaplyanskii, V. N. Bogomolov, and A. V. Prokofiev , "Existence of a photonic pseudogap for visible light in synthetic opals," Phys. Rev. B. **55**, 13357 (1997). 37

[44] J. F. Bertone, P. Jiang, K. S. Hwang, D. M. Mittleman, and V. L. Colvin, "Thickness dependence of the optical properties of ordered silica-air and air-polymer photonic crystals," Phys. Rev. Lett. **83**, 300 (1999). 37

[45] N. Stefanou, C. Tserkezis, and G. Gantzounis, "Plasmonic excitations in ordered assemblies of metallic nanoshells," Proc. of SPIE **6989**, 698910 (2008). 37

[46] W. L. Vos and L. A. Woldering, in Ref. 49 Chapter 8, pp. 180-214, also available from: http://arxiv.org/abs/1504.06803. 38

[47] W. L. Vos, H. M. van Driel, M. Megens, A. F. Koenderink, and A. Imhof, "Experimental probes of the optical properties of photonic crystals," Proceedings of the NATO ASI "Photonic Crystals and Light Localization in the 21st century," edited by C.M. Soukoulis (Kluwer, Dordrecht, 2001), 181- 198 (2001). 38

[48] W. L. Vos, R. Sprik, A. van Blaaderen, A. Imhof, A. Lagendijk, and G. H. Wegdam, "Strong effects of photonic band structures on the diffraction of colloidal crystals," Phys. Rev. B **53**, 24 (1996). 38

[49] Edited by M. Ghulinyan and L. Pavesi, *"Light Localisation and Lasing: Random and Pseudorandom Photonic Structures,"* (Cambridge Univ. Press, Cambridge, 2015). 50

[50] H. M. van Driel and W. L. Vos, "Multiple Bragg wave coupling in photonic band gap crystals," Phys. Rev. B **62**, 9872-9875 (2000). 38

[51] M. A. Green, K. Emery, Y. Hishikawa, W. Warta, and E. D. Dunlop, "Solar cell efficiency tables (Version 45)," Prog. Photovolt. **20**, 606 (2012). 41

[52] A. Polman and H. A. Atwater, "Photonic design principles for ultrahigh-efficiency photovoltaics," Nat. Mater. **11**, 174-177 (2012). 41

[53] P. Bermel, C. Luo, L. Zeng, L. C. Kimerling, and J. D. Joannopoulos, "Improving thin-film crystalline silicon solar cell efficiencies with photonic crystals," Opt. Express **15**, 25 (2007). 42

[54] D. J. Griffiths, *"Introduction to electrodynamics,"* (Prentice Hall, Upper Saddle River NJ, 1999). 43

[55] A. Ghatak and K. Thyagarajan, *"Optical Electronics,"* (Cambridge University Press, Cambridge, 1999). 44

CHAPTER 3

Broadband, omnidirectional, and polarization-insensitive back reflector for thin silicon film solar cells

3.1 Introduction

The sun is the ultimate source of energy bestowed upon nature and humankind. A major key to harness the sun's energy is a solar cell, which employs the photovoltaic effect to convert light into electricity using semiconducting materials [1]. Being the most abundant and non-toxic semiconducting material available in the earth's crust, silicon is an ideal choice to make a solar cell [2]. The cost of a silicon solar cell largely depends on the volume of material used. Therefore, thin-film silicon solar cells are favorable over thick-film silicon solar cells due to cost reduction. Also, thin-film silicon solar cells are lightweight, flexible and versatile for building-integrated photovoltaics and for photovoltaic gazing material to laminate windows.

However, these solar cells are too thin for the silicon material to effectively absorb the incident light in the high photon energy region of the solar spectrum [3–5], adversely affecting the cost and the flexibility advantages. Crystalline silicon (c-Si) has a band gap at 1.1 eV that causes the absorption of light in the near infrared regime to be low, as illustrated by a long absorption length of $l_a = 1$ mm at $\lambda = 1100$ nm and $l_a = 10\mu$m at $\lambda = 800$ nm [6]. This wavelength range contains upto 36% of all solar photons [7] and hence thin film c-Si solar cells will fail to capture a significant fraction of solar energy. Therefore, limited light absorption constrains the efficiency of thin-film silicon solar cells [3, 8–11].

Efficient light trapping [5, 10] can enhance the photovoltaic efficiency of silicon solar cells while sustaining the advantages of the thin film. The traditional light trapping approach controls the light paths in the solar cells using geometrical optics [12, 13], *e.g.*, by scattering incident light via surface texturing and using a back reflector that reflects unabsorbed light back into the solar cell. In practice, perfect scattering is impossible to achieve, which limits the attainable efficiency [14]. An ideal back reflector reflects light incident from any angle, known as omnidirectional reflectance, and ideally for all wavelengths, and all polarizations of light. Theoretically, a perfect superconducting metal gives 100% reflectivity for all wavelengths and all polarizations and could thus be considered an ideal back reflector. In practice, no metal has 100% reflectivity at all wave-
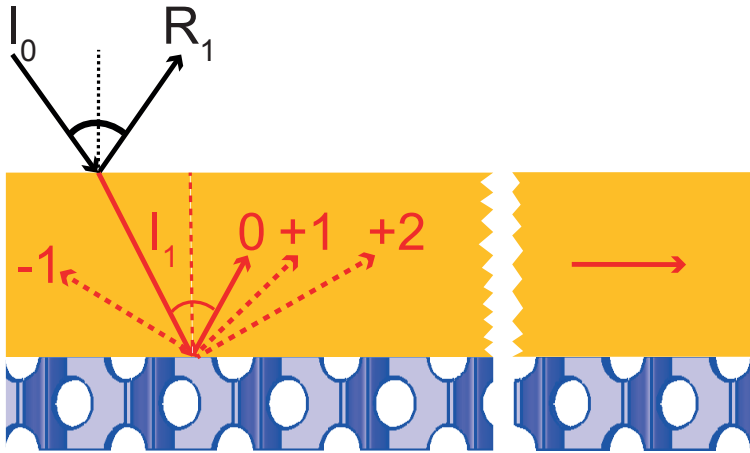
Figure 3.1: Schematic illustration of a solar cell design consisting of a thin silicon film (orange) with a 3D photonic band gap crystal (purple) as back reflector. Here, I_0 and R_1 represent the light incident and reflected at the front surface of the thin silicon film. I_1 represents the light refracted into the thin silicon film medium and incident on the photonic crystal. 0 corresponds to the 0th diffraction order that corresponds to specular reflected light by the photonic crystal; -1, 1, and 2 are nonzero diffraction orders. The red arrow on the right represents the propagation of guided resonant modes in the thin silicon film.

lengths due to Ohmic losses [15]. The unreflected light gets absorbed in the metal and produces heat, which limits the photovoltaic efficiency of the solar cell.

Recently, it has been shown that the light trapping approaches based on wave optics [16–18] outperform all geometrical optics approaches for a certain range of frequencies. One can employ specially nano-designed structures such as photonic crystals [19–25], notably crystals with a complete 3D photonic band gap, a frequency range for which the propagation of light is rigorously forbidden for all incident angles and all polarizations. Therefore, a 3D photonic band gap crystal is theoretically an omnidirectional, broadband, and polarization-insensitive back reflector for solar cells.

Figure 3.1 shows a schematic illustration of a thin silicon film (orange) with a 3D photonic band gap crystal as a back reflector (blue). Incident light has intensity I_0 and once it is in the thin film, it has intensity I_1. When the light I_1 has a frequency in the band gap, it is reflected by the photonic crystal [26]. The reflected beam corresponds to the zeroth diffraction order. Figure 3.1 illustrates non-zeroth order diffraction modes at certain discrete wavelengths, $e.g.$, -1, 1, and 2 generated at the thin film-photonic crystal interface. These non-zero diffraction modes couple into guided resonant modes and are confined inside the thin film via total internal reflection. Hence, a 3D photonic crystal will enhance the absorption of a thin silicon film for all incident angles and polarizations by (i) giving perfect reflectivity inside the band gap and (ii) generating guided resonances at certain discrete wavelengths. Recently, a numerical study was reported

on the reflectivity for a realistic 3D silicon photonic band gap crystal with finite support [27]. However, this study employed a constant, non-absorbing refractive index of the silicon, which can thus not capture photovoltaic behavior.

We study here a 3D photonic band gap crystal [28–30] with finite support as a back reflector in the visible regime. We use finite-element computations of the 3D time-harmonic Maxwell equations to calculate absorption of light in a thin-film silicon solar cell with a photonic crystal as a back reflector. The high-index backbone of the inverse woodpile photonic crystal has a refractive index similar to silicon. To make our calculations relevant to experimental studies, we consider a dispersive (wavelength-dependent) complex refractive index obtained from experiments [31]. We tailor the inverse woodpile crystal design to have a broad photonic band gap in the visible range to improve the photovoltaic efficiency of thin-film silicon. We compare the photonic crystal back reflector to a perfect metallic back reflector. We also assess the absorption enhancement without the additional length of a back reflector. We investigate the absorbing layer with thicknesses varying from sub-wavelength to multiple-wavelength. As a result, our numerical study shows nearly 2.6 times enhanced frequency-, angle-, polarization-averaged absorption between $\lambda = 680$ nm and $\lambda = 890$ nm compared to a thin silicon film only. We emphasize on understanding the physics behind such a large enhancement by identifying the responsible physical mechanism beyond a standard back reflector.

3.2 Methods

The solar cell design in Fig. 3.1 consists of a thin silicon film as an absorbing layer and a cubic inverse woodpile photonic crystal as a back reflector. The 3D inverse woodpile crystal structure consists of two 2D arrays of identical pores with radius r running in two orthogonal directions X and Z [28]. Each 2D array has a centered-rectangular lattice with lattice parameters c and a. When the lattice parameters have a ratio $\frac{a}{c} = \sqrt{2}$, the diamondlike structure is cubic. Cubic inverse woodpile photonic crystals have a broad maximum band gap width $\Delta\omega/\omega_c = 25.3\%$ relative to the central band gap frequency ω_c for pores with a relative radius $\frac{r}{a} = 0.245$ [29, 30]. Our results in Ref. 27 and Chapter 2 reveal that a reflectivity in excess of $R > 99\%$ (hence transmission $T < 1\%$) occurs even for a thin inverse woodpile photonic crystal with a thickness $L \geq 3c$. Therefore, we choose a cubic inverse-woodpile crystal with an optimal pore radius $\frac{r}{a} = 0.245$ and with a thickness $L_{3DPC} = 4c$ as a back reflector for the calculation of the absorption of light by the solar cell.

To accurately model the optical absorption of a thin silicon film solar cell, we employ the commercial COMSOL finite-element (FEM) solver to describe the time-harmonic Maxwell equations [32]. Figure 3.2 illustrates the computational cell viewed in the YZ plane. We employ Bloch-Floquet periodic boundaries in the $\pm X$ and the $\pm Y$ directions to describe a thin film [26]. To mimic a solar cell with finite support, absorbing boundaries are employed in the $-Z$ and $+Z$ directions. The incident fields start from a plane at the left that is separated
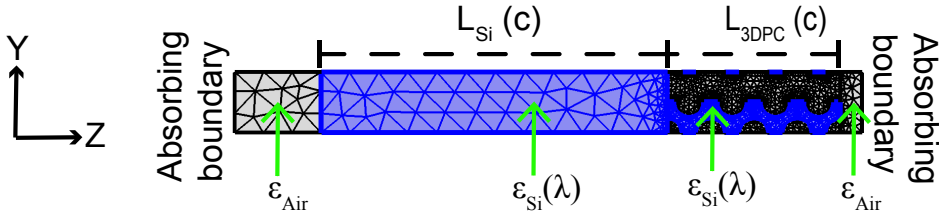
Figure 3.2: Computational cell for the thin silicon film solar cell with a photonic crystal back reflector. A thin silicon film with thickness $L_{Si} = 8c$ is the absorbing layer. A 3D inverse woodpile photonic crystal with a thickness $L_{3DPC} = 4c$ acts as a back reflector. The computational cell is bounded by absorbing boundaries at $-Z$ and $+Z$, and by periodic boundary conditions at $\pm X$ and $\pm Y$. The blue color represents the high-index material with a dielectric function similar to silicon.

from the silicon layer by an air layer. The plane represents a boundary condition rather than a true current source since it also absorbs the reflected waves [33]. The incident plane waves have either s polarization (electric field normal to the plane of incidence) or p polarization (magnetic field normal to the plane of incidence), and have an angle of incidence between $0°$ and $80°$. We calculate reflectivity and transmission of the solar cell at the absorbing boundaries in the $-Z$ and $+Z$ directions, respectively. The light with a given wavelength λ incident at an angle θ is either reflected or transmitted, or absorbed by the thin film solar cell [15]. Thus, we calculate the absorption $A(\lambda, \theta)$ for the solar cell as

$$A(\lambda, \theta) = I_0 - R(\lambda, \theta) - T(\lambda, \theta), \qquad (3.1)$$

with I_0 the incident light, $R(\lambda, \theta)$ the reflectivity, and $T(\lambda, \theta)$ the transmission.

Figure 3.2 illustrates the finite element mesh that is used to subdivide the 3D computational cell into elements. We use tetrahedra as basic elements in our finite element method. Since the air layer and the silicon thin film are homogeneous media, an upper limit $\triangle l \leq \frac{\lambda_0}{8}$ is imposed to the edge length Δl on any tetrahedron in these layers, with λ_0 the shortest wavelength of the incident plane waves in vacuum. An inverse woodpile crystal contains many sharp interfaces between the high-index backbone and the air. To accurately mesh this complex geometry, an upper limit $\Delta l \leq \frac{\lambda_0}{8 \max(n_{Si})}$ is imposed to the edge length Δl on any tetrahedron in the inverse woodpile photonic crystal, with $\max(n_{Si})$ the maximum refractive index for the selected range of wavelengths. For computational efficiency, we apply the MUMPS direct solver that is fast, multicore capable, and cluster capable. We perform calculations on the "Serendipity" cluster [34] at MACS in MESA+.

To make our calculations relevant to experimental studies, we used a wavelength-dependent complex refractive index obtained from experiments for the thin silicon film and the high-index backbone of the inverse woodpile photonic crystal. Figure 3.3 shows the wavelength dependency of the real and imaginary parts of
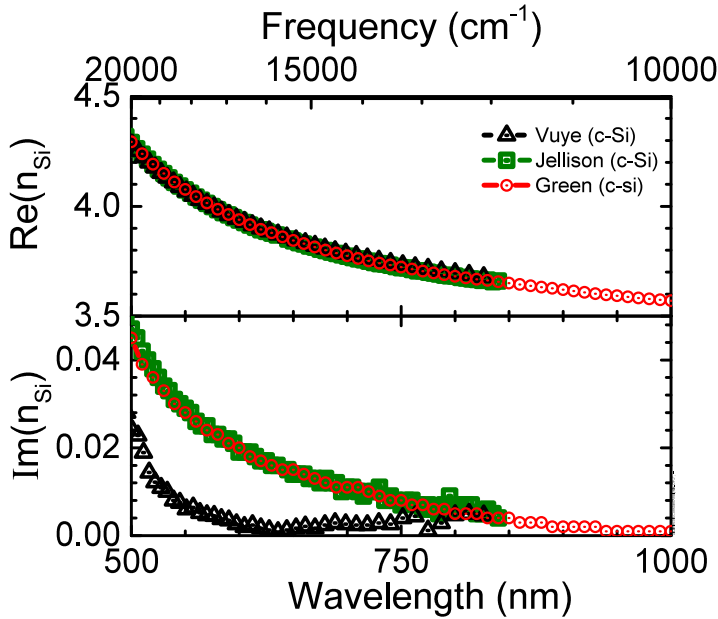
Figure 3.3: Wavelength dependence of real and imaginary parts of the refractive index of silicon in the visible regime. Red circles, Black triangles, and green squares are the data obtained from Ref. 31, Ref. 35, and Ref. 36, respectively. The top ordinate shows the frequency in wave numbers (cm^{-1}).

the refractive index of silicon in the visible regime from several sources of measurements. Ref. 35 presents the dielectric function of a commercially available silicon wafer using *in situ* spectroscopic ellipsometry. In Ref. 36 the dielectric function of crystalline silicon is measured using two-channel polarization modulation ellipsometry, whereas Ref. 31 gives a tabulation of the optical properties of intrinsic silicon based on many different sources, aiming at solar cell calculations. Figure 3.3 shows that for the real part of the refractive index the data of Ref. 35, Ref. 36, and Ref. 31 are in very good mutual agreement. For the imaginary part of the refractive index, we observe that the results of Ref. 36 and Ref. 31 agree well with each other between 500 nm and 750 nm and differ from the ones from Ref. 35 for reasons unknown to us. Since Ref. 31 is based on many different sources of data, we have decided to adopt it as the source of the refractive index of silicon in our study.

To enhance the weak absorption of silicon in the frequency range above the electronic band gap (corresponding to wavelengths in the range 600 nm $< \lambda <$ 1100 nm), we tailor the lattice parameter of the inverse woodpile photonic crystal to be $a = 425$ nm (and hence $c = 300$ nm), such that the band gap is in the visible range. This choice for the lattice parameter is significantly smaller than usually taken for photonic band gap physics at frequencies in the non-absorbing range [37, 38](Chapter 2). Throughout this chapter, we express all thicknesses

in terms of the lattice parameter $c = 300$ nm.

A perfect metal is known to posses a very large imaginary value for the refractive index and hence gives 100% reflectivity for all wavelengths and for all polarizations [15]. Therefore, a perfect metal is considered as an ideal back reflector for a thin silicon film. In order to evaluate our proposition of using a 3D inverse woodpile photonic crystal as a back reflector, we compare the absorption spectra for a thin silicon film with a photonic crystal back reflector to spectra for a thin film with a perfect metallic back reflector. To calculate the absorption spectra of a thin silicon film with a perfect metallic back reflector, we replace the photonic crystal and the air layer on the right in Fig. 3.2 with a homogeneous metallic plane. We use a very large purely imaginary refractive index for the perfect metallic plane $n'' = -i \cdot 10^{20}$.

3.3 Results

3.3.1 Wavelength-resolved transmission and absorption

For the thin silicon film with a photonic crystal back reflector, we decided to break the problem down into several steps, in order to allow the physical interpretation of the problem at hand. First, we perform simulations of the thin film with a photonic crystal back reflector where we only consider a zero imaginary part of the refractive index ($\mathbb{Im}(n_{Si}) = 0$), hence we only allow dispersion but no imaginary part of the refractive index. This fictitious situation was chosen since it allows to build on the absorption-free results in Chapter 2. In a second step, we consider the same solar cell structure with the full dispersive and absorbing refractive index of silicon that was modeled according to Ref. 31.

We have performed an extensive set of polarization-resolved (s or p) transmission and absorption calculations at normal incidence to the thin silicon film. The transmission spectra for the thin silicon film in Fig. 3.4 reveal oscillations between $\lambda = 600$ nm and $\lambda = 1450$ nm for both polarizations. We observe that these oscillations diminish in amplitude with decreasing wavelength. The intensity of a propagating wave decays exponentially due to the imaginary part of the refractive index of the medium of propagation [39]. We note that the imaginary part of the refractive index of silicon in Fig. 3.3 increases with decreasing wavelength. Therefore, the incident wave strongly decays through a thin silicon film with decreasing wavelength and hence these oscillations diminish in amplitude. These oscillations are possibly the signature of Fabry-Pérot fringes [40] resulting from multiple Bragg diffractions of the propagating incident wave at the two interfaces of the thin film.

To verify whether the oscillations are indeed Fabry-Pérot fringes, we compare the diffraction order of the fringes in the transmission spectra to the diffraction order obtained from the Fabry-Pérot interference condition. From the Fabry-Pérot interference condition corresponding to standing waves in the thin film [40], the diffraction order Δm in terms of the central frequency ν_c of a fringe is

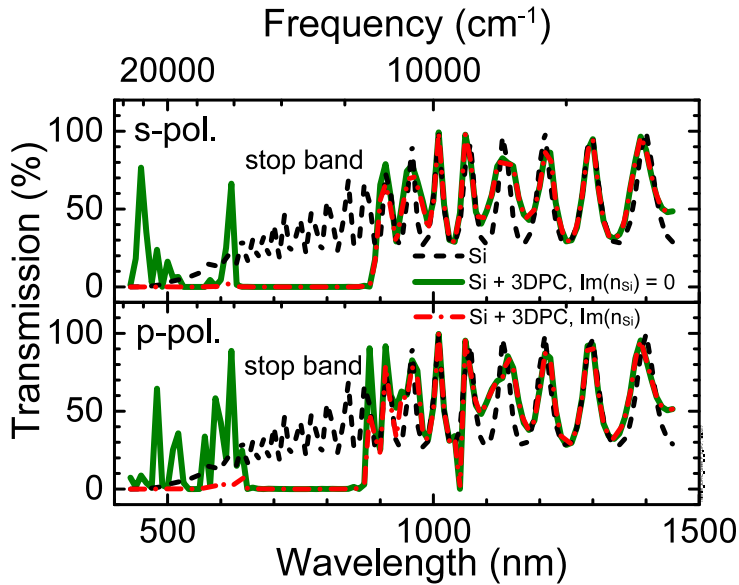$$\Delta m = 2L_{Si}\nu_c n_{Si}(\nu_c), \tag{3.2}$$

Figure 3.4: Transmission spectra calculated for a thin silicon film solar cell at normal incidence. Top panel: s polarization, bottom panel: p polarization. Black dashed curves are the transmission spectra for a thin silicon film. Green solid curves are results for the thin silicon film with a 3D inverse woodpile photonic crystal back reflector, with dispersion but no absorption in silicon ($\mathbb{Im}(n_{Si}) = 0$). Red dashed-dotted curves are results for the thin silicon film with a 3D inverse woodpile photonic crystal back reflector, including absorption ($\mathbb{Im}(n_{Si}) \neq 0$).

with L_{Si} the thickess of the silicon film and $n_{Si}(\nu_c)$ the dispersive refractive index of silicon. We describe analytically the diffraction orders Δm from Eq. 3.2 for the central frequency ν_c of a fringe for the thin silicon film (thickness $L_{Si} = 8c$) in Fig. 3.4 and the refractive index of silicon at ν_c from Ref. 31. Figure 3.5 shows an agreement within 0.3% between the analytically and the numerically calculated diffraction orders. Therefore, the oscillations revealed in the transmission spectra of the thin silicon film in Fig. 3.4 are indeed Fabry-Pérot fringes. We note from Eq. 3.2 that there exists a linear relation between the transmission spectra and the absorption spectra. Therefore, Fabry-Pérot fringes will also appear in the absorption spectra corresponding to the central frequencies of fringes in the transmission spectra as we will see later on.

Figure 3.4 shows that the transmission between $\lambda = 600$ nm and $\lambda = 1500$ nm is nearly the same for a thin film with a photonic crystal back reflector with and without imaginary part of the silicon refractive index. We note nearly 0% transmission between $\lambda = 600$ nm and $\lambda = 900$ nm. These strong transmission troughs indicate an $s-$polarized stop band from $\lambda = 647$ nm to $\lambda = 874$ nm and a $p-$polarized stop band from $\lambda = 634$ nm to $\lambda = 892$ nm. From the good agreement of the stop bands with and without absorption in silicon, we deduce
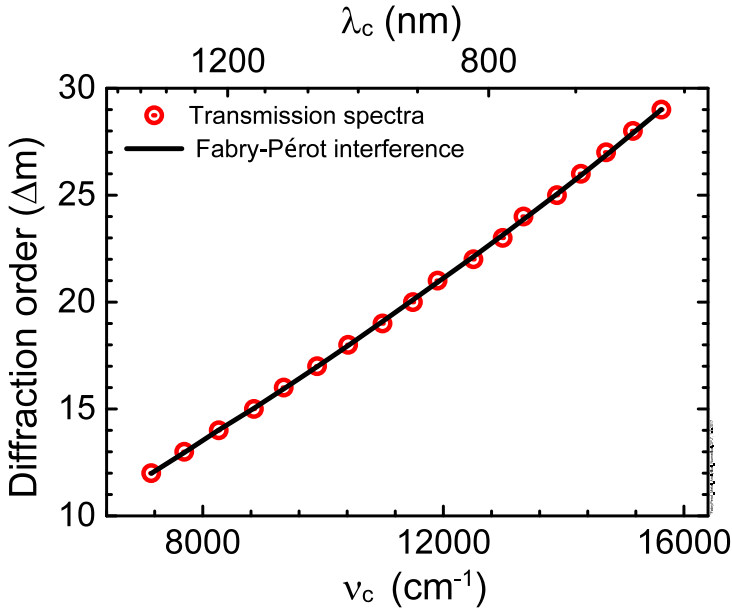
Figure 3.5: Diffraction order versus the central frequency of the fringes in the transmission spectra of the thin silicon film in Fig. 3.4. Red circles are the diffraction order of the fringes taken directly from the transmission spectra. The black line represents the analytical diffraction order calculated from Eq. 3.2 using the dispersive refractive index of silicon in Ref. 31.

that an inverse woodpile photonic crystal behaves as a perfect reflector in the visible range even with full absorption. This also shows that the absorption length of silicon is longer than the Bragg attenuation length inside the stop bands of the 3D inverse woodpile photonic crystal. Hence, the waves incident on the photonic crystal are reflected back before being absorbed by the high-index backbone of the photonic crystal. Therefore, the Fabry-Pérot fringes revealed between $\lambda = 600$ nm and $\lambda = 1450$ for a thin silicon film are suppressed by the stop bands of the photonic crystal back reflector. The transmission spectra for the thin film with a photonic crystal back reflector reveals oscillations above $\lambda = 900$ nm for both polarizations. These oscillations have nearly the same central frequencies and bandwidths as the Fabry-Pérot fringes revealed for thin silicon film. Therefore, we conclude that these oscillations are indeed the Fabry-Pérot fringes. We observe oscillations below $\lambda = 600$ nm in the transmission spectra for a thin silicon film with a photonic crystal back reflector with zero imaginary part for the silicon refractive index. The transmission spectra with a physically realistic imaginary refractive index show nearly 0% transmission below $\lambda = 600$ nm. Since silicon is strongly absorbing at wavelengths below $\lambda = 600$ nm, no light remains unabsorbed and hence there are no more fringes.

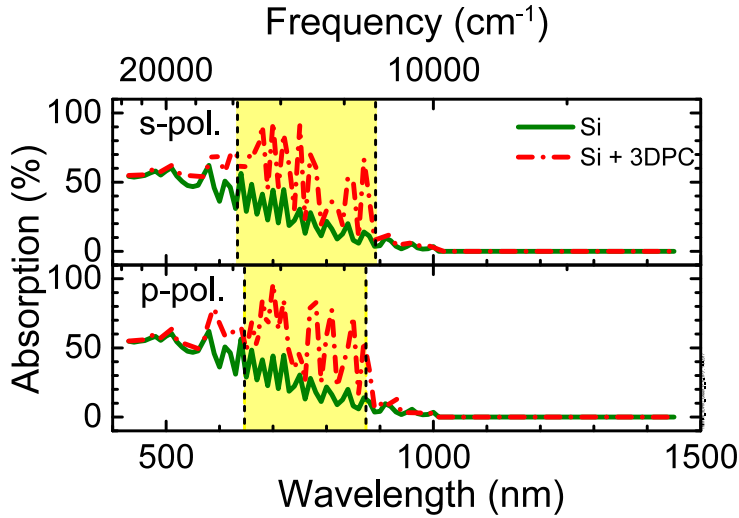Figure 3.6 shows the absorption spectra for a thin silicon film without and with

Figure 3.6: Absorption spectra calculated for a thin silicon film solar cell at normal incidence. Top panel: s polarization, bottom panel: p polarization. Green solid curves are results for a thin silicon film. Red dashed-dotted curves are results for a thin silicon film with a 3D inverse woodpile photonic crystal back reflector. The vertical black dashed lines indicate the edges of the $s-$stop band in the top panel and $p-$stop band in the bottom panel. The stop bandwidths are shown with the yellow bar. These stop bands are obtained from the transmission spectra in Fig. 3.4.

a 3D inverse woodpile photonic crystal back reflector. We consider the dispersive and complex refractive index for the silicon film and the high-index backbone of the photonic crystal. We observe that the absorption for thin film is nearly 0% above $\lambda = 900$ nm. This shows that silicon has negligible absorption in the near infrared regime where the imaginary part of the silicon refractive index is very small ($\mathbb{Im}(n_{Si}) \sim 0$ as shown in Fig. 3.3). Fabry-Pérot fringes are revealed below $\lambda = 900$ nm, corresponding to standing waves in the thin silicon film. With decreasing wavelength, the imaginary part of the silicon refractive index increases (as shown in Fig. 3.3) and hence the absorption in silicon increases in Fig. 3.6.

After understanding the absorption spectra of the thin silicon film, we now study the absorption spectra of a thin film with a photonic crystal back reflector, see Figure 3.6. We observe that above $\lambda = 900$ nm, the absorption spectra for both polarizations match with the corresponding absorption spectra for the thin film only. Between $\lambda = 600$ nm and $\lambda = 900$ nm, the absorption spectra for a thin film with a photonic crystal back reflector differ considerably from the absorption spectra for a thin film without back reflector. We observe enhancements and oscillations between $\lambda = 600$ nm and $\lambda = 900$ nm in the absorption spectra of the thin film with a photonic crystal back reflector for both polarizations, which differs from the spectra for the thin film only.

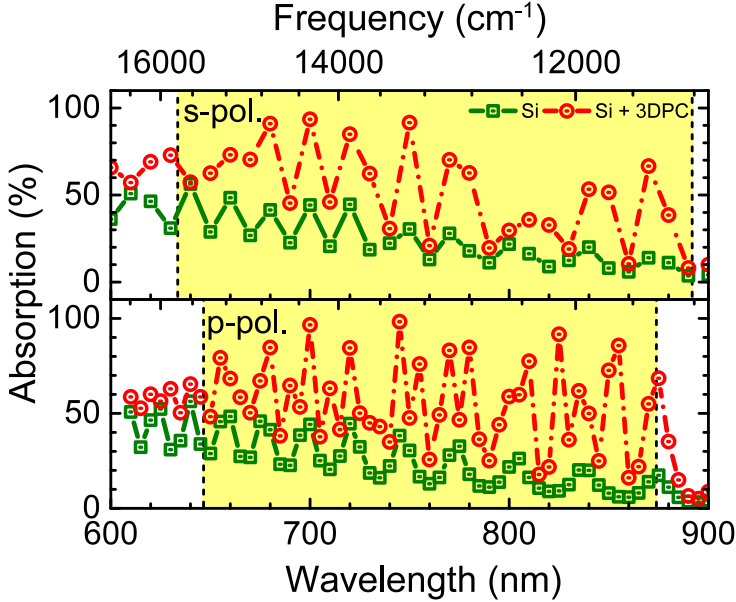In order to characterize this difference, we zoom in on the absorption inside

Figure 3.7: Absorption in the stop band of a 3D inverse woodpile photonic crystal. Top panel: $s-$, bottom panel: $p-$polarized light. Green solid curves are absorption spectra for a thin silicon film. Red dashed-dotted curves are absorption spectra for a thin silicon film with a 3D inverse woodpile photonic crystal back reflector. The vertical black dashed lines indicate the edges of the $s-$stop band in the top panel and $p-$stop band in the bottom panel. The stop bandwidths are shown as the yellow bar.

the stop bands between $\lambda = 600$ nm and $\lambda = 900$ nm in Fig. 3.7. We note that in the $s-$stop band in the top panel the fringes for a thin film with photonic crystal back reflector are enhanced in amplitude compared to the fringes for a standalone thin film.

In the bottom panel of Fig. 3.7, we show the absorption spectra for p polarization at higher resolution in wavelength. We observe that the fringes inside the $p-$stop band are clearly increased in number compared to the thin film only. We will try to interpret this result by first considering diffraction from the photonic crystal surface.

In Ref. 37, 38 and Chapter 2, the light is incident on the photonic crystal surface from air. In contrast, the solar cell design in Fig. 3.1 shows that the light first resides in a silicon medium, before it is incident on the photonic crystal surface. Therefore, the wavelength λ of the incident light reduces to $\lambda/n_{Si}(\lambda)$ inside the silicon layer. Firstly, for the entire stop bands (both s and p) the wavelength $\lambda/n_{Si}(\lambda)$ between $\lambda = 600$ nm and $\lambda = 900$ nm is considerably smaller than the lattice parameter $c = 300$ nm of the 3D inverse woodpile photonic crystal along the ΓZ direction in wave vector space. Secondly, a 3D inverse woodpile photonic crystal introduces a periodic refractive index contrast at the interface with a thin silicon film. Due to these two reasons, nonzero diffraction modes [25, 26] are

generated from the photonic crystal-thin film interface at specific wavelengths inside the stop bands, giving rise to a finite number of additional reflected waves.

The silicon film thickness $L_{Si} = 8c$ is larger than half of the wavelength $\lambda/n_{Si}(\lambda)$ inside the absorbing layer for the stop bands between $\lambda = 600$ nm and $\lambda = 900$ nm. This satisfies the condition for a photonic crystal-thin film interface to couple the reflected waves into the guided resonant modes [15, 22] that propagate inside the film and are confined within the film via total internal reflection. The absorption on guided resonant modes can be very high [22], sometimes approaching values as large as 100%, *e.g.*, at $\lambda = 700$ nm and 720 nm in the bottom panel of Fig. 3.7. Therefore, the physical mechanism responsible for the additional number of fringes is non-zero diffraction modes coupled into guided resonant modes due to the photonic crystal back reflector. We note that the perfect reflectivity of a 3D inverse woodpile photonic crystal extends over the entire stop bands, whereas nonzero order diffraction modes and guided resonant modes are limited to certain specific wavelengths. Later on in Section 3.3.7, we investigate this topic further by decreasing the thickness of the film, such that no guided resonant modes are allowed.

3.3.2 Comparison to a perfect metal

The top panel of Fig. 3.8 shows the comparison between the numerically and the analytically calculated absorption spectra for a thin silicon film, also see Appendix 3.B. The Fabry-Pérot fringes revealed in the top panel in the absorption spectra of the thin film decay in amplitude with increasing wavelength, which is in agreement with the observation made in Section 3.3.1.

Theoretically, a perfect metallic back reflector [15] is considered as an ideal back reflector for a thin film solar cell for all wavelengths and for all polarizations. Therefore, we compare the photonic crystal back reflector to an ideal back reflector. The middle panel of Fig. 3.8 shows the absorption spectra for a thin film with a perfect metallic back reflector, calculated using the method described in Section 3.2. Fabry-Pérot fringes are revealed in the middle panel. The Fabry-Pérot fringes at $\lambda = 700$ nm, 720 nm, and 750 nm in the top panel are spaced by 20 nm and 30 nm. Similar spaced fringes in the middle panel are at $\lambda = 710$ nm, 730 nm, and 760 nm. We note that the fringes in the middle panel are shifted in wavelength with respect to the fringes in top panel. According to the Fresnel equations [15, 39], when an incident wave in a low-index medium is reflected from a medium with a higher refractive index it gets a phase shift of 180°. A perfect metal has a very high refractive index compared to silicon, whereas a photonic crystal has a lower effective index (as calculated in Section 3.2 of Chapter 2). Therefore, the light reflected from the perfect metallic back reflector gets a phase shift of 180°, and hence the fringes in the middle panel are shifted by half a free spectral range with respect to the fringes in top panel. We also observe that the fringes in the middle panel are enhanced in amplitude compared to the fringes in the top panel. Since a perfect metal reflects all incident light, the distance travelled by the light inside the absorbing silicon layer increases and hence the overall absorption in the thin film increases.
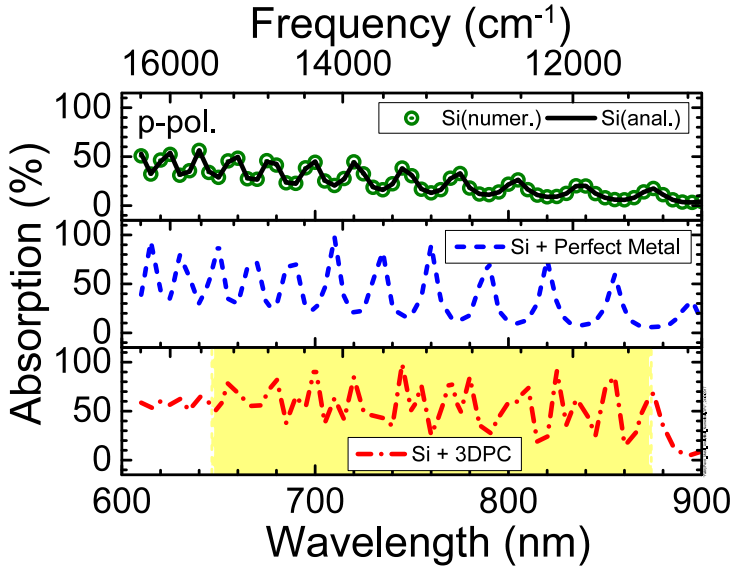
Figure 3.8: Calculated absorption spectra for a thin silicon film solar cell for $p-$polarized light. Top panel: The analytically calculated absorption for a thin silicon film is shown in black solid curve. Blue circles represent the numerically computed absorption for the thin silicon film. Middle panel: Blue dashed curve is the absorption spectrum for a thin silicon film with a perfect metallic back reflector. Bottom panel: Red dashed-dotted curve is the absorption spectrum for a thin silicon film with a 3D inverse woodpile photonic crystal back reflector. The $p-$stop band is shown as the yellow bar.

The bottom panel of Fig. 3.8 shows the absorption spectra for a thin film with a photonic crystal back reflector. The Fabry-Pérot fringes inside the $p-$stop band between $\lambda = 647$ nm and $\lambda = 874$ nm are enhanced in amplitude and numerous compared to the Fabry-Pérot fringes in the top panel, in agreement with the observation made in Section 3.3.1.

For the overall comparison of the fringes revealed in the absorption spectra in all three panels of Fig. 3.8, we calculated the diffraction order for each fringe using the Fabry-Pérot interference condition of Eq. 3.2. Figure 3.9 shows the diffraction order of a fringe in Fig. 3.8 as a function of the central frequency of a fringe and the corresponding refractive index of silicon. We note that between any two diffraction orders for a thin film, there is only one diffraction order of a thin film with a perfect metallic back reflector. The shift in the diffraction orders for a thin film compared to the diffraction orders for a thin film with a perfect metallic back reflector confirms the phase shift of 180° introduced by the perfect metal. Thus, a perfect metal back reflector causes a phase shift in the existing fringe, while the total number of fringes remain constant. Figure 3.9 reveals that there is always more than one diffraction orders of a thin film with a photonic crystal back reflector between two consecutive diffraction orders of a thin film.
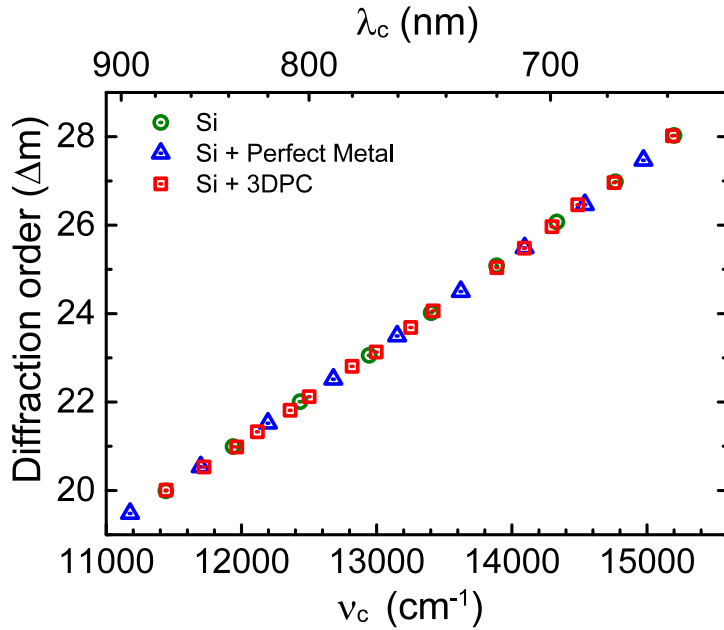
Figure 3.9: Diffraction order versus the central frequency for the Fabry-Pérot fringes revealed in the absorption spectra in Fig. 3.8. Green circles represent fringes for a thin silicon film. Blue triangles represent fringes for a thin silicon film with a perfect metallic back reflector. Red squares represent fringes for a thin silicon film with a 3D inverse woodpile photonic crystal back reflector.

In other words, a photonic crystal back reflector increases the number of fringes for a thin film. We derive from the slope in Fig. 3.9 that the effective refractive index of the silicon remains unchanged by the addition of either a perfect metallic back reflector or a photonic crystal back reflector. Thus, we conclude that the addition of a back reflector increases the effective path length for an absorbing layer and hence enhances the overall absorption, without changing the effective refractive index of the absorbing medium.

3.3.3 Absorption enhancement of a thin silicon film

To quantify a 3D inverse woodpile photonic crystal as a back reflector in the visible regime, we calculate the absorption enhancement η_{abs} of the thin silicon film solar cell shown in Fig 3.2 as

$$\eta_{abs} \equiv \frac{A_{(Si+3DPC)}}{A_{Si}}, \tag{3.3}$$

with $A_{(Si+3PC)}$ the absorption in a thin silicon film with a photonic crystal back reflector and A_{Si} the absorption in a silicon film of thickness equal to the absorbing layer L_{Si} of a solar cell.
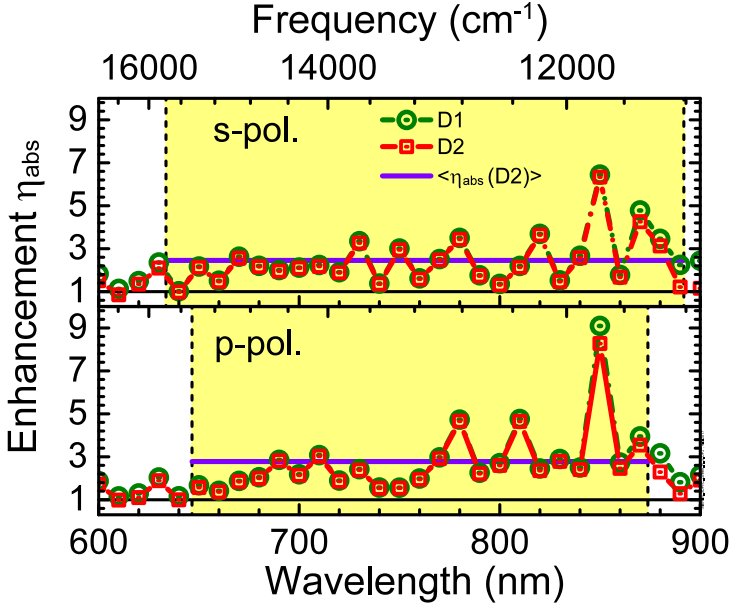
Figure 3.10: Absorption enhancement spectra for a thin silicon film. Top panel: $s-$, bottom panel: $p-$polarized light. D1 indicates the thin silicon film volume and D2 indicates the combined volume of a thin silicon film and a 3D inverse woodpile photonic crystal back reflector. The green solid and the red dashed-dotted curves are enhancement spectra in the D1 and D2 domains, respectively. The vertical black dashed lines indicate the edges of the $s-$stop band in the top panel and the $p-$stop band in the bottom panel. The stop bands are shown as the yellow bar. The violet solid lines denote the frequency-averaged absorption enhancements over the stop band calculated using Eq. 3.4.

Figure 3.10 shows the absorption enhancement η_{abs} for a thin film with a photonic crystal back reflector at the normal incidence for both polarizations. The absorption enhancement oscillates between 1 and 9 inside the stop bands between $\lambda = 640$ nm and $\lambda = 900$ nm. To average the enhancement over a frequency range such as the stop band, we employ the definition

$$< \eta_{abs} > \equiv \frac{\sum_{i=1}^{k} \eta_i \nu_i}{\sum_{i=1}^{k} \nu_i}, \tag{3.4}$$

with k the number of discrete frequencies considered. The frequency-averaged absorption enhancement is nearly $\eta_{abs} = 2.45$ for the $s-$stop band and nearly $\eta_{abs} = 2.78$ for the $p-$stop band.

A perfect back reflector gives 100% specular reflectivity as the 0th order of diffraction. Hence, the absorption enhancement η_{abs} for a thin film with a perfect back reflector is always less than $\eta_{abs} \leq 2$. For specific wavelengths, a photonic crystal back reflector generates non-zero order diffraction modes, which couples light into guided resonant modes and confines the light inside the thin film via

total internal reflection, as discussed in Section 3.3.1. Since the effective optical path length travelled by a non-zero diffraction mode is longer than the one travelled by a zero order diffraction mode, therefore a photonic crystal back reflector gives an absorption enhancement greater than $\eta_{abs} \geq 2$ for specific wavelengths, as observed in Fig. 3.10. This observation strengthens our assertion that a 3D inverse woodpile photonic crystal enhances the absorption of a thin silicon film by (i) behaving as a perfect reflector, exhibiting nearly 100% reflectivity in the stop bands, as well as (ii) generating guided resonant modes at many discrete wavelengths.

Since the high-index backbone of the 3D inverse woodpile photonic crystal is silicon, the addition of a 3D inverse woodpile photonic crystal back reflector effectively increases the total amount of silicon in the solar cell. To investigate whether the absorption is enhanced due to the additional silicon material, we calculated the absorption enhancement within the volume of the absorbing layer L_{Si} of the solar cell (see Fig. 3.2) using the volume integral of the total power dissipation density from Ref. 32. Figure 3.10 shows the comparison between absorption enhancement spectra for the absorbing layer L_{Si} of the solar cell and for the complete solar cell. We observe that the absorption enhancement spectra for the absorbing layer of the solar cell agree very well with the spectra for the complete solar cell in the stop bands between $\lambda = 640$ nm and $\lambda = 900$ nm. Therefore, the absorption in the high-index backbone of a 3D inverse woodpile photonic crystal is negligible inside the stop bands, even in the visible regime. This also shows that the Bragg attenuation length inside the stop bands for a 3D inverse woodpile photonic crystal is indeed smaller than the absorption depth for silicon in the visible regime.

3.3.4 Angle- and wavelength-resolved absorption

As an extension of the transmission and absorption spectra at normal incidence in Sec 3.3.1, we also consider transmission and absorption for angles of incidence up to 80° off normal. Figures 3.11(a) and 3.11(b) show transmission spectra maps for a thin silicon film with a 3D inverse woodpile photonic crystal back reflector. We observe that an angle-independent (omnidirectional) and polarization-independent range of nearly 0% transmission appears between $\lambda = 680$ nm and $\lambda = 880$ nm. We refer to the wavelength range from $\lambda = 680$ nm to $\lambda = 880$ nm as the *omnidirectional stop band* [26]. Therefore, a photonic crystal acts as a perfect reflector in the omnidirectional stop band for all incident angles and for all polarizations, even with full absorption in the refractive index. This shows that the Bragg attenuation length for the 3D inverse woodpile photonic crystal is smaller than the absorption length of silicon for all incident angles for the omnidirectional stop band.

To investigate the effect of the incident angle on the absorption enhancement of a 3D inverse woodpile photonic crystal back reflector in the visible regime, we performed calculations for angles of incidence up to 80° off normal. Figures 3.12(a) and 3.12(b) show the absorption enhancement maps for both polarizations for the omnidirectional stop band obtained from Fig. 3.11(a) and 3.11(b). To
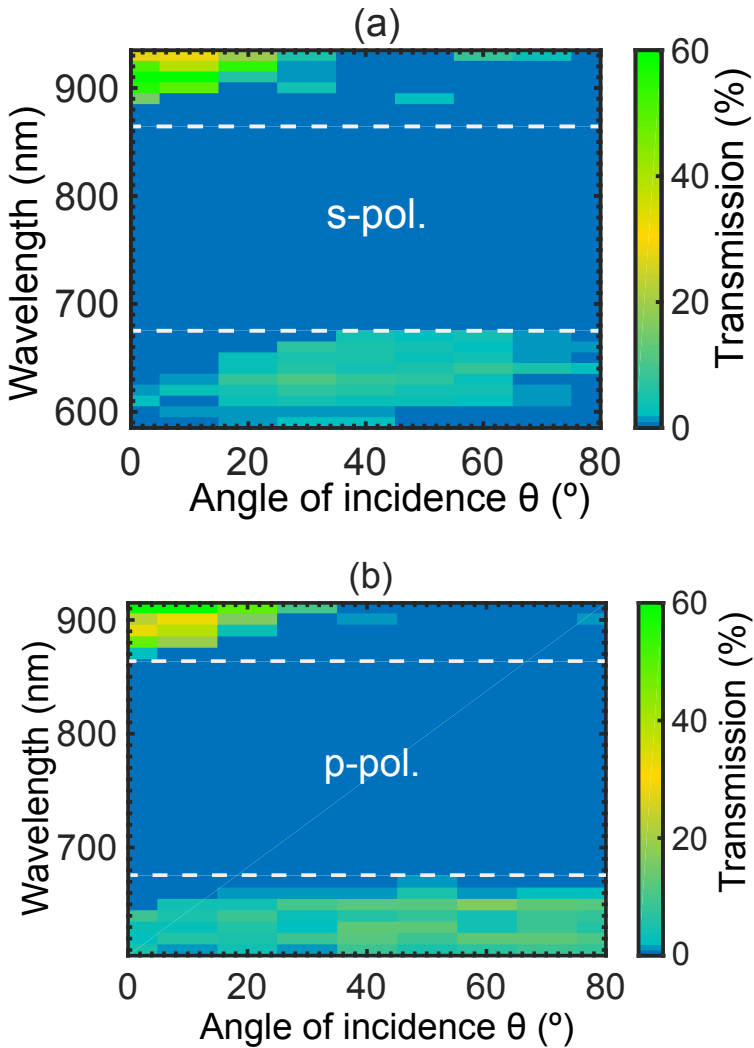
Figure 3.11: Calculated angle- and wavelength-resolved transmission spectra for a thin silicon film solar cell with a 3D inverse woodpile photonic crystal back reflector for (a) *s* polarization and (b) *p* polarization. The dark blue color represents nearly 0% transmission that occurs in the stop band at all incident angles. The white dashed box indicates an angle- and polarization-independent range with nearly 0% transmission.
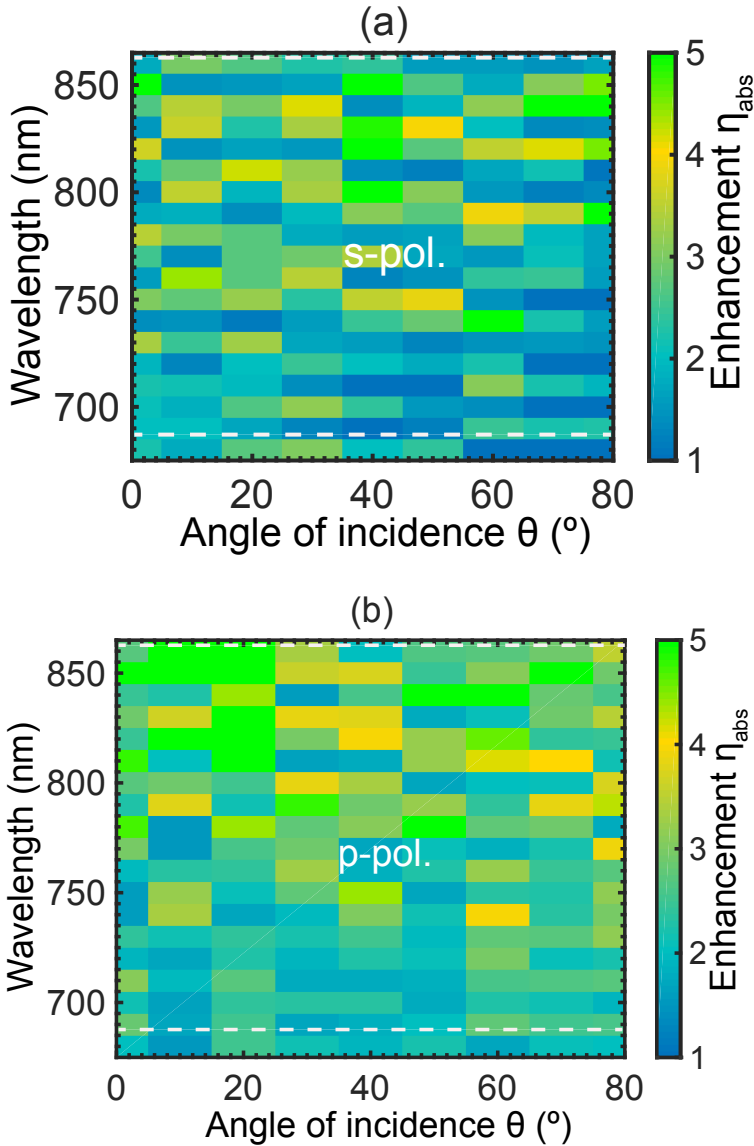
Figure 3.12: Absorption enhancement factor for a thin silicon film solar cell with a 3D inverse woodpile photonic crystal back reflector for (c) $s-$ and (d) $p-$polarized light. The white dashed box indicates the angle- and polarization-independent wavelength range obtained from Fig. 3.11. The dark blue color represents an enhancement ratio less than or equal to 1. Absorption enhancement η'_{abs} is calculated using the Eq. 3.3.

calculate the angle-averaged and frequency-averaged absorption enhancement, we employ the definition

$$< \eta'_{abs} > \equiv \frac{1}{n} \sum_{i=1}^{n} cos(\theta_i) \frac{\sum_{i=1}^{k} \eta_i \nu_i}{\sum_{i=1}^{k} \nu_i}, \tag{3.5}$$

with n the number of incident angles and k the number of frequencies and.

Therefore, the angle- and frequency-averaged absorption enhancement for s polarization is $\eta'_{abs} = 2.38$ and for p polarization is $\eta'_{abs} = 2.87$, which exceeds the maximum absorption enhancement feasible for a perfect reflector. These enhancements are possible only if a photonic crystal back reflector generates non-zeroth order diffraction modes at certain discrete wavelengths for all incident angles. Once these non-zero diffraction modes couple into guided resonant modes and are confined inside the thin film via total internal reflection, the effective optical path length travelled is longer than the one travelled by a zero order diffraction mode. Therefore, a 3D inverse woodpile crystal enhances the absorption of a thin silicon film for all incident angles and polarizations by (i) giving perfect reflectivity inside the omnidirectional stop band and (ii) generating guided resonances for specific wavelengths.

3.3.5 Absorption enhancement without the additional length of a back reflector

At this point in our discussion, one could hypothesize that an additional back reflector increases the total length of a thin silicon film solar cell especially since we propose the back reflector to be a photonic crystal that is made of silicon, just like the thin film. One possible design is that we position a 3D inverse woodpile photonic crystal at the back end of a thin silicon film. This design will keep the length of the solar cell unchanged as well as make the thin film solar cell lighter, given that the 3D inverse woodpile photonic crystal consists of nearly 80% volume fraction of air, as shown in Fig. 1.2 of Chapter 1.

To investigate this design, we break the problem down into three steps, in order to understand the physics behind the thickness of the thin film solar cell. First, we perform simulations of a thin silicon film of thickness $L_{Si} = 8c$. Second, we consider a photonic crystal back reflector of thickness $L_{Si} = 4c$ connected to a thin silicon film of thickness $L_{Si} = 8c$. Third, we perform simulations for a thin silicon film of thickness $L_{Si} = 12c$, which equals the combined thickness of a thin film and a photonic crystal back reflector in the second step. Finally, we compare the transmission and absorption spectra calculated in these three steps.

Figure 3.13 shows Fabry-Pérot fringes between $\lambda = 500$ nm and $\lambda = 1500$ nm in the transmission spectra for a thin silicon film with thicknesses $L_{Si} = 8c$ and $L_{Si} = 12c$. We deduce from Eq. 3.2 that the diffraction order of Fabry-Pérot fringes increases linearly with the increasing film thickness. Therefore, the number of Fabry-Pérot fringes in the transmission spectra for a thin film with thickness $L_{Si} = 12c$ is greater than in the film with thickness $L_{Si} = 8$. The amplitude of these Fabry-Pérot fringes decreases with the decreasing wavelength due to the
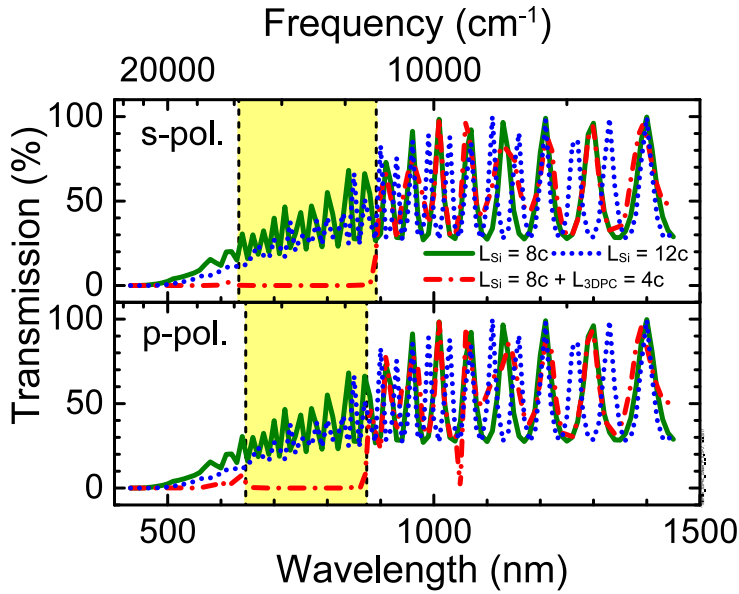
Figure 3.13: Calculated transmission spectra for a thin silicon film solar cell. Top panel: $s-$, bottom panel: $p-$polarized light. Green solid and the blue dotted curves are the results for a thin silicon film with thicknesses $L_{Si} = 8c$ and $L_{Si} = 12c$, respectively. Red dashed-dotted curves are results for a solar cell with a thin silicon film thickness $L_{Si} = 4c$ and a 3D inverse woodpile photonic crystal back reflector thickness $L_{3DPC} = 4c$. The vertical black dashed lines indicate the edges of the $s-$stop band in the top panel and $p-$stop band in the bottom panel. The stop bands are shown as the yellow bar.

increase in the imaginary part of the silicon refractive index, as discussed before in Section 3.3.1. The volume of silicon for the film thickness $L_{Si} = 12c$ is larger than for the film thickness $L_{Si} = 8c$. Therefore, the Fabry-Pérot fringes in the transmission spectra for the film thickness $L_{Si} = 12c$ decay faster by absorption than for the film thickness $L_{Si} = 8c$.

Figure 3.13 shows the transmission spectra for a thin silicon film with thickness $L_{Si} = 8c$ and a photonic crystal back reflector with thickness $L_{3DPC} = 4c$. We note that inside the stop bands between $\lambda = 600$ nm and $\lambda = 900$ nm the transmission for a thin film with a photonic crystal back reflector is considerably lower than for a thin film only with thicknesses $L_{Si} = 8c$ and $L_{Si} = 12c$. Therefore, even if we convert the part of the thin silicon film in a 3D inverse woodpile photonic crystal, the overall unabsorbed light transmitting through the solar cell diminishes to nearly 0% inside the stop bands. Thus, the transmission inside the broad stop bands would correspond to an effective thin film with an infinite thickness.

To investigate the stop band effect on absorption, we zoom in on the absorption spectra inside the stop bands in Fig. 3.7. Figure 3.14 shows the Fabry-Pérot
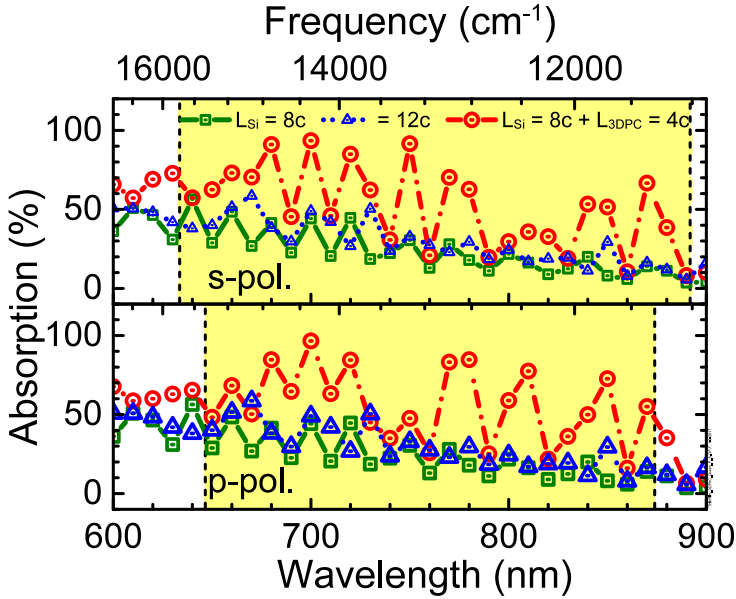
Figure 3.14: Absorption spectra in the stop band of a 3D inverse woodpile photonic crystal. Top panel: $s-$, bottom panel: $p-$polarized light. Green solid and the blue dotted curves are the results for a thin silicon film with thicknesses $L_{Si} = 8c$ and $L_{Si} = 12c$, respectively. Red dashed-dotted curves are results for a solar cell with a thin silicon film thickness $L_{Si} = 4c$ and a photonic crystal back reflector thickness $L_{3DPC} = 4c$. The vertical black dashed lines indicate the edges of the $s-$stop band in the top panel and $p-$stop band in the bottom panel. The stop bands are shown as the yellow bar.

fringes between $\lambda = 640$ nm and $\lambda = 900$ nm for a thin film with thicknesses $L_{Si} = 8c$ and $L_{Si} = 12c$. We note that the number of Fabry-Pérot fringes in the absorption spectra increases with increasing film thickness, as is evident from the Fabry-Pérot condition in Eq. 3.2. The thin film with thickness $L_{Si} = 12c$ has a larger silicon volume and hence has a slightly higher amplitude for the Fabry-Pérot fringes in the absorption spectra compared to the fringes for film thickness $L_{Si} = 8c$. Between $\lambda = 600$ nm and $\lambda = 900$ nm, Fig. 3.14 reveals that inside stop bands the amplitude of fringes in the absorption spectra for a thin film $L_{Si} = 8c$ with a photonic crystal back reflector $L_{3DPC} = 4c$ is significantly higher than for a thin film of total thickness $L_{Si} = 12c$. Using Eq. 3.4, the frequency-averaged absorption enhancement due to a photonic crystal back reflector is nearly $\eta_{abs} = 1.92$ for the $s-$stop band and nearly $\eta_{abs} = 2.1$ for the $p-$stop band compared to a thin film with thickness $L_{Si} = 12c$. Therefore, fabricating a 3D inverse woodpile photonic crystal in a part of the thin silicon film increases the overall absorption of the solar cell inside the stop bands, even though the silicon volume in the solar cell reduces. To obtain maximum efficiency for a given range of wavelengths keeping a constant thickness of a solar cell, one can find the
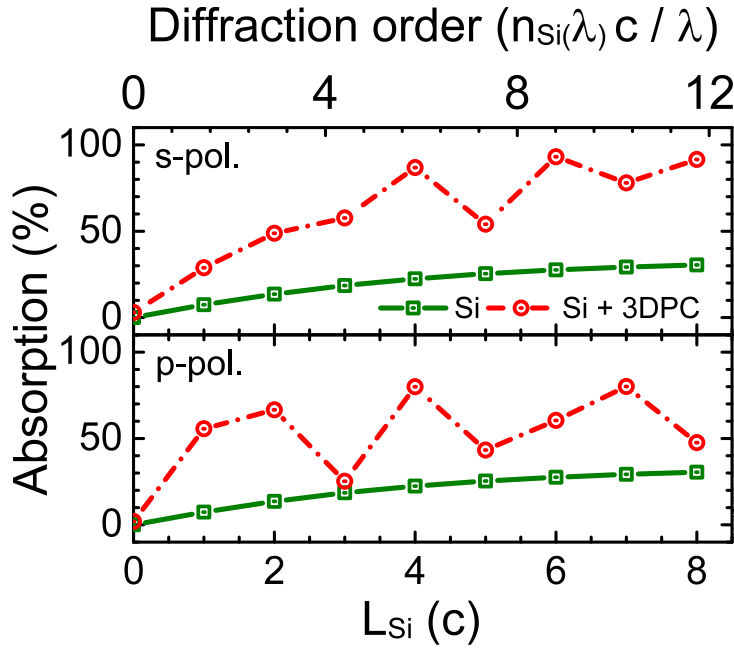
Figure 3.15: Absorption versus thickness of thin silicon film for a wavelength $\lambda = 760$ nm, which is inside the stop band of a 3D inverse woodpile photonic crystal for both s and p polarizations. Top panel: $s-$, bottom panel: $p-$polarized light. Green squares pertain to a thin silicon film. Red circles pertain to a thin silicon film with a 3D inverse woodpile photonic crystal back reflector. Green solid and red dashed-dotted curves are the guide to the eye showing modulations in absorption spectra. The top ordinate shows the diffraction order calculated using the Fabry-Pérot interference condition of Eq. 3.2.

optimized ratio between the thicknesses of a thin film and of a photonic crystal back reflector. Regarding thin silicon film solar cells, it is a generally advised not to etch features directly into the active region [8, 25]. Ref. 8 and Ref. 25 discuss that etching into deposited silicon can remove a significant part of the absorbing layer and texturing the surface of a thin-cut free-standing wafer can significantly reduces its mechanical strength. Therefore, experimental and numerical studies are needed to ascertain the impact of fabricating a 3D inverse woodpile photonic crystal back reflector in a thin silicon film on the overall photovoltaic efficiency.

3.3.6 Thickness of the absorbing layer

To investigate the effect of varying the thickness of the absorbing layer of a thin film silicon solar cell, we calculated the absorption for film thicknesses between $L_{Si} = c$ and $L_{Si} = 8c$. We studied 3D inverse woodpile photonic crystal of a constant thickness $L_{3DPC} = 4c$ as back reflector. Figure 3.15 shows the absorption spectra for a wavelength inside the stop band with varying thicknesses of

the thin film. We note that the absorption for a thin silicon film shows a monotonic increase with increasing film thickness for both polarizations. Figure 3.15 shows that the absorption for a thin film with a photonic crystal back reflector is always higher than the corresponding standalone thin silicon film. We observe that absorption spectra of a thin film with a photonic crystal back reflector reveals oscillations with increasing film thicknesses for both polarizations. These oscillations follow the diffraction order using the Fabry-Pérot interference condition of Eq. 3.2 and hence are Fabry-Pérot fringes. These Fabry-Pérot fringes are resulting from the multiple Bragg diffractions [27, 40, 41] between air-silicon and silicon-inverse woodpile interfaces. In order to maximize photovoltaic efficiency for a given wavelength, the thickness of a thin film had better be chosen to the maxima of the Fabry-Pérot fringes in Fig. 3.15.

3.3.7 Sub-wavelength thin absorbing layer

We found in Section 3.3.1 that a photonic crystal-thin film interface can couple the diffracted waves into guided resonant modes for a film thickness more than half of the wavelength of the incident light $L_{Si} \geq \frac{\lambda}{2n_{Si}(\lambda)}$. To investigate the role of guided modes, we study in this section the impact of a back reflector on a silicon absorbing layer with a thickness less than half of wavelength $\lambda/n_{Si}(\lambda)$ of the incident light. We reduce the thickness of the thin silicon film illustrated in Fig. 3.2 to $L_{Si} = 80$ nm, which does not satisfy the condition of guided resonant modes for any wavelength higher than $\lambda = 640$ nm. To accurately mesh this complex geometry, an upper limit $\triangle l \leq \frac{\lambda_0}{8\max(n_{Si})}$ is imposed to the edge length $\triangle l$ on any tetrahedron in the inverse woodpile photonic crystal and in the thin silicon film, with $\max(n_{Si})$ the maximum silicon refractive index for the selected range of wavelengths.

Figure 3.16 shows the absorption spectra for a sub-wavelength thin silicon film solar cell for both s and p polarizations. The absorption depth of silicon between $\lambda = 600$ nm and $\lambda = 900$ nm is nearly 1000 nm [31], which is very large compared to the thickness of absorbing layer $L_{Si} = 80$ nm. Therefore, the absorption for a thin silicon film with and without a perfect metallic back reflector is nearly 0% between $\lambda = 600$ nm and $\lambda = 900$ nm in Fig. 3.16. When a photonic crystal is employed as a back reflector to the sub-wavelength thin silicon film, we observe few sharp peaks appearing between $\lambda = 600$ nm and $\lambda = 900$ nm in Fig. 3.16. There are four absorption peaks (namely S1, S2, S3, and S4) inside the $s-$stop band and two absorption peaks (namely P1 and P2) inside the $p-$stop band. Since the thickness of the silicon film $L_{Si} = 80$ nm does not allow for guided resonance modes for these stop bands, the observed absorption peaks cannot be due to the guided resonant modes.

One can argue that these fringes are the result of the absorption in the extra silicon volume in the form of the photonic crystal back reflector. To investigate whether the absorption peaks appeared due to the absorption in the photonic crystal back reflector, we calculated the absorption within the volume of absorbing layer of the solar cell, using the power per unit volume formulae of Ref. 32. Figure 3.16 shows the comparison between absorption spectra for the absorbing
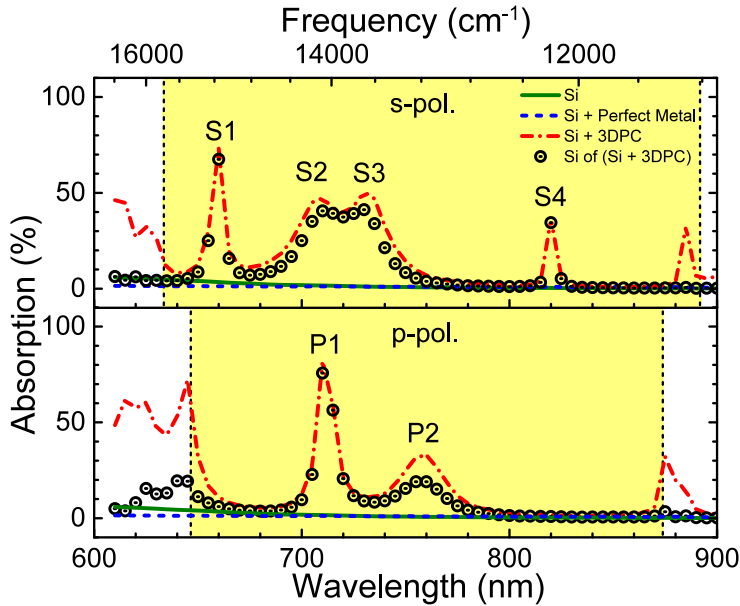
Figure 3.16: Absorption spectra for a sub-wavelength thin silicon film solar cell. Top panel: $s-$, bottom panel: $p-$polarized light. Green solid curves are absorption spectra calculated for a sub-wavelength thin silicon film. Blue dashed curves are absorption spectra calculated for a sub-wavelength thin silicon film with a perfect metallic back reflector. Red dashed-dotted curves are absorption spectra calculated for a sub-wavelength thin silicon film with a 3D inverse woodpile photonic crystal back reflector. Black circles represent the absorption in the silicon layer of a sub-wavelength thin silicon film with a photonic crystal back reflector. The vertical black dashed lines indicate the edges of the $s-$stop band in the top panel and $p-$stop band in the bottom panel. The stop bands are shown as the yellow bar.

layer of the solar cell and the complete solar cell. We observe that all six absorption peaks (namely S1, S2, S3, S4, P1, and P2) are also present in the absorption spectra calculated only for the absorbing layer of the solar cell. Therefore we conclude that the absorption in the high-index backbone of a 3D inverse woodpile photonic crystal back reflector is not the reason for the appearance of these peaks.

To reason with the physics behind these intriguing peaks, we investigate the distribution of the electric field in the computational cell at one peak for each polarization, *e.g.* S3 and P1. The incident electric field for s polarization is in the X direction and for the p polarization is in the Y direction. Therefore, we investigate the non-incident components of the electric field. Figure 3.17 shows distribution along X axis of E_z and E_y electric field components for s polarization and of E_z and E_x components for p polarizations. We observe that the high electric field is present either inside the thin film (in S3_Ey and P1_Ex) or at the thin film-photonic crystal interface (in S3_Ez and P1_Ez).
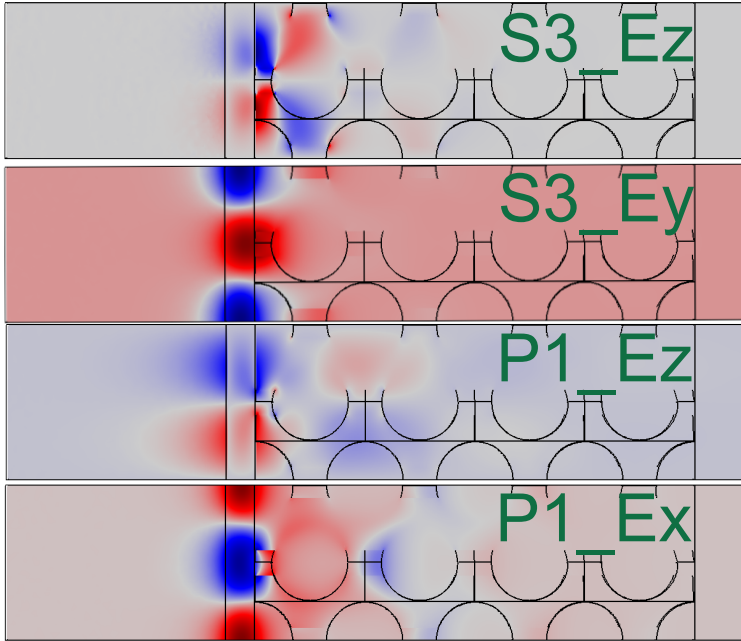
Figure 3.17: Distribution of the electric field components along the Z axis of the computational cell illustrated in Fig. 3.2. S3 and P1 represent the absorption peaks present in Fig 3.16. Red and blue denote the maxima and the minima of the electric field components, respectively.

In S3_Ey and P1_Ex, the high electric field distributions show the periodic variations in the plane of the thin film that are characteristic of guided resonances [18, 42]. Since the thickness of the silicon film does not satisfy the condition of the guided resonant modes, we investigate the physics behind the reflectivity from the photonic crystal. The incident light is completely reflected by the photonic crystal after covering the Bragg attenuation length [40]. Chapter 2 shows that the Bragg attenuation length for an inverse woodpile is frequency dependent and is nearly $L_B = 0.6c$ at the p-stop band center. Hence, the sum of the Bragg attenuation length for an inverse woodpile and the thickness of the silicon film can satisfy the condition of the guided resonances at discrete frequencies (or wavelengths) and hence these peaks appear.

In S3_Ez and P1_Ez, the high electric field distributions localized at the air-film and at the film-photonic crystal interfaces decay away from the interfaces. These field distributions are plausibly the signature of the confinement of the surface mode [26, 43]. Hence, we visualize the structure in this section as a thin absorbing dielectric film added on top of a photonic crystal in order to confine a surface-defect, which causes the propagation of the incident wave via the surface state resonances. Therefore, the intriguing peaks observed in Fig. 3.16 are the combined effect of two physical mechanisms: (i) a guided resonance due to the Bragg attenuation length and (ii) confinement due to a surface-defect.

3.4 Conclusions and outlook

We have studied the absorption of light by a thin silicon film with and without a back reflector by numerical methods. We investigated a thin 3D photonic band gap crystal as a back reflector in the visible regime, which reflects light within the band gap for all directions and for all polarizations. We used finite-element computations of the 3D time-harmonic Maxwell equations to calculate absorption of a thin silicon film solar cell with a 3D inverse woodpile photonic crystal back reflector. We tailored the finite-sized inverse woodpile crystal design to have a broad photonic band gap in the visible range. We have used the refractive index of real silicon including dispersion and absorption, in order to make our calculations relevant to experiments. From the comparison of the photonic crystal back reflector to a perfect metallic back reflector, we infer that a photonic crystal back reflector increases the number of Fabry-Pérot fringes for a thin film, without changing the effective refractive index of silicon. We observe that a 3D inverse woodpile photonic crystal enhances the absorption of a thin silicon film by (i) behaving as a perfect reflector, exhibiting nearly 100% reflectivity in the stop bands, as well as (ii) generating guided resonant modes at many discrete wavelengths. Our absorption results show nearly 2.62 times enhanced frequency-, angle-, polarization-averaged absorption between $\lambda = 680$ nm and $\lambda = 890$ nm compared to a 2400 nm thin silicon film. We find that the photovoltaic efficiency is enhanced by positioning an inverse woodpile back reflector at the back end of a thin silicon film, which will keep the length of the solar cell unchanged as well as make the thin film solar cell lighter. In order to maximize the efficiency for a given wavelength, we show that the thickness of a thin film had better be chosen to the maxima of the Fabry-Pérot fringes. For a sub-wavelength thin absorbing layer with a photonic crystal back reflector, we identify and demonstrate two physical mechanisms causing the giant enhancement at discrete wavelengths: (i) a guided resonance due to the Bragg attenuation length and (ii) confinement due to a surface-defect.

In order to enhance the absorption of light over a wavelength range broader than reported here, we propose to employ an inverse woodpile crystal with the light incident in the ΓY direction as a back reflector for a thin film. The reason is that for a 3D silicon inverse woodpile photonic crystal, the ΓY stop gap (relative bandwidth 39.1 %) is about $1.3\times$ broader than the ΓZ (or symmetry-related ΓX) stop gap (relative bandwidth 30.4 %) [27, 29, 30, 37]. Moreover, the stop gap of an inverse woodpile crystal depends on the lattice parameters and gives perfect reflectivity, provided the Bragg attenuation length of an inverse woodpile crystal is smaller than the absorption length of silicon. Therefore, a novel back reflector consisting of a series of inverse woodpile crystals with varying lattice parameters and different stop gaps will enhance the absorption over a broad wavelength range, which will be the combination of individual stop gaps.
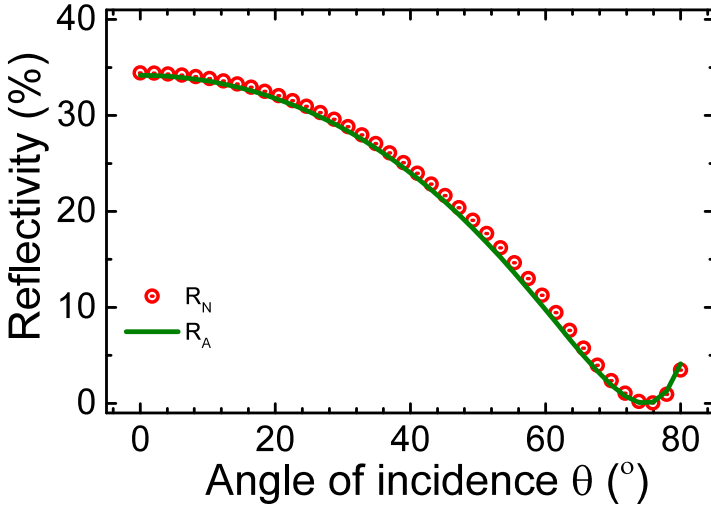
Figure 3.18: Analytical calculation versus numerical calculation for reflectivity of a semi-infinite dielectric medium for p polarization at wavelength $\lambda = 752$ nm, in the visible regime. Data for the refractive index of the dielectric medium is obtained from Ref. 31. The analytically calculated reflectivity (R_A) is shown in green line. R_A is exact only for $\theta = 0°$. Blue circles represent the numerically computed reflectivity (R_N).

3.A Analytical validation of the numerical scheme with a semi-infinite homogeneous medium

To validate our numerical scheme, we calculate reflectivity spectra of a system that can be analytically analyzed using Fresnel's equations with absorption, namely a homogeneous dielectric medium [15, 39]. We consider $p-$polarized plane waves at a single frequency with a range of angles of incidence. We replace the photonic crystal and the air layer on the right in Fig. 3.2 with a homogeneous silicon medium. This results in a semi-infinite homogeneous medium that is separated from the source by an air layer and a silicon-air interface. This numerical calculation is performed for the mesh resolution same as the one used in Section 3.2. The angular resolution is $2°$.

In Fig 3.18 we show the calculated reflectivity spectra of a semi-infinite homogeneous medium for the above defined reference computational cell. We note that the numerical calculation agrees very well with the analytical results from the Fresnel equations using the dispersive and complex refractive index of silicon. We observe the Brewster angle at $\theta_B = 75.3°$, which matches the value obtained from an analytical calculation of Heavens [39]. Ref. 39 gives an exact expression of the reflectivity only at normal incidence to the surface of a semi-infinite absorbing medium. To calculate the relative error $\triangle R_{rel}$ between the numerical

calculation and the analytical result, we employ the definition

$$\triangle R_{rel} \equiv \left(\frac{R_{A,0} - R_{N,0}}{R_{A,0}} \right) \tag{3.6}$$

with $R_{N,0}$ the numerical reflectivity, and $R_{A,0}$ the analytical reflectivity at normal incidence. For the solution shown in Fig. 3.18, the error is only about $\triangle R_{rel} = 0.007$. Therefore, the error bar on our calculated results is estimated to be 0.7%, which is clearly sufficient to assess the role of a photonic crystal back reflector.

3.B Analytical validation of the numerical scheme with a homogeneous thin-film

To validate our numerical scheme for two interfaces, we calculate the reflectivity spectra of a system that can be analytically approximated using Fresnel's equations with absorption, namely a homogeneous dielectric film [15, 39]. We consider $p-$polarized plane waves. We replace the photonic crystal on the right in Fig. 3.2 with a homogeneous silicon medium. This results in a homogeneous film of silicon that is separated from the source by an air layer and a silicon-air interface. This numerical calculation is performed for the same mesh resolution as the one used in Section 3.2. Figure 3.8 shows the calculated analytical spectra of a thin silicon film for the above defined reference computational cell. We note that the numerical calculation agrees very well with the analytical results obtained from the Fresnel equations using the dispersive and complex refractive index of silicon. To calculate the relative error $\triangle R_{rel}$ between the numerical calculation and the analytical result, we employ the definition

$$\triangle R_{rel} \equiv \frac{1}{n} \sqrt{ \left(\sum_{i=1}^{n} \left(\frac{(T_{A,i} - T_{N,i})^2}{T_{A,i}^2} + \frac{(R_{A,i} - R_{N,i})^2}{R_{A,i}^2} \right) \right) } \tag{3.7}$$

with $(T_{N,i}, R_{N,i})$ the numerical transmission and reflectivity, and $(T_{A,i}, R_{A,i})$ the analytical transmission and reflectivity and n the number of wavelengths. For the solution shown in Fig. 3.8, the error is only about $\triangle T_{rel} = 0.0035$, hence we consider the calculation to be converged.

Bibliography

[1] A. L. Fahrenbruch and R. H. Bube, *"Fundamentals in Solar Cells"* (Academic Press, New York, 1983). 51

[2] A. Rohatgi, E. Weber, and L. C. Kimerling, "Opportunities in silicon photovoltaics and defect control in photovoltaic materials," J. Electron. Mater. **22**, 65 (1993). 51

[3] T. Tiedje, E. Yablonovitch, G. D. Cody, and B. G. Brooks, "Limiting efficiency of silicon solar cells," IEEE Trans. Electron Devices **31**, 711 (1984). 51

[4] M. A. Green, K. Emery, Y. Hishikawa, W. Warta, and E. D. Dunlop, "Solar cell efficiency tables (Version 45)," Prog. Photovolt. **20**, 606 (2012). 51

[5] P. Sheng, A. N. Bloch, and R. S. Stepleman, "Wavelength-selective absorption enhancement in thin-film solar cells," Appl. Phys. Lett. **43**, 579 (1983). 51

[6] C. Herzinger, B. Johs, W. McGahan, J. Woollam, and W. Paulson, "Ellipsometric determination of optical constants for silicon and thermally grown silicon dioxide via a multi-sample, multi-wavelength, multi-angle investigation," J. Appl. Phys. **83**, 3323 (1998). 51

[7] ASTMG173-03, *"Standard tables for reference solar spectral irradiances: direct normal and hemispherical on 37 degree tilted surface,"* (ASTM International, West Conshohocken, Pennsylvania, 2005). 51

[8] K. Münzer, K. T. Holdermann, R. E. Schlosser, and S. Sterk, "Thin monocrystalline silicon solar cells," IEEE Trans. Electron Devices **46**, 2055 (1999). 51, 71

[9] A. V. Shah, H. Schade, M. Vanecek, J. Meier, E. Vallat-Sauvain, N. Wyrsch, U. Kroll, C. Droz, and J. Bailat, "Thin-film silicon solar cell technology," Prog. Photovolt., **12**, 113 (2004). 51

[10] N-Ning Feng, J. Michel, L. Zeng, J. Lie, C-Yin Hong, L. C. Kimerling, and X. Duan, "Design of highly efficient light-trapping structures for thin-film crystalline silicon solar cells," IEEE Trans. Electron Devices **54**, 1926 (2007). 51

[11] Z. Yu, A. Raman, and S. Fan, "Fundamental limit of nanophotonic light trapping in solar cells," Proc. Natl. Acad. Sci. U.S.A. **2010**, 17491 (2010). 51

[12] E. Yablonovitch and G. Cody, "Intensity enhancement in textured optical sheets for solar cells," IEEE Trans. Electron Devices **29**, 300 (1982). 51

[13] E. Moulin, U. W. Paetzold, H. Siekmann, J. Worbs, A. Bauer, and R. Carius, "Study of thin-film silicon solar cell back reflectors and potential of detached reflectors," Energy Procedia **10**, 106 (2011). 51

[14] R. Brendel, M. Hirsch, R. Plieninger, and J.Werner, "Quantum efficiency

3

analysis of thin-layer silicon solar cells with back surface fields and optical confinement," IEEE Trans. Electron Devices **43**, 1104 (1996). 51

[15] D. J. Griffiths, *"Introduction to electrodynamics,"* (Prentice Hall, Upper Saddle River NJ, 1999). 52, 54, 56, 61, 76, 77

[16] W. Wang, S. Wu, K. Reinhardt, Y. Lu, and S. Chen, "Broadband light absorption enhancement in thin-film silicon solar cells," Nano Lett., **10**, 2012 (2010). 52

[17] A. Polman and H. A. Atwater, "Photonic design principles for ultrahigh-efficiency photovoltaics," Nat. Mater **11**, 174 (2012). 52

[18] M. Brongersma, Y. Cui, and S. Fan, "Light management for photovoltaics using high-index nanostructures," Nat. Mater. **13**, 451 (2014). 52, 74

[19] S. Nishimura, N. Abrams, B. A. Lewis, L. I. Halaoui, T. E. Mallouk, K. D. Benkstein, J. van de Lagemaat, and A. J. Frank, "Standing wave enhancement of red absorbance and photocurrent in dye-sensitized titanium dioxide photo-electrodes coupled to photonic crystals," J. Am. Chem. Soc. **125**, 6306 (2003). 52

[20] A. Mihi and H. Miquez, "Origin of light-harvesting enhancement in colloidal-photonic-crystal-based dye-sensitized solar cells," J. Phys. Chem. B **109**, 15968 (2005). 52

[21] P. Bermel, C. Luo, L. Zeng, L. C. Kimerling, and J. D. Joannopoulos, "Improving thin-film crystalline silicon solar cell efficiencies with photonic crystals," Opt. Express **15**, 25 (2007). 52

[22] P. G. O'Brien, N. P. Kherani, A. Chutinan, G. A. Ozin, S. John, and S. Zukotynski, "Silicon photovoltaics using conducting photonic crystal back-reflector," Adv. Mater. **20**, 1577 (2008). 52, 61

[23] B. Curtin, R. Biswas, and V. Dalal, "Photonic crystal based back reflectors for light management and enhanced absorption in amorphous silicon solar cells," Appl. Phys. Lett. **95**, 231102 (2009). 52

[24] L. Zeng, P. Bermel, B. A. Alamariu, K. A. Broderick, J. Liu, X. Duan, J. Joannopoulos, and L. C. Kimerling, "Demonstration of enhanced absorption in thin film Si solar cells with textured photonic crystal back reflector," Appl. Phys. Lett. **93**, 221105 (2008). 52

[25] R. Biswas, J. Bhattacharya, B. Lewis, N. Chakravarty, and V. Dalal, "Enhanced nanocrystalline silicon solar cell with a photonic crystal back-reflector," Sol. Energy Mat. Sol. Cells **94**, 2337 (2010). 52, 60, 71

[26] J. D. Joannopoulos, S. G. Johnson, J. N. Winn, and R. D. Meade, "Photonic crystals: Molding the flow of light," (Princeton University Press, Princeton NJ, 2008). 52, 53, 60, 65, 74

[27] D. Devashish, S. B. Hasan, J. J. W. van der Vegt, and W. L. Vos, "Reflectivity calculated for a three-dimensional silicon photonic band gap crystal with finite support," Phys. Rev. B **95**, 155141 (2017). 53, 72, 75

[28] K. M. Ho, C. T. Chan, C. M. Soukoulis, R. Biswas, and M. Sigalas, "Photonic band gaps in three dimensions: new layer-by-layer periodic structures," Solid State Commun. **89**, 413 (1994). 53

[29] R. Hillebrand, S. Senz, W. Hergert, and U. Gösele, "Macroporous-silicon-based three-dimensional photonic crystal with a large complete band gap," J.

Appl. Phys. **94**, 2758 (2003). 53, 75

[30] L. A. Woldering, A. P. Mosk, R. W. Tjerkstra, and W. L. Vos, "The influence of fabrication deviations on the photonic band gap of three-dimensional inverse woodpile nanostructures," J. Appl. Phys. **105**, 093108 (2009). 53, 75

[31] M. A. Green, "Self-consistent optical parameters of intrinsic silicon at 300K including temperature coefficient," Sol. Energy Mat. Sol. Cells, **92**, 1305 (2008). 53, 55, 56, 57, 58, 72, 76

[32] "COMSOL Multiphysics® v. 5.2. www.comsol.com, COMSOL AB, Stockholm, Sweden". 53, 65, 72

[33] J.M. Jin, *"The finite element method in electromagnetics"* (Wiley-IEEE Press, New York, 2000). 54

[34] Serendipity is a high performance computing cluster made by Dell at MACS, University of Twente. It consists of 16 nodes, each node having 40 cores. Each node has 56 GBPS speed and 256 GB memory. 54

[35] G. Vuye, S. Fisson, V. Nguyen Van, Y. Wang, J. Rivory, and F. Abelés, "Temperature dependence of the dielectric function of silicon using *in situ* spectroscopic ellipsometry," Thin Solid Films, **233**, 166 (1993). 55

[36] G. E. Jellison Jr., "Optical functions of silicon determined by two-channel polarization modulation ellipsometry," Opt. Mater. **1**, 41 (1992). 55

[37] S. R. Huisman, R. V. Nair, L. A. Woldering, M. D. Leistikow, A. P. Mosk, and W. L. Vos, "Signature of a three-dimensional photonic band gap observed with silicon inverse woodpile photonic crystals," Phys. Rev. B **83**, 205313 (2011). 55, 60, 75

[38] M. D. Leistikow, A. P. Mosk, E. Yeganegi, S. R. Huisman, A. Lagendijk, and W. L. Vos, "Inhibited spontaneous emission of quantum dots observed in a 3D photonic band gap," Phys. Rev. Lett. **107**, 193903 (2011). 55, 60

[39] O. S. Heavens, *"Optical properties of thin solid films"* (Dover Publications, New York, 1965). 56, 61, 76, 77

[40] A. Yariv and P. Yeh, *"Optical waves in crystals: propagation and control of laser radiation"* (Wiley, New York NY, 1980), Chapter 6, pp. 155-219. 56, 72, 74

[41] E. Yeganegi, A. Lagendijk, A. P. Mosk, and W. L. Vos, "Local density of optical states in the band gap of a finite one-dimensional photonic crystal," Phys. Rev. B **89**, 045123 (2014). 72

[42] S. Fan and J. D. Joannopoulos, "Analysis of guided resonances in photonic crystal slab," Phys. Rev. B. **65**, 235112 (2002). 74

[43] K. Ishizaki and S. Noda, "Manipulation of photons at the surface of three-dimensional photonic crystals," Nature (London) **46**, 367 (2009). 74

3

CHAPTER 4

Large energy enhancement at cavity resonances in a three-dimensional photonic band gap crystal with finite support

4.1 Introduction

Capturing light in a minuscule spatial volume is a flourishing field of nanophotonics [1, 2]. Notable applications are trapping or slowing down of photons [1], sensing for bio applications [3], controlled enhancement of spontaneous emission [4], and cavity quantum electrodynamics [5–7]. Up to date, many devices have been reported including microspheres [8, 9], micropillars [4, 10], microdisks [14], Fabry-Pérot-type plasmon cavities [11, 12], microtoroids [13], or photonic crystal cavities [15, 16].

Among recent developments, a cavity formed by a defect embedded in a three-dimensional photonic band gap crystal has a prime significance [17, 18], since the confinement of light is truly three-dimensional and there is no leakage of light as in, *e.g.*, a pillar or a 2D photonic crystal. A defect in a photonic crystal is formed by either the addition or the removal of the high-index backbone material [19]. The defect formed by adding the high-index backbone material is called a donor defect and the one formed by removing the high-index backbone material is called an acceptor defect [19–21], since in the first case the defect level derives from the high frequency (= "conduction") bands, whereas in the second case the level derives from the low frequency (= "valence") bands [22].

3D inverse woodpile photonic crystals are symmetry related to the cubic diamond crystals [23] and are known for their broad band gaps [24, 25], which lead to an optimal shielding of the embedded cavity. Ref. 26 proposed a design for a cavity in a 3D inverse woodpile photonic crystal, where the point defect that acts as a cavity is formed in the proximal region of two orthogonal pores with a radius that differs from the ones in the bulk of the crystal, as illustrated in Fig. 4.1. For an inverse woodpile crystal, Woldering *et al.* observed that the cavity resonances occur only for smaller defect pores (yielding donor levels), but not for larger ones, thus no acceptor levels appear. Moreover, they found that it takes a certain threshold in the pore radius change $\triangle r > 0$ to observe the cavity resonances. Each of these resonances has a frequency ω nearly invariable with the wave vector $\vec{k}$. Therefore, it is logical by Fourier transform that the resonance frequency ω_c is localized in real space $\vec{r}$ and hence ω_c will be independent of the incident angle
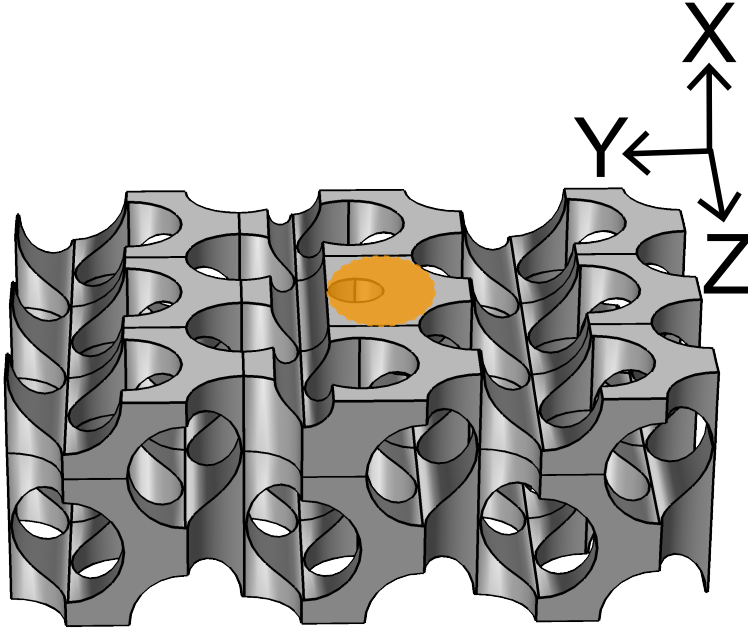
Figure 4.1: Schematic illustration of a cubic inverse woodpile photonic crystal with a point defect. The structure has been cut through the center of the cavity and parallel to the YZ plane. The proximal region of the two defect pores, each with a radius smaller than the bulk radius, results in a region with an excess of high-index material, indicated by the orange ellipse.

in reflectivity. The small mode volume of order $V \simeq \lambda^3$ (resonance wavelength cubed) of the cavity resonances reported by Ref. 26 will lead to a large Purcell factor [27] and ultimately a large local enhancement of the spontaneous emission rate of an emitter [4, 28–31]. However, since the calculation performed by Ref. 26 has no surrounding vacuum, the cavity quality factor cannot be calculated and the Purcell factor could not be studied.

Here we investigate the optical properties of photonic band gap cavities with a design as in Ref. 26. Therefore, we study the reflectivity and absorption of a 3D silicon inverse woodpile photonic crystal with symmetry-disruption due to finite support and an intentional point defect. By comparing defect bands in the band structure for an infinite crystal and troughs in the reflectivity spectra for a finite crystal, we identify cavity resonances and their field patterns. We verify the angle-dependency to confirm the localization of the cavity resonances in real space. Since the photonic crystal has a finite support, we calculate the quality factor and hence the Purcell factor for these resonances. We calculate the accurate electric-field energy enhancement due to these resonances and assess their potential application to enhance the photovoltaic efficiency. To investigate the effect of the point defect on the linear regime of the band structure, we study resonances existing below the 3D band gap of a perfect crystal. Consequently, our

numerical analysis provides a novel insight in understanding resonances appearing due to the locally disrupted lattice symmetry in a 3D inverse woodpile photonic crystal and their potential application in photovoltaics.

4.2 Methods

Woldering *et al.* [26] calculated the photonic band structure (frequency ω versus wave vector $\vec{k}$) of a supercell of the 3D inverse woodpile photonic crystal by employing a plane-wave expansion method [32] that assumes the structure to be infinitely extended. They reported that the defect pore radius $r' = 0.5r$ gives optimal light confinement. In order to relate to previous results, we tuned the parameters in our calculations, namely an optimal ideal pore radius [24, 33] $\frac{r}{a} = 0.24$, an optimal defect pore radius [26] $\frac{r'}{a} = 0.12$, and a dielectric permittivity [25, 34] $\epsilon = 12.1$, typical for silicon in the near infrared and telecom ranges.

To investigate features related to the finite size or to unavoidable deviations from perfect periodicity, we study the reflectivity spectra for the complex system of the photonic crystal with finite support and with a point defect. We employ the commercial COMSOL finite-element method (FEM) [35] solver to solve the time-harmonic Maxwell equations. We employ Bloch-Floquet periodic boundaries in the $\pm X$ and the $\pm Y$ directions to describe a thin slab [22]. We use incident plane waves with either s polarization (the electric field perpendicular to the plane of incidence) or p polarization (the magnetic field normal to the plane of incidence), and with an angle of incidence that we discretely varied between $0°$ and $80°$. To compute the reflectivity spectra for a crystal with finite support, absorbing boundaries are employed in the $-Z$ and $+Z$ directions. Therefore, there is only one point defect in the direction of propagation of the incident plane wave. The incident field starts from a plane in the $-Z$ direction that is separated from the crystal by an air layer. The plane represents a boundary condition rather than a true current source since it also absorbs the reflected waves [36]. Since our results in Chapter 2 and Ref. 37 revealed that a thickness $L \geq 3c$ (c is the lattice parameter for an inverse woodpile crystal) is sufficient to show the band gap property of a perfect 3D inverse woodpile crystal, we select $3 \times 3 \times 3$ as the dimension of the super cell, as illustrated in Fig. 4.1.

We investigate the symmetry-disruption effect of the crystal interfaces by comparing the reflectivity spectra for a thin slab to the corresponding photonic band structure for an infinitely extended crystal. In order to eliminate the possible deviation arising due to differences in the numerical methods or the dielectric permittivity distributions, we employ the eigenvalue solver of the COMSOL finite-element method (FEM) [35] to compute the photonic band structure. Since a photonic band structure pertains only to an infinitely extended crystal, we alter our finite reflectivity computational cell by employing Bloch-Floquet periodic boundaries in all three directions $\pm X$, $\pm Y$, and $\pm Z$ directions [22]. Therefore, this supercell is replicated infinitely and a point defect occurs once every three unit cells in each dimension. Furthermore, we highlight the contrast between the

band structures obtained from the plane-wave expansion method and the finite element method in Appendix 4.A.

We use tetrahedra as basic elements in our finite element mesh to subdivide the 3D computational cell into elements. To accurately mesh sharp interfaces in a 3D inverse woodpile crystal, an upper limit of $\triangle l \leq \frac{\lambda_0}{8\sqrt{\epsilon_{max}}}$ is imposed to the edge length $\triangle l$ on any tetrahedron in the inverse woodpile, with ϵ_{max} the maximum dielectric permittivity for the selected range of frequencies. We show an extensive analysis of the mesh convergence in Appendix 4.B. To detect all possible reflectivity troughs, we use a frequency resolution of $\delta\tilde{\omega} = 0.0005$ for the calculations in the 3D band gap and $\delta\tilde{\omega} = 0.001$ below the 3D band gap [38]. We perform the frequency convergence analysis in Appendix 4.C. All calculations are performed on the "Serendipity" cluster [39] at MACS in MESA+.

In order to simplify the physical interpretation of the point defect in a 3D inverse woodpile photonic crystal, we decided to consider the 3D photonic band gap of a perfect inverse woodpile as the reference, where the band gap exists between $\tilde{\omega} = 0.51$ and $\tilde{\omega} = 0.646$ as shown in Fig. 4.2. So we subdivide the frequency range into two parts: the range below the 3D band gap and the range consisting of defect bands in the 3D band gap.

4.3 Results

4.3.1 Cavity resonances within the 3D band gap

The middle panel of Fig. 4.2 shows the polarization-resolved band structure for a $3 \times 3 \times 3$ supercell of the 3D inverse woodpile photonic crystal with a point defect. With increasing frequency starting from the bottom of the band gap at $\tilde{\omega} = 0.51$, we observe that there is one isolated s-polarized defect band S1 at $\tilde{\omega} = 0.5144$ and four isolated p-polarized defect bands P1, P2, P3, and P4 at $\tilde{\omega} = 0.5140, 0.5213, 0.5376$, and 0.5441, respectively. Ref. 26 also reported five isolated defect bands without mentioning the polarization states and at frequencies nearly $\triangle\tilde{\omega} = 0.007$ higher than our calculations. This frequency shift is attributed to different spatial resolutions and numerical methods employed to calculate the band structures (see Appendix 4.A for the detailed comparison). There are numerous $s-$ and $p-$defect bands beyond $\tilde{\omega} = 0.55$, but they are neither isolated nor dispersionless. Therefore, we disregard them as potential cavity resonances, similar to Ref. 26.

Since a defect band in the band structure corresponds to a frequency at which incident light can couple to a Bloch mode in the photonic crystal, it is expected that there is a trough in the reflectivity spectra corresponding to each of the five isolated defect bands. In order to identify these resonance troughs, we calculate reflectivity inside the 3D band gap at normal incidence for a $3 \times 3 \times 3$ supercell of the 3D inverse woodpile photonic crystal with a point defect. The top and bottom panels of Fig. 4.2 show the reflectivity spectra for s and p polarizations, respectively. We observe a multitude of troughs between $\tilde{\omega} = 0.50$ and $\tilde{\omega} = 0.55$ for both polarizations.
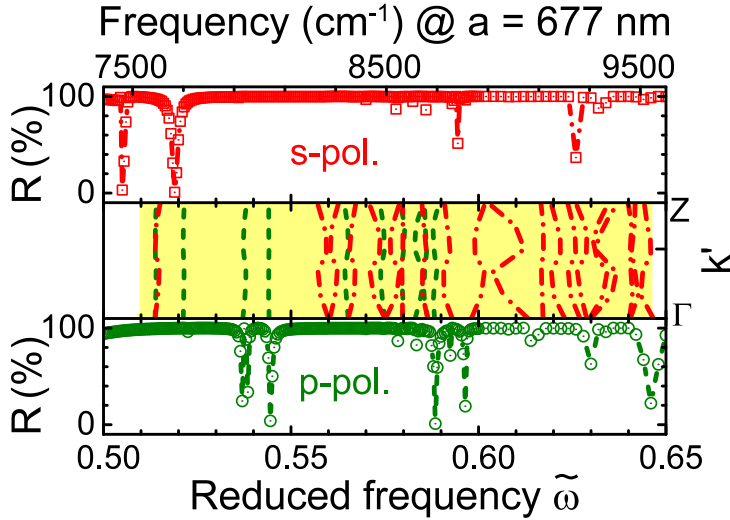
Figure 4.2: Reflectivity spectra in the 3D band gap calculated for a 3D inverse wood-pile photonic crystal with a point defect at normal incidence in the ΓZ direction. In the top and bottom panels, red dashed-dotted and green dashed curves are reflectivity spectra for s and p polarizations, respectively. The middle panel shows the band structure for the ΓZ direction, where the 3D band gap of the perfect crystal is shown with the yellow bar. The wave vector is expressed as $k' = (ka/2\pi)$. Red dashed-dotted lines indicate the $s-$polarized bands and green dashed lines indicate $p-$polarized bands.

To match a defect band for an infinite crystal to a corresponding reflectivity trough for a finite crystal, we cross-correlate the spatial distribution of the electric-field $|E|(\vec{r}, \tilde{\omega}_i)$ of a defect band $\tilde{\omega}_i$ with a field $|E|(\vec{r}, \tilde{\omega})$ calculated at a frequency $\tilde{\omega}$ in the reflectivity spectra. We take the cross section through the center of the cavity and parallel to the YZ plane (see Fig. 4.1). To calculate the normalized cross-correlation $C(\Delta r, \tilde{\omega}, \tilde{\omega}_i)$ of the field pattern $|E|(\vec{r}, \tilde{\omega}_i)$ at a reference point r_0 and $|E|(\vec{r}, \tilde{\omega})$ at position $(r_0 + \Delta r)$, we employ the definition [40]:

$$C(\Delta r, \tilde{\omega}, \tilde{\omega}_i) \equiv \frac{\int_0^{L_t} \Big(|E|(r_0, \tilde{\omega}_i) |E|(r_0 + \Delta r, \tilde{\omega}) \Big) dr}{\left[\int_0^{L_t} (|E|(r_0, \tilde{\omega}_i))^2 dr \int_0^L (|E|(r_0 + \Delta r, \tilde{\omega}))^2 dr \right]^{\frac{1}{2}}}, \qquad (4.1)$$

where Δr is the translation from the reference position r_0 and L_t is the transverse length until which the electric field is matched. Fig. 4.3 shows the cross-correlation $C(\tilde{\omega}, \tilde{\omega}_i)$ for a Δr at which $C(\Delta r, \tilde{\omega}, \tilde{\omega}_i)$ is maximum.

A reflectivity resonance with a field that cross-correlates to 1 at its central frequency $\tilde{\omega}_c$ will correspond to a defect band $\tilde{\omega}_i$. We further confirm the cavity resonance by the visual inspection of the cross sections of the electric-field distribution. In order to verify the 3D band gap confinement of light, we check the angular dependence of a cavity resonance.
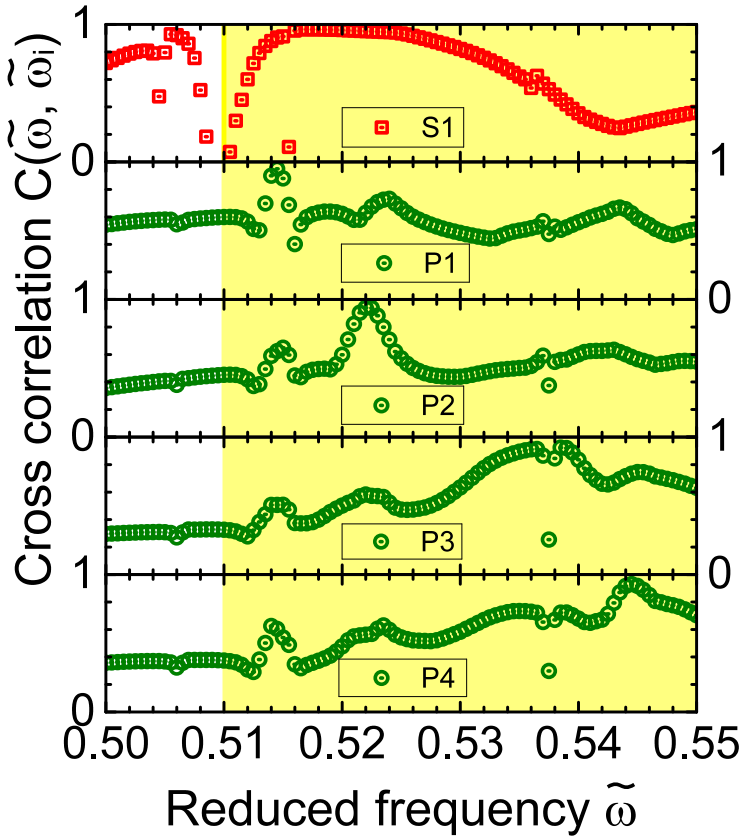
Figure 4.3: Normalized cross-correlation between the cross sections of the electric-field distribution ($|E|$) at the defect bands $\tilde{\omega}_i$ in the bandstructure and fields at discrete frequencies $\tilde{\omega}$ in the reflectivity spectra for a finite 3D inverse woodpile photonic crystal with a point defect. The 3D band gap of the perfect crystal is shown with the yellow bar. S1 indicates the single s-polarized cavity resonance inside the 3D band gap. Similarly, P1, P2, P3, and P4 indicate the four p-polarized cavity resonances inside the 3D band gap.

We will now apply our cross-correlation method to identify the five defect bands with corresponding resonances in reflectivity. Simultaneously, we will identify the spatial field distributions of each resonance. From the five resonances S1, P1, P2, P3, and P4, it appears that P1, P2, and P4 show relatively straightforward behavior, therefore we first discuss these three resonances, before analyzing the more complex behavior of S1 and P3 resonances.

If we cross-correlate the field of the P1 defect band at $\tilde{\omega}_i = 0.5140$ with the finite crystal fields as a function of frequency $\tilde{\omega}$, we see in Fig. 4.3 that the cross correlation equals about 0.6 everywhere, with a marked peak at $\tilde{\omega} = 0.5140$. This cross correlation peak with $C = 1$ corresponds to a tiny resonance trough
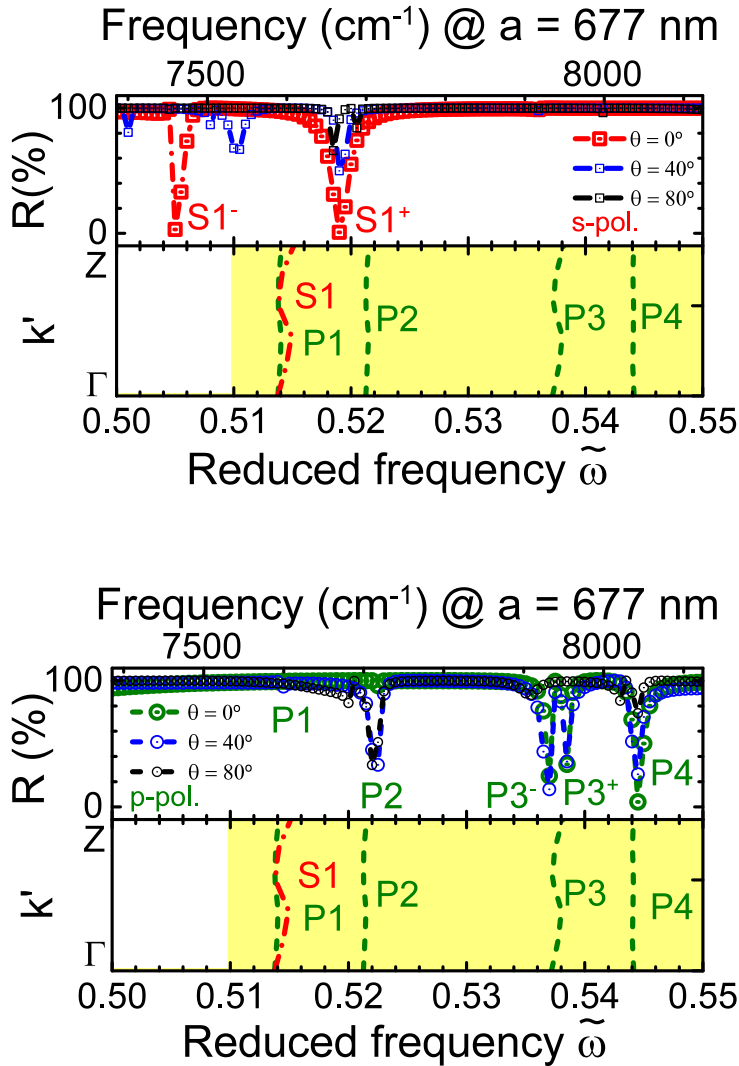
Figure 4.4: Reflectivity near the bottom of the 3D band gap for (a) $s-$ and (b) $p-$polarized light for a 3D inverse woodpile photonic crystal with a point defect. In panels (i), red dashed-dotted and green dashed curves are calculated results at normal incidence, as in Fig. 4.2. Blue solid and black curves in panels (i) are reflectivity spectra for angles of incidence $40°$ and $80°$, respectively, off normal in the ΓZ direction. Panels (ii) show the band structures for (a) $s-$ and (b) $p-$polarized light. The wave vector is expressed as $k' = (ka/2\pi)$. The 3D band gap of a perfect crystal is shown with the yellow bar. $S1^-$, $S1^+$, P1, P2, $P3^-$, $P3^+$, and P4 are reflectivity resonances. Angle-dependent reflectivity troughs are speckles, plausibly due to calculations for finite sized crystals.
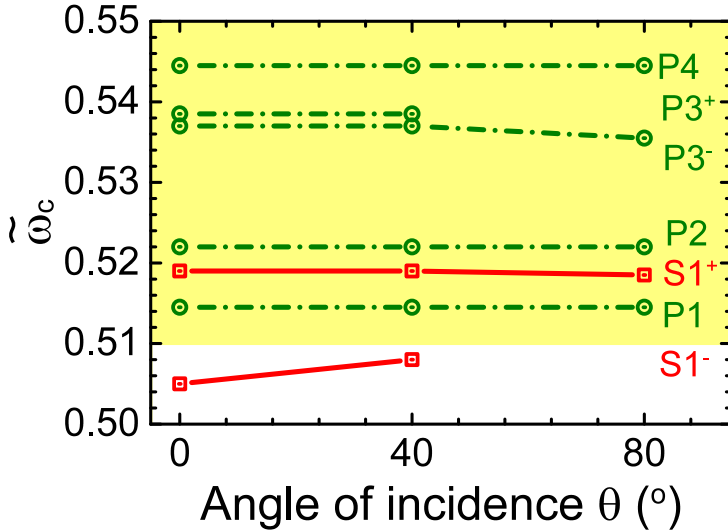
Figure 4.5: The central frequency of a resonance trough versus angle of incidence. S1$^-$, S1$^+$, P1, P2, P3$^-$, P3$^+$, and P4 are reflectivity resonances in the spectra in Fig. 4.4. The 3D band gap of a perfect crystal is shown with the yellow bar.

in reflectivity ($R_{min} \simeq 99\%$) at normal incidence. Upon varying the angle of incidence of light on the finite structure, see Fig. 4.4 (b), we observe firstly that the reflectivity resonance becomes slightly more prominent ($R_{min} \simeq 95\%$) and secondly that the reflectivity resonance frequency is independent on angle, as shown in Fig. 4.5. Last but not least, Fig. 4.6 shows that the spatial YZ field distribution for the defect band in the infinite photonic band gap crystal matches very well with the field pattern in the finite photonic band gap crystal slab. Therefore, from all three main observations (correlation, angle-independent reflectivity resonance, and spatial field distribution) we firmly identify the P1 defect band to occur at $\tilde{\omega}_i = 0.5140$ with a field distribution shown in Fig. 4.6.

The P2 defect band at $\tilde{\omega}_i = 0.5213$ in the infinite crystal (Fig. 4.2) shows in cross correlation (Fig. 4.3) with the finite crystal field distributions a constant correlation of about $C = 0.4$. At $\tilde{\omega} = 0.522$, the cross correlation has a maximum of $C = 1$ that agrees well with a weak reflectivity resonance at $\tilde{\omega} = 0.522$ at normal incidence (see Fig. 4.4 (b)). With increasing angle of incidence the reflectivity resonance deepens eventually to $R_{min} \simeq 30\%$. The reflectivity resonance is independent of incident angle (Fig. 4.5) as expected for a cavity resonance in a 3D band gap. Fig. 4.6 shows that the spatial field distribution in the infinite crystal defect band agrees very well with the field distribution in the finite crystal slab. We note on comparing that the P2 field distribution has some qualitative similarity with the P1 field distribution, which explains the occurrence of a secondary cross-correlation peak at $\tilde{\omega} = 0.514$ in Fig. 4.3. Therefore, we identify the P2 defect band to occur at $\tilde{\omega}_i = 0.522$ with a field distribution as shown in Fig. 4.6.
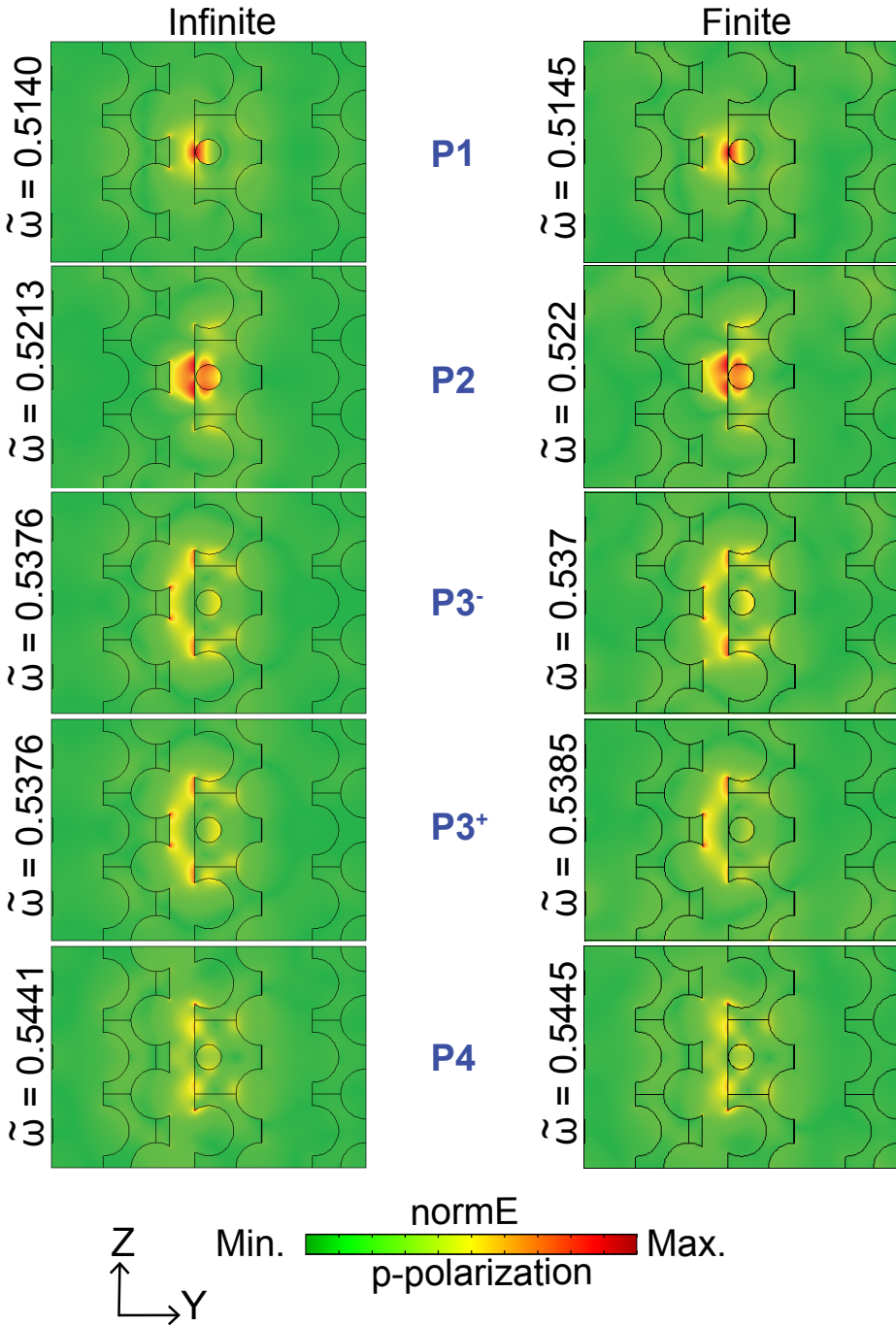
Figure 4.6: YZ cross sections of the electric-field distribution ($|E|$) of the P1, P2, P3$^-$, P3$^+$, and P4 resonances in the $3 \times 3 \times 3$ super cell of a 3D inverse woodpile photonic crystal with a point defect for $p-$polarized light at normal incidence.
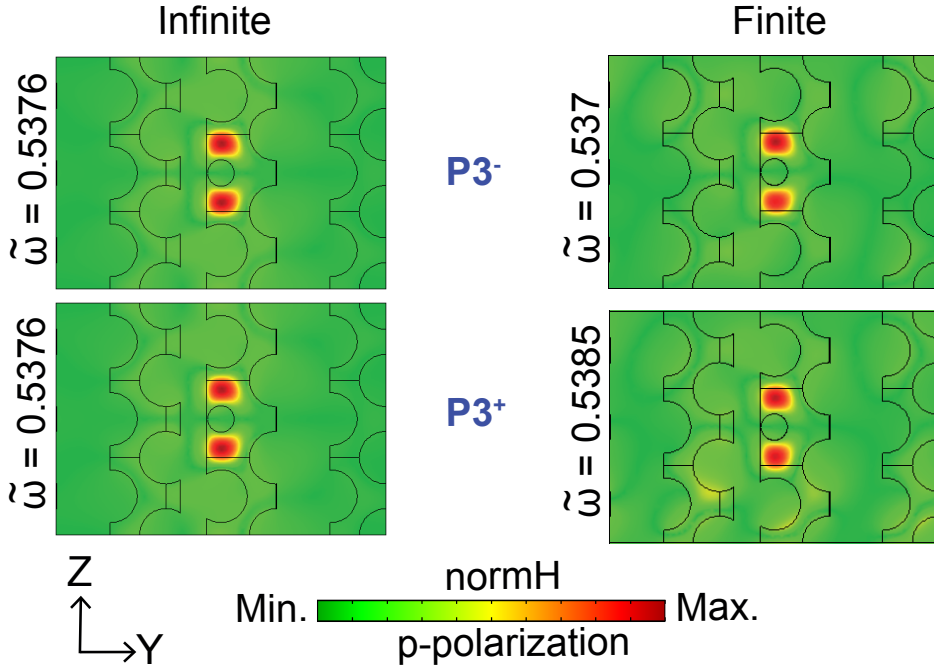
Figure 4.7: YZ cross sections of the magnetic-field distribution ($|H|$) of the P3$^-$ and P3$^+$ resonance in the $3 \times 3 \times 3$ super cell of a 3D inverse woodpile photonic crystal with a point defect for $p-$polarized light at normal incidence.

The cross correlation of the P4 defect band at $\tilde{\omega}_i = 0.5441$ in the infinite crystal (Fig. 4.2 (b)) with the finite crystal field distributions is a constant correlation of about $C = 0.3$ (Fig. 4.3). At $\tilde{\omega} = 0.5445$, the cross correlation has a maxima at $C = 1$ that agrees well with a strong reflectivity ($R_{min} \simeq 0\%$) resonance at $\tilde{\omega} = 0.5445$ at normal incidence (see Fig. 4.4 (b)). However, with increasing angle of incidence the reflectivity resonance changes to $R_{min} \simeq 70\%, 20\%$. Moreover, the reflectivity resonance is independent of incident angle (Fig. 4.5), which is expected for a cavity resonance in a 3D band gap. Finally, Fig. 4.6 shows that the spatial field distribution in the infinite crystal defect band agrees very well with the field distribution in the finite crystal slab. The comparison shows that P4 field distribution has some qualitative similarity with the P3 field distribution and hence a secondary cross-correlation peak appears at $\tilde{\omega} = 0.537$ and $\tilde{\omega} = 0.5385$ in Fig. 4.3. Therefore, we identify the P4 defect band to occur at $\tilde{\omega}_i = 0.5445$ with a field distribution as shown in Fig. 4.6.

The P3 defect band at $\tilde{\omega}_i = 0.5376$ in the infinite crystal reveals a double cross correlation peak at $\tilde{\omega}_- = 0.537$ and $\tilde{\omega}_+ = 0.5385$ (see Fig. 4.3). In reflectivity (Fig. 4.4 (b)) we observe two resonance troughs at $\tilde{\omega}_- = 0.537$ and $\tilde{\omega}_+ = 0.5385$. Both troughs develop deep minima ($R_{min} \simeq 20\%$) versus angle of incidence, but their resonance frequencies are independent of angle (Fig. 4.5), typical of photonic band gap cavity resonances. Moreover, we observe that these two troughs are
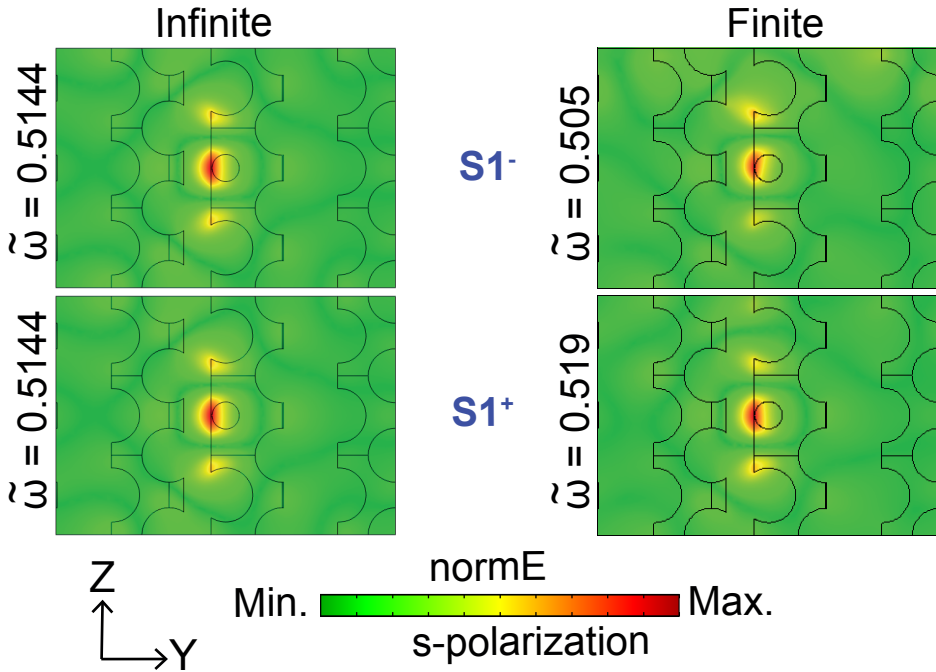
Figure 4.8: YZ cross sections of the electric-field distribution ($|E|$) of the S1$^-$ and S1$^+$ resonance in $3 \times 3 \times 3$ super cell of a 3D inverse woodpile photonic crystal with a point defect for $s-$polarized light at normal incidence.

symmetrically located on either sides of the defect band $\tilde{\omega}_i = 0.537$.

Fig. 4.6 shows that the spatial electric-field distribution of the P3 defect band matches very well with both field distributions at the lower ($\tilde{\omega}_- = 0.537$) and upper ($\tilde{\omega}_+ = 0.5385$) reflectivity resonances. Since the magnetic field is orthogonally related to the electric field for an electromagnetic wave [41], we compare their magnetic-field distributions and Fig. 4.7 shows that both field distributions at the reflectivity resonances match very well with the magnetic field of the P3 defect band, which confirms that both finite-size resonances derive from one and the same resonance in the infinite crystal.

Since the double reflectivity resonance is likely the result of a (currently) unknown coupling, it is uncertain whether the widths of either resonance can be attributed to a true resonance width and thus a quality factor. Nevertheless, we derive the bandwidths of P3$^-$ and P$^+$ reflectivity resonances as $\triangle\tilde{\omega}_- = 0.00053$ and $\triangle\tilde{\omega}_+ = 0.0005$.

The S1 defect band at $\tilde{\omega}_i = 0.5144$ in the infinite crystal also reveals a double cross correlation peak with $C = 1$ at $\tilde{\omega}_- = 0.505$ and $\tilde{\omega}_+ = 0.5190$ (the latter being remarkably broad). In reflectivity (Fig. 4.2 (a)) we observe two resonances at normal incidence, namely at $\tilde{\omega}_- = 0.505$ and $\tilde{\omega}_+ = 0.5190$, in good agreement with the cross correlations. With increasing angle of incidence the two resonances reveal remarkably different behavior. The upper resonance at $\tilde{\omega}_+ = 0.5190$ does

not shift with angle of incidence (Fig. 4.5), as expected for a photonic band gap cavity, even though its amplitude varies markedly. The lower resonance at $\tilde{\omega}_- = 0.505$ (at $\theta = 0°$) occurs at a frequency *outside* the photonic band gap, but inside the $s-$polarized stop band. Indeed the trough shifts with angle of incidence, since different troughs occur at $\theta = 40°$ or $\theta = 80°$. Moreover, we observe that these two troughs are asymmetrically located on either sides of the defect band $\tilde{\omega}_i = 0.5144$. This dispersive behavior is typical for a cavity resonance that is not fully confined in 3D, but lower dimensions, as in the case for instance of a Fabry-Pérot cavity (strictly only confined in 1D). At this time we do not yet have an explanation for the underlying physics of this remarkable behavior.

The S1 and P3 defect bands in the infinite crystal reveal more complicated behavior because we identify them to correspond to double resonances in the finite crystal reflectivity spectra. At this time we do not have an explanation for this behavior, only the general hypothesis that apparently the leaking of vacuum modes into the finite crystals seem to cause the splitting. But this statement does not explain why there would be a resonant structure in the vacuum that would couple to the defect bands ((instead if a broad vacuum continuum that might induce Fano resonances [42] (see Section 4.3.3 below for Fano resonances that appear below the band gap)).

We note that except S1$^-$ all other reflectivity resonances (S1$^+$, P1, P2, P3$^-$, P3$^+$ and P4) are inside the 3D photonic band gap for a perfect crystal and hence will provide a three-dimensional confinement of light. Therefore, we calculate the cavity quality factor Q [41] for these resonances using

$$Q = \frac{\tilde{\omega}_c}{\triangle\tilde{\omega}}, \tag{4.2}$$

with $\tilde{\omega}_c$ the central frequency and $\triangle\tilde{\omega}$ the full width at half maxima of the reflectivity resonance. However, Fig. 4.4 shows that the bandwidth $\triangle\tilde{\omega}$ is extremely small for the P1 and the P2 reflectivity resonances and hence report the minimum bound for their quality factors by using the employed frequency resolution $\delta\tilde{\omega} = 0.0005$. The bandwidths of reflectivity resonances S1$^-$, S1$^+$, P3$^-$, P3$^+$, and P4 are $\triangle\tilde{\omega} = 0.0011, 0.0020, 0.00053, 0.0005,$ and 0.0010, respectively, which corresponds to cavity quality factors shown in the top panel of Fig. 4.9. We note that P1 , P2, P3$^-$, P3$^+$ resonance have the highest cavity quality factors $Q \sim 1000$ and S1$^+$ resonance has the lowest quality factor $Q \sim 250$. This quality factor appears to be about 4 times greater than for a direct woodpile crystal with the same thickness of 12 layers [21].

4.3.2 Purcell factor and energy enhancement

Since an optical cavity creates an environment to spatially control the local density of states [43], the spontaneous emission rate of an emitter can be locally controlled [4, 28–31]. In order to find the increase in the spontaneous emission rate due to the cavity resonances, known as the Purcell effect [27], we calculate
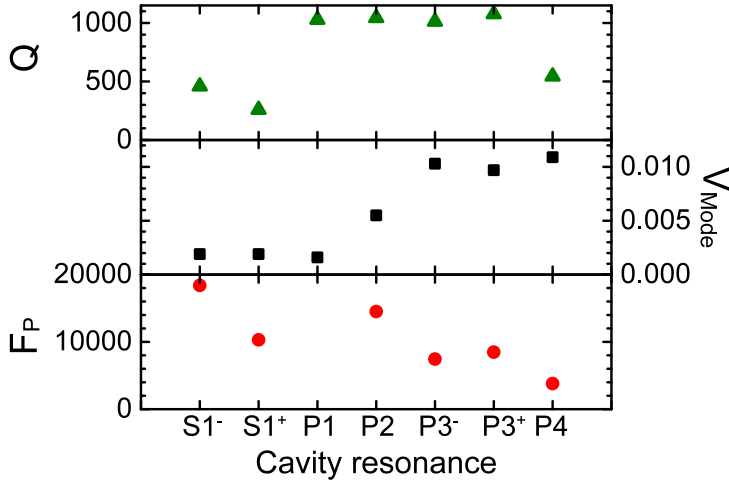
Figure 4.9: Top panel: quality factor Q, middle panel: mode volume V_{Mode} normalized to the cubed wavelength of each reflectivity resonance j: λ_j^3, and bottom panel: Purcell factor F_P normalized to $(\frac{\lambda_j}{n})^3$ with n the refractive index of a cavity medium. $S1^-$, $S1^+$, $P3^-$, $P3^+$, and P4 are reflectivity resonances. For the frequency resolution employed in the calculation, Q = 1000 represents the minimum bound of the quality factors for the P1 and the P2 reflectivity resonances. Additionally, the P1 resonance has the Purcell factor $F_P = 49987(\frac{1}{n})^3$.

the Purcell factor F_P given by

$$F_P = \frac{3}{4\pi^2}\frac{Q}{V_{Mode}}\left(\frac{1}{n}\right)^3, \tag{4.3}$$

with Q the cavity quality factor, V_{Mode} the mode volume normalized to cubed wavelength and n the refractive index of a cavity medium.

To determine the mode volume V_{Mode} [26, 44] normalized to the cubed wavelength of each reflectivity resonance j: λ_j^3, we employ the definition

$$V_{Mode} \equiv \frac{\int_V \epsilon(\vec{r})(|E|(\vec{r},\lambda_j))^2 dV}{\max_V\left(\epsilon(\vec{r})(|E|(\vec{r},\lambda_j))^2\right)}\left(\frac{1}{\lambda_j^3}\right), \tag{4.4}$$

with E the electric field and ϵ the dielectric permittivity. We choose the region to have a total volume $V = ac^2$ equal to one primitive unit cell of the cubic inverse woodpile photonic crystal.

The middle panel of Fig. 4.9 shows that the $P3^-$, $P3^+$, and P4 resonances have nearly equal mode volume $V_{Mode} = 0.01$, as observed by Ref. 26. We observe extremely small mode volumes for the $S1^-$ resonance ($V_{Mode} = 0.0019$), $S1^+$ resonance ($V_{Mode} = 0.0019$), P1 resonance ($V_{mode} = 0.0016$), and the P2 resonance ($V_{mode} = 0.0055$), which are significantly smaller than the mode volume $V_{mode} = 0.69$ reported by Ref. 45 for an L3 cavity in a 2D photonic crystal slab.

According to the calculations of Ref. 26, the P2 resonance was reported to have the smallest mode volume $V_{Mode} = 0.8$ that qualitatively supports our finding, however the numerical values are different, which we explain in the Appendix 4.D.

For a strong confinement of light by an optical cavity, a large quality factor and a small mode volume are desirable, which corresponds to a large Purcell factor. Therefore, with a known quality factor Q and mode volume V_{Mode}, we calculate the Purcell factor F_P normalized to $(\frac{\lambda_j}{n})^3$ using Eq. 4.3. The bottom panel of Fig. 4.9 reveals the highest Purcell factor $F_P = 14506(\frac{1}{n})^3$ for the P2 resonance (excluding S1$^-$ resonance, which is outside the band gap and P1 resonance, which does not show any reflectivity minimum at any incident angle). Hence, the P2 reflectivity resonance with $\tilde{\omega}_c = 0.522$ has the best potential for the spatial confinement of light in a very small mode volume, which agrees with the conclusion of Ref. 26 that the 3rd resonance is the best one for nanophotonic purposes.

Considering the electric-field distributions of Fig. 4.6 and Fig. 4.8, we note that the electric field is strongly concentrated in the proximal region of two orthogonal pores for all cavity resonances. However, we observe that the cavity resonances are localized in silicon as well as in air, $e.g.$, the S1$^+$ and P1 resonances have field maxima in silicon, whereas the P2 resonance has maxima in air as well as in silicon. Hence, our Purcell factor calculation cannot accurately determine the energy enhancement over the entire volume, given the strongly different refractive indices for air and silicon [44]. Therefore, to accurately quantify the energy enhancement η_E at a frequency ω in the reflectivity spectra with respect to the reference frequency ω_{ref}, we employ the definition

$$\eta_E \equiv \frac{\int_V \epsilon(\vec{r})(|E|(\vec{r}, \omega))^2 dV}{\int_V \epsilon(\vec{r})(|E|(\vec{r}, \omega_{\text{ref}}))^2 dV}. \tag{4.5}$$

with E the electric field, ϵ the dielectric permittivity, and a total volume $V = ac^2$ equal to one primitive unit cell of the cubic inverse woodpile photonic crystal. As references, we select either the incident light in vacuum, or a low frequency $\tilde{\omega} = 0.04$, which is a frequency unperturbed by the reflectivity resonances. Figure 4.10 shows the enhancement η_E between $\tilde{\omega} = 0.5$ and $\tilde{\omega} = 0.55$ for both polarizations. We observe significant energy enhancement at frequencies pertaining to the reflectivity resonances, $i.e.$, S1$^-$, S1$^+$, P3$^-$, P3$^+$, and P4, which confirms our results regarding the identification of these resonances. Moreover, the enhancement η_E for the S1$^+$ resonance is nearly equal to the one for the P2 resonance. We note that the enhancement is maximum for the P3$^-$, P3$^+$, and P4 resonances.

From calculations of the Purcell factor and the energy enhancement, we conclude for nanophotonic purposes that the P2 resonance is ideal for the confinement of light in a very small spatial volume, whereas the P3 and P4 resonances are suitable for the large energy enhancement over a large spatial volume.
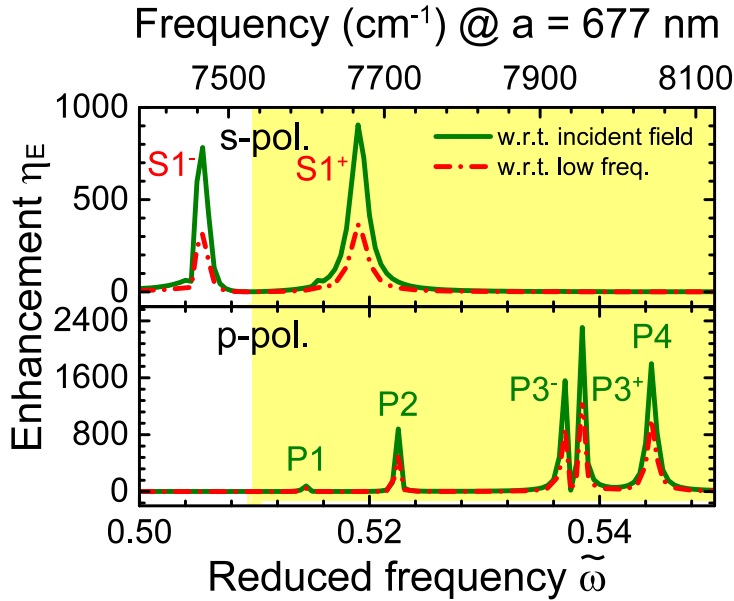
Figure 4.10: Energy enhancement for a 3D inverse woodpile photonic crystal with a point defect. Red dashed-dotted curves represent the enhancement with respect to a frequency below the 3D band gap of a perfect crystal. Green solid curves represent the enhancement with respect to the incident light. Here, S1$^-$, S1$^+$, P3$^-$, P3$^+$, and P4 are reflectivity resonances.

4.3.3 Fano resonances below the 3D band gap

The reflectivity spectra for a perfect 3D inverse woodpile photonic crystal reveal Fabry-Pérot fringes below the stop band as a result of interference between the front and back surfaces [37]. To investigate the effect of a point defect on these Fabry-Pérot fringes, we calculate the polarization-resolved (s or p) reflectivity below $\tilde{\omega} = 0.50$ at normal incidence to the $3 \times 3 \times 3$ supercell of an inverse woodpile photonic crystal with and without a point defect. We observe below $\tilde{\omega} = 0.21$ in Fig. 4.11 that the spectra for a photonic crystal with defect matches very well with the one for a perfect photonic crystal. Beyond $\tilde{\omega} = 0.21$, several sharp peaks appear in the spectra for a photonic crystal with a point defect. These peaks are narrow and sometimes have a reflectivity near 100%. The band structure in Fig. 4.11 (ii) reveals that the bands are linearly increasing till $\tilde{\omega} = 0.12$ and then linearly decreasing till $\tilde{\omega} = 0.21$. Beyond $\tilde{\omega} = 0.21$, the band folding occurs, since the calculations were performed for a supercell. By comparing this band structure to the corresponding reflectivity spectra, we note that fringes for a photonic crystal with defect match with the fringes for a perfect crystal only till the bands are in linear regime, *i.e.*, below $\tilde{\omega} = 0.21$. Therefore, these sharp and narrow peaks in the fringes correspond to frequency range of the band folding.

In order to verify the localization of these peaks in real space, we investigate
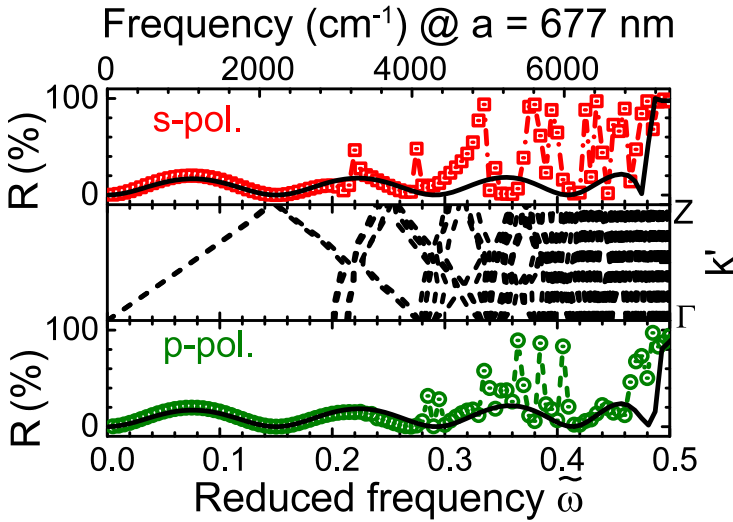
Figure 4.11: Reflectivity below the 3D band gap for a 3D inverse woodpile photonic crystal with a point defect. The red curve in (i) and the green curve in (iii) are reflectivity spectra calculated at normal incidence for s and p polarizations, respectively. The corresponding band structure for the ΓZ direction is shown in (ii), which is calculated by MPB PWE solver. Panel (ii) also illustrates the band folding due to supercell calculations. The wave vector is expressed as $k^{'} = (ka/2\pi)$. Black curves in (i) and (iii) indicate the reflectivity spectra for a perfect 3D inverse woodpile photonic crystal for s and p polarization, respectively. Near $\tilde{\omega} = 0.21$, the reflectivity spectra for a crystal with defect starts deviating from the one for a perfect crystal.

their angle-dependency. Figure 4.12 shows the reflectivity for a photonic crystal with a point defect between $\tilde{\omega} = 0.21$ and $\tilde{\omega} = 0.5$ at incident angles $0°$ and $40°$. We observe that there are peaks perturbing the Fabry-Pérot fringes for both incident angles. However, most of these peaks vary with incident angle. Therefore at this point, we consider that these peaks are angle-dependent, unlike the cavity resonances in Section 4.3.1.

To understand the origin of these peaks, we simplify the problem to study a homogeneous film. We consider a $L = 3c$ thin silicon film with two orthogonal defect pores at the center, which is similar to the computational cell of an inverse woodpile with a point defect. Figure 4.13 shows the reflectivity spectra for a thin film without and with two orthogonal defect pores. We observe Fabry-Pérot fringes below $\tilde{\omega} = 0.4$, which are due to the continuum contribution from the two interfaces of the thin film. The reflectivity spectrum for a thin film with two orthogonal defect pores of radii $r^{'} = 0.12a$ reveals several peaks and troughs at discrete frequencies, e.g., a trough at $\tilde{\omega} = 0.18$ and a peak at $\tilde{\omega} = 0.27$. We note that a trough always occurs near the maxima and a peak always near the minima of a Fabry-Pérot fringe. Increasing radii of these defect pores changes amplitudes of existing peaks and troughs and new ones appear as well. We surmise this behavior as the electromagnetic interference of reflectivity from the
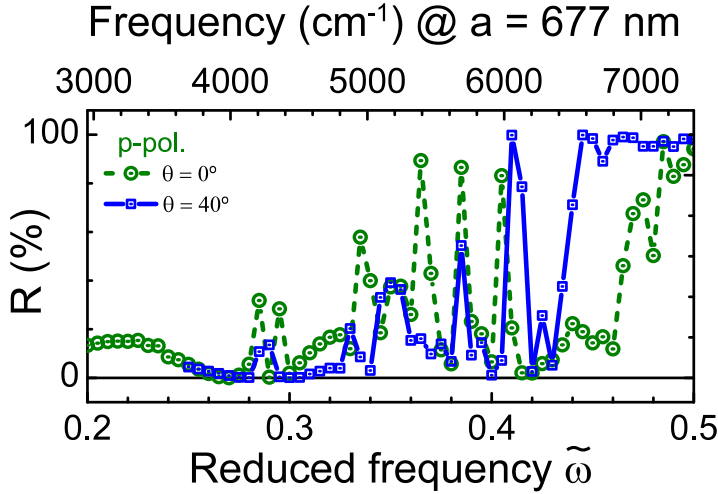
Figure 4.12: Reflectivity below the 3D band gap for a 3D inverse woodpile photonic crystal with a point defect for *p*-polarized incident light. The green dashed and blue solid curves are the spectra for incident angles $\theta = 0°$ and $\theta = 40°$, respectively, off the normal in the ΓZ direction.

continuum contribution of the film and from the discrete contribution of the defect pores. This interference leads to sharp resonances, commonly referred as Fano resonances in solid-state and atomic physics [42, 46].

After understanding the origin of Fano resonances due to two orthogonal defect pores in a thin film, we now investigate these two orthogonal defect pores in an inverse woodpile. The incident plane wave is reflected from the photonic crystal for all frequencies and gets coupled to the resonant cavity only at discrete frequencies [46, 47]. Therefore, the electromagnetic interference between the continuum contribution of the light reflected by the photonic crystal and the discrete contribution of the cavity resonance gives rise to a Fano resonance [42, 47], *e.g.*, at $\tilde{\omega} = 0.22$ in the *s* polarization spectrum in Fig. 4.11. When the continuum contribution and the discrete contribution to the interference are comparable, the Fano resonance has a characteristic sharp asymmetrical shape, *e.g.*, at $\tilde{\omega} = 0.315$ for *s* polarization and at $\tilde{\omega} = 0.365$ for *p* polarization in Fig. 4.11. Hence, these Fano resonances are angle-dependent and sometimes asymmetrical in shape unlike the cavity resonances, which are angle-independent and symmetrical in shape.

4.3.4 Resonant cavities for photovoltaic efficiency enhancement

To benefit from the large energy enhancement at the reflectivity resonances, we investigate the possibility of using a 3D silicon inverse woodpile with a resonant cavity as an absorbing medium of a solar cell. In order to make our calculations relevant to experimental studies, we use a wavelength-dependent complex refractive index of silicon obtained from Ref. 48, which was previously used in
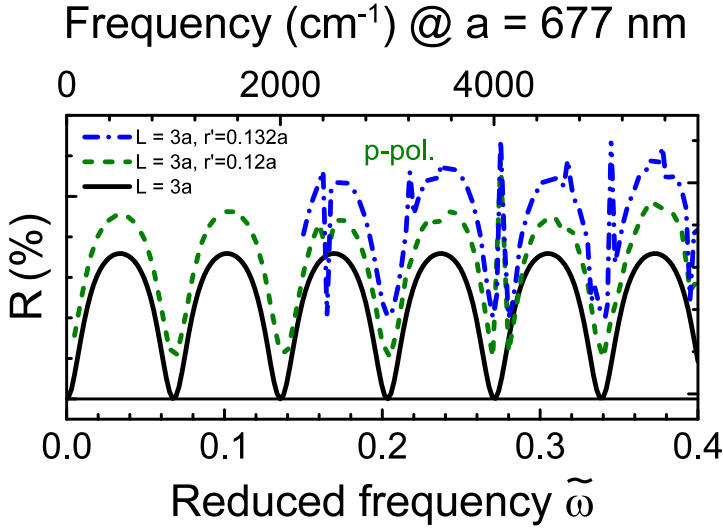
Figure 4.13: Calculated reflectivity spectra for a thin dielectric film with thickness $L = 3a$ for p polarization. The film has dielectric permittivity $\epsilon = 12.1$. The black curve shows the reflectivity spectrum for a perfect thin film. Green dashed and blue dashed-dotted curves represent the reflectivity spectra for a thin film with two orthogonal defect pores of radii $r' = 0.12a$ and $r' = 0.132a$, respectively. To compare spectra for different defect-pore radii, we use ordinate offsets of 20% and 40% in green dashed and blue dashed-dotted curves, respectively.

Chapter 3. Chapter 3 reported that the thin silicon film absorbs weakly in the wavelength range from 600 to 1000 nm. To enhance the absorption in this range, we tailor the lattice parameters of the inverse woodpile to be $a = 425$ nm and $c = 300$ nm (same as previously used in Chapter 3), such that the reflectivity resonances are between $\lambda = 600$ and $\lambda = 1000$ nm.

To build up on the identification results of the reflectivity resonance troughs in Section 4.3.1, we compare the reflectivity spectra in the top panels of Figs. 4.14 (a) and (b) with and without imaginary part of the silicon refractive index. We observe between $\tilde{\omega} = 0.45$ and $\tilde{\omega} = 0.70$ in the spectra that there are more reflectivity troughs with absorption than without absorption for both polarizations, which implies that absorption gives rise to additional resonances. We also note that only few of the troughs for spectra without absorption match with the troughs with absorption, e.g., at $\tilde{\omega} = 0.49$ and $\tilde{\omega}_c = 0.59$ for s polarization, and at $\tilde{\omega}_c = 0.52$ for p polarization. To ascertain whether these troughs are indeed reflectivity resonances, one need to follow the complete procedure depicted in Section 4.3.1. Currently, we surmise that reflectivity resonances in the visible regime differ in number from the ones in the infrared regime.

As a first step to investigate photovoltaic efficiency of the 3D inverse woodpile photonic crystal, we calculate the absorption spectra, as shown in the bottom panels of Figs. 4.14 (a) and (b). We compare the absorption by a thin inverse
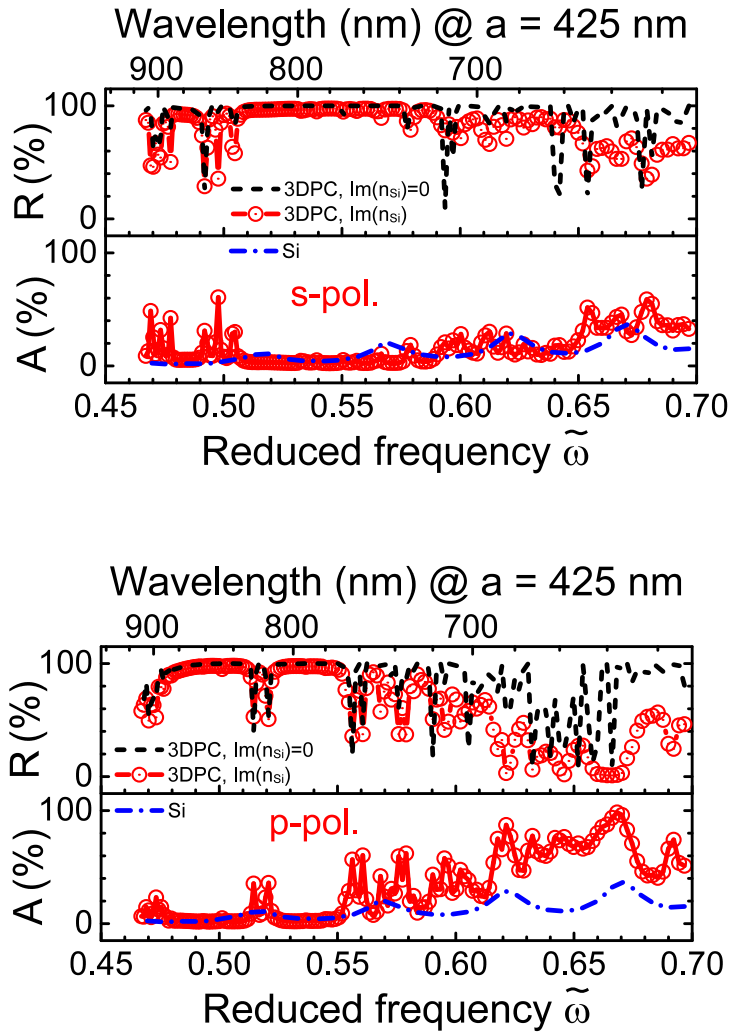
Figure 4.14: Reflectivity and absorption spectra calculated for a 3D inverse woodpile photonic crystal with a point defect in the visible regime at normal incidence in the ΓZ direction. The high-index backbone has complex refractive index, which includes dispersion and absorption. Top panel: Black curves are the reflectivity spectra for an inverse woodpile photonic crystal, with dispersion but no absorption ($\mathbb{I}m(n_{Si}) = 0$). Red curves are results for an inverse woodpile photonic crystal, with dispersion and absorption ($\mathbb{I}m(n_{Si}) \neq 0$). Bottom panel: Red curves are the absorption spectra for an inverse woodpile photonic crystal, with dispersion and absorption ($\mathbb{I}m(n_{Si}) \neq 0$). Blue curves are results for a thin silicon film.

woodpile with thickness $L_{3DPC} = 3c = 900$ nm to the absorption by a thin silicon film of equal thickness $L_{Si} = 3c$. We observe that at frequencies corresponding to the troughs in the reflectivity spectra, an inverse woodpile has multiple times higher absorption than a thin film, *e.g.*, at $\tilde{\omega} = 0.49$ for s polarization and at $\tilde{\omega} = 0.52$ for p polarization. Hence, a 3D inverse woodpile photonic crystal with a resonant cavity is an interesting candidate for the absorbing medium of a solar cell in order to enhance the photovoltaic efficiency at multiple discrete frequencies in the visible regime. We note that the absorption by an inverse woodpile is significantly higher for p polarization than for s polarization.

To understand this difference, we consider the number of troughs in the reflectivity spectra for both polarizations. We note that the p-polarized reflectivity spectrum has higher number of troughs between $\tilde{\omega} = 0.60$ and $\tilde{\omega} = 0.65$ than the s-polarized reflectivity spectrum. Therefore, an aggregate contribution of these large number of reflectivity troughs significantly enhances the absorption by an inverse woodpile in the case of p polarization.

Interestingly, a 3D inverse woodpile photonic crystal contains silicon by only 20% volume fraction (see Fig. 1.2 of Chapter 1) and hence is extremely lightweight compared to a bulk silicon of comparable thickness. However, the photocurrent density depends on the absorption as well as the surface recombination. Since an inverse woodpile has a large surface area per unit cell compared to a thin film, the surface recombination factor has to be deducted before reporting the final photovoltaic efficiency.

4.4 Conclusion

We have studied numerically the reflectivity and the absorption of a resonant cavity in a three-dimensional photonic crystal with finite support. The point defect acting as a cavity is formed in the proximal region of two orthogonal pores with a radius that differs from the ones in the bulk of the crystal. We employed the finite element method to study crystals with the cubic diamondlike inverse woodpile structure with a high-index backbone having a dielectric function similar to silicon. By comparing defect bands in the band structure for an infinite crystal and troughs in the reflectivity spectra for a finite crystal, we identify cavity resonances and their field patterns. Out of five observed cavity resonances, one is s-polarized and four are p-polarized. These cavity resonances are angle-independent, indicating a strong confinement of light in the crystal slab. The P1, P2, and P4 resonances reveal normal behavior with single cross-correlation peaks (between field distributions) and single reflectivity resonances. The P3 and S1 resonances in finite crystals reveal an intriguing splitting into 2 sub-resonances, for which we have currently no explanation.

We find that the P3 resonance at $\tilde{\omega} = 0.522$ is ideal for the confinement of light in a very small spatial volume around 0.0055 cubic wavelengths. We find large energy enhancement at cavity resonances, *i.e.*, up to $\eta_E = 2400$ times the incident energy and up to $\eta_E = 1200$ times the energy at a lower frequency. Fano resonances are observed below the band gap due to the electromagnetic
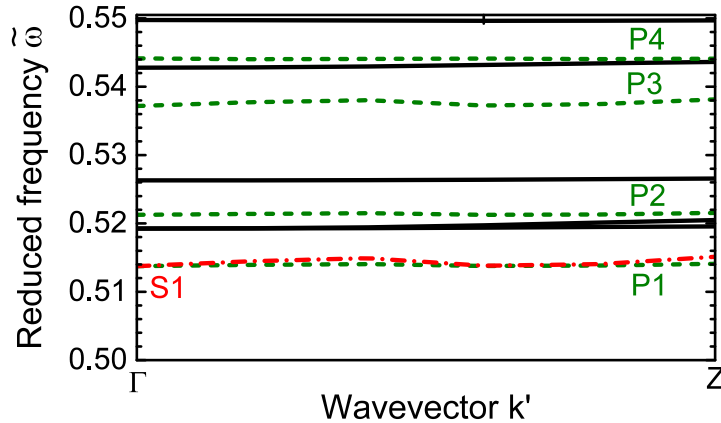
Figure 4.15: Comparison between the band structures in the ΓZ direction calculated using the COMSOL finite-element method (FEM) solver and the MPB plane-wave expansion (PWE) method. The band structure pertains to a 3D silicon inverse woodpile photonic crystal with two orthogonal defect pores with pore radius $\frac{r}{a} = 0.24$, defect pore radius $r' = 0.5r$ and $\epsilon_{Si} = 12.1$, using a $3 \times 3 \times 3$ supercell. Black lines are calculated by the MPB PWE solver. Red dashed-dotted line and green dashed lines are calculated by the COMSOL FEM solver. The wave vector is expressed as $k' = (ka/2\pi)$. Due to higher spatial resolution, the bands calculated by FEM solver are shifted to lower frequencies when compared to the bands calculated by the MPB solver. Upto five isolated and nearly dispersionless bands appear within the 3D photonic band gap and appear to confine light as cavity resonances. Thus, S1 indicates the single s-polarized cavity resonance inside the photonic band gap. Similarly, P1, P2, P3, and P4 indicate the four p-polarized cavity resonances inside the photonic band gap.

interference between the discrete contribution of the fundamental cavity mode and the continuum contribution of the light scattered by the photonic crystal. Our results indicate that 3D photonic band gap crystals with resonant cavities are potential candidates for the absorbing medium of a solar cell in order to enhance the photovoltaic efficiency and reduce the weight of the solar cell by nearly 80%. Consequently, our analysis of the resonant cavity provides a novel insight in understanding various resonances appearing due to locally disrupted lattice symmetry in 3D periodic photonic nanostructures.

4.A Photonic band structure calculations

To compute the photonic band structure for the supercell of a 3D inverse wood-pile photonic crystal with a point defect, Ref. 26 employs a plane-wave expansion (PWE) method eigenvalue solver, whereas we employ the COMSOL finite-element method (FEM) [35] eigenvalue solver [32]. We compute the polarization-resolved (both s and p) band structures. Figure 4.15 shows the bands between
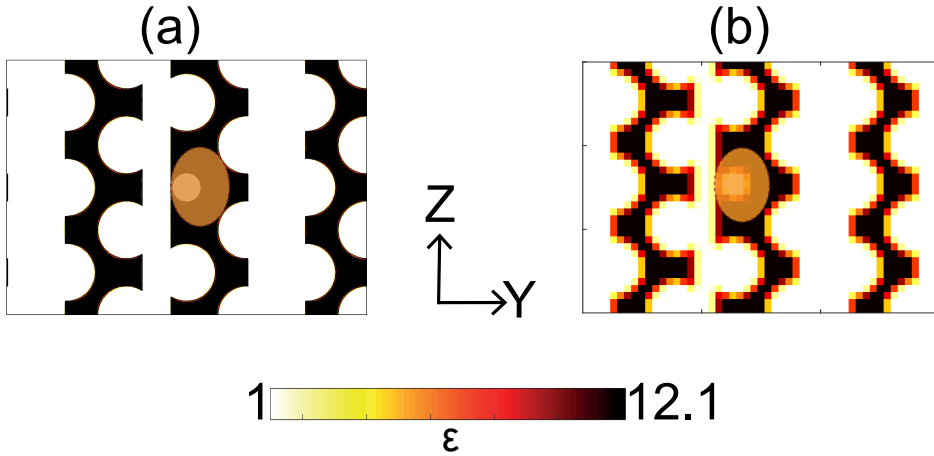
Figure 4.16: Cross sections of the dielectric-permittivity distribution (ϵ) along the YZ plane of the $3 \times 3 \times 3$ super cell of a 3D inverse woodpile photonic crystal with a point defect, using (a) COMSOL finite-element method and (b) MPB plane-wave expansion method with a grid resolution of $24 \times 34 \times 24$. The black color represents the high-index backbone of the crystal having dielectric function similar to silicon. The white color represents air. Two orthogonal defect pores result in a region with an excess of high-index backbone, indicated by brown color ellipses.

$\tilde{\omega} = 0.51$ and $\tilde{\omega} = 0.56$ obtained using both the FEM solver and the PWE method. We observe that there are five isolated and nearly dispersionless bands obtained using both methods. Out of these five bands, the FEM solver gives one s-polarized band, namely S1, and four p-polarized bands, namely P1, P2, P3, and P4. We note that all bands obtained using the FEM occur at lower frequencies compared to the corresponding bands obtained using the PWE method.

In order to characterize this frequency shift between the FEM and the PWE results, we compare cross sections of the dielectric-permittivity distribution of the supercell structure obtained from both methods in Fig. 4.16. We take the cross section through the center of the cavity and parallel to the YZ plane. We observe that the curved boundaries between the air and the high-index backbone material are smoother in Fig. 4.16 (a) compared to Fig. 4.16 (b). This difference is more pronounced for the sharp interface surrounding the point defect. Compared to the PWE solver, we use a smaller element size in the FEM solver to subdivide the computational domain and hence the sharp interfaces and the curved boundaries are better approximated. Ref. 26 also reports in Appendix A that the resonance bands shift to lower frequencies with a higher spatial resolution. Therefore, we conclude that the frequency shift between the bands obtained using the two numerical methods is due to the differences in the spatial resolution, resulting into different dielectric-permittivity distributions.

The computational time using the FEM solver is 2 times longer than the PWE method. In order to minimize the computational time, we subdivide the fre-

quency regime into two ranges: below the 3D band gap and the 3D band gap. Since there are no isolated resonance bands below the 3D band gap, we do not need the calculation to have the FEM spatial resolution. Hence, we employ the faster option of the PWE method to calculate the photonic band structure below the band gap. However, we employ a spatial resolution of $24 \times 34 \times 24$, which is a $2 \times 2 \times 2$ times greater 3D spatial resolution than in Ref. 26. Since we explicitly aim at identifying isolated cavity resonances, we compute the photonic band structure inside the 3D band gap using the FEM solver, which is the same numerical method used for the reflectivity calculations.

4.B   Mesh convergence

We are using tetrahedra to subdivide the 3D computational domain in the finite element method. To determine the edge length of the tetrahedra to completely mesh the complex geometry, we investigate the mesh convergence of the reflectivity results. We perform reflectivity calculations using upper limits of $\triangle l \leqslant \frac{\lambda_0}{4\sqrt{\epsilon}}$, $\triangle l \leqslant \frac{\lambda_0}{8\sqrt{\epsilon}}$, and $\triangle l \leqslant \frac{\lambda_0}{12\sqrt{\epsilon}}$ to the edge length $\triangle l$ on any tetrahedra, with λ_0 the shortest wavelength of the incident plane waves in vacuum. Figure 4.17 shows the reflectivity at frequencies below, inside, and near the upper edge of the 3D band gap. These reflectivity values change less than $\sim 0.1\%$ with the maximum edge length. From the nearly constant results of these three mesh resolutions, we conclude the quantitative convergence of our calculated reflectivity spectra. These three mesh resolutions take 4301 s, 5330 s, and 11017 s on the Serendipity cluster [39]. In order to minimize the computational time for a large number of frequencies, while maintaining the quantitative convergence of the results, we decided to choose an upper limit of $\triangle l \leqslant \frac{\lambda_0}{8\sqrt{\epsilon}}$ to the edge length of any tetrahedra used in the finite-element mesh.

4.C   Frequency convergence

The reflectivity troughs corresponding to the cavity resonances have bandwidths as narrow as $\triangle \tilde{\omega} = 0.0005$. Thus, a calculation performed for an insufficient number of discrete frequencies will not detect these reflectivity resonances. Moreover, the calculation may not show the actual minima of a given trough due to saturation. Therefore, we perform the frequency convergence analysis to determine the appropriate frequency resolution to detect these resonance troughs. We define the frequency resolution as the spacing between two adjacent frequencies. We choose three frequency regimes: between $\tilde{\omega} = 0.30$ and $\tilde{\omega} = 0.35$ below the band gap, between $\tilde{\omega} = 0.53$ and $\tilde{\omega} = 0.54$ inside the band gap, and between $\tilde{\omega} = 0.58$ and $\tilde{\omega} = 0.59$ near the upper edge of the band gap.

Figure 4.18 (a) shows the reflectivity spectra between $\tilde{\omega} = 0.30$ and $\tilde{\omega} = 0.35$ below the band gap. A comparison between the spectra for a perfect inverse woodpile and an inverse woodpile with a point defect reveals the Fano resonance at $\tilde{\omega} = 0.335$, as previously shown in Section 4.3.3. We observe that the maxima
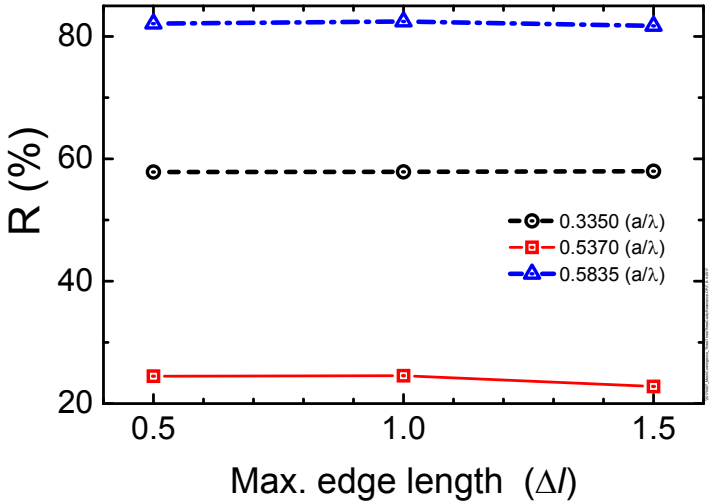
Figure 4.17: Mesh convergence analysis of the finite-element method for the calculation of reflectivity spectra for a 3D inverse woodpile photonic crystal with a point defect. Tetrahedra are used as basic elements. An upper limit of $\triangle l \leqslant \frac{\lambda_0}{8\sqrt{\epsilon}}$ is imposed to the edge length $\triangle l$ on any tetrahedra, with λ_0 the shortest wavelength of the incident plane waves in vacuum. Black circles and blue triangles pertain to frequencies below and near the upper edge of the 3D band gap, respectively. Red squares denote the frequency at the P3 cavity resonance. Black dashed, blue dashed-dotted, and red solid curves are guides to the eye showing modulations in the reflectivity with the varying edge length of a tetrahedron.

of this Fano resonance enhances with the frequency resolution. Also, there is a new Fano resonance appearing at $\tilde{\omega} = 0.335$ at the higher frequency resolution. Since we performed calculations using $\delta\tilde{\omega} = 0.005$ for the frequency range below the 3D band gap, there could be more Fano resonances than the ones shown in Fig. 4.11.

Figure 4.18 (b) shows the reflectivity spectra between $\tilde{\omega} = 0.53$ and $\tilde{\omega} = 0.54$ inside the band gap. We observe that P3 cavity resonance troughs with $\tilde{\omega} = 0.536$ and with $\tilde{\omega} = 0.538$ are detected only at frequency resolutions $\delta\tilde{\omega} = 0.0005$ and 0.0001. Since we employed a frequency resolution $\delta\tilde{\omega} = 0.0005$ for all calculations inside the 3D band gap, we have successfully detected all possible troughs. However, we note that the minima of the trough with $\tilde{\omega} = 0.536$ changes around 25% after increasing the frequency resolution by 5 times. Therefore, the detected cavity resonances can show even lower reflectivity at a higher frequency resolution than our calculations.

Figure 4.18 (c) shows the reflectivity spectra between $\tilde{\omega} = 0.582$ and $\tilde{\omega} = 0.591$ near the upper edge of the band gap. We see two troughs at $\tilde{\omega} = 0.583$ and $\tilde{\omega} = 0.588$ for an inverse woodpile with a point defect. We observe that the trough at $\tilde{\omega} = 0.583$ is invariant with the frequency resolution, whereas the minima value for the trough at $\tilde{\omega} = 0.588$ changes. We surmise that the trough
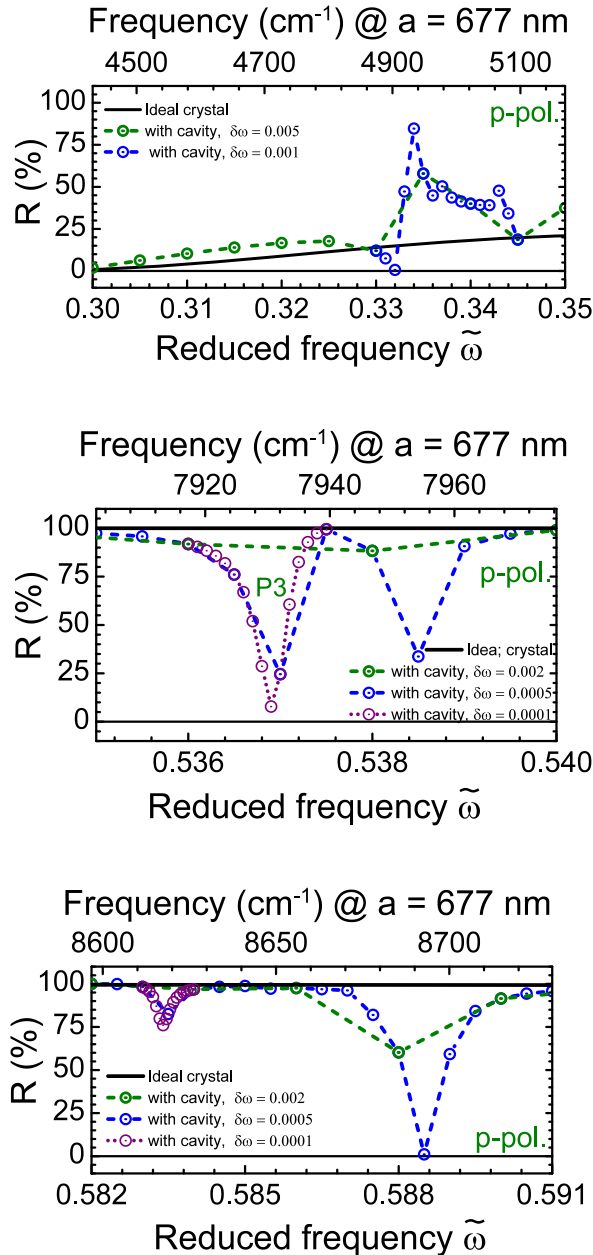
Figure 4.18: Frequency-resolved reflectivity spectra for a 3D inverse woodpile photonic crystal with a point defect for *p*-polarized light at normal incidence in the ΓZ direction. (a) Fano resonance below the band gap, (b) P3 cavity resonance inside the band gap, and (c) resonance near the upper edge of the band gap. Green dashed, blue dashed, and purple dashed curves are results calculated for the photonic crystal with defect for frequency resolutions $\delta\tilde{\omega} = 0.002$, 0.0005, and 0.0001, respectively. The black solid line indicates the reflectivity for an ideal crystal.

at $\tilde{\omega} = 0.583$ is a numerical speckle due to the finite sized calculations and the trough at $\tilde{\omega} = 0.588$ corresponds to one of the resonance bands near the upper edge of the band gap.

4.D Mode volume

Our calculated mode volume for the P2 reflectivity resonance $V_{\mathrm{mode}} = 0.0055$ is nearly **145** times smaller than the mode volume $V_{\mathrm{mode}} = 0.8$ reported by Ref. 26. In order to characterize this significant difference, we first investigate the number of degrees of freedom employed in Ref. 26 and in our calculations. For a $3 \times 3 \times 3$ supercell calculation by the PWE solver in Ref. 26, the number of degrees of freedom equals the 3D spatial resolution ($36 \times 51 \times 36$) times the number of dependent variables (2 field components) [22, 32], and hence $N_f = 36 \times 51 \times 36 \times 2 = 132192$. In our FEM results, the employed number of degrees of freedom is $N_f = 11073944$, which is nearly **84** times larger than the one in Ref. 26. Moreover, the field patterns for resonances in Fig. 4.6 and Fig. 4.8 reveal that the field maxima always occur near the sharp boundaries and the curved boundaries, which are accurately approximated using the FEM solver (see Fig. 4.16 and Appendix 4.A). Therefore, we conclude that these two main observations (larger number of degrees of freedom and better approximated field maxima) qualitatively explain the underlying numerical factor leading to different mode volumes.

Theoretically, the mode volume calculates the spatial confinement of light in a single cavity mode. However, the mode volume calculation in Eq. 4.4 employs integration over a volume V, which is not precisely defined for an open system and extending the volume over the entire space leads to the divergence of the integral [53, 54]. Moreover, it is extreme challenging for the experimental studies to relate with the maximum mode volume for a cavity resonance. Therefore, we calculate the average mode volume V'_{Mode} normalized to the cubed vacuum wavelength of each reflectivity resonance j: λ_j^3 by employing the definition

$$V'_{Mode} \equiv \frac{\int_V \epsilon(\vec{r})(|E|\,(\vec{r}, \lambda_j))^2 dV}{\mathrm{avg}_V\left(\epsilon(\vec{r})(|E|\,(\vec{r}, \lambda_j))^2\right)}\left(\frac{1}{\lambda_j^3}\right), \qquad (4.6)$$

with E the electric field and ϵ the dielectric permittivity. We choose the region to have a total volume $V = ac^2$ equal to one primitive unit cell of a cubic inverse woodpile photonic crystal.

The middle panel of Fig. 4.19 shows that P3$^-$, P3$^+$, and P4 resonances have nearly equal average mode volume $V'_{Mode} = 2.20$, which is nearly 220 times bigger than their corresponding maximum mode volume $V_{Mode} = 0.010$ observed in Fig. 4.9. The average mode volumes for S1$^-$, S1$^+$, P1, and P2 resonances are nearly 1000 times bigger than their maximum mode volumes V_{Mode}. Furthermore, we calculate the Purcell factor F_P normalized to $(\frac{\lambda_j}{n})^3$ using Eq. 4.3 for average mode volumes V'_{Mode}. The bottom panel of Fig. 4.19 reveals Purcell factors F_P between 10 and 50 for all the reflectivity resonances, which are nearly
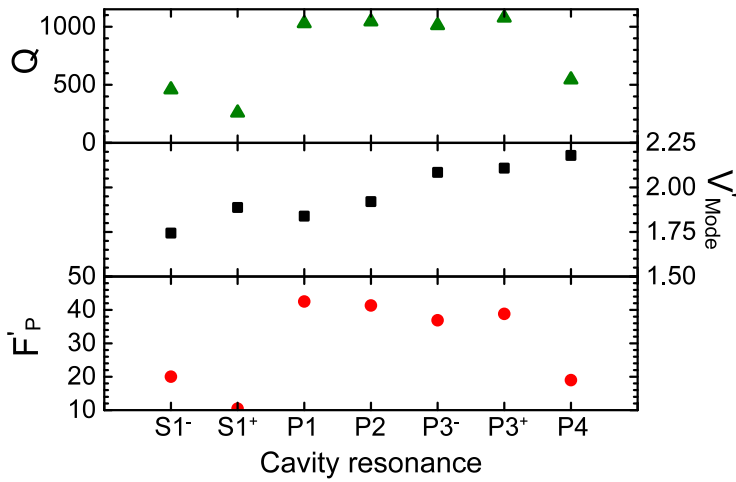
Figure 4.19: Top panel: quality factor Q, middle panel: Average mode volume V'_{Mode} normalized to the cubed wavelength of each reflectivity resonance j: λ_j^3, and bottom panel: Purcell factor F'_P normalized to $(\frac{\lambda_j}{n})^3$ with n the refractive index of a cavity medium. $S1^-$, $S1^+$, $P3^-$, $P3^+$, and P4 are reflectivity resonances. For the frequency resolution employed in the calculation, Q $=$ 1000 represents the minimum bound of the quality factors for the P1 and P2 reflectivity resonances.

1000 times smaller than Purcell factors observed in the bottom panel of Fig. 4.9 for the maximum mode volume. Although the average mode volume and Purcell factor are quantitatively smaller than the corresponding maximum values, qualitatively they will eradicate the possibility of imprecise calculation due to integral divergence as well as will give a fair comparison to the experimental studies.

Bibliography

[1] K. J. Vahala, "Optical microcavities," Nature (London) **424**, 839 (2003). 83

[2] L. Novotny and B. Hecht, *"Principles of nano-optics,"* (Cambridge University Press, Cambridge, 2006). 83

[3] E. Krioukov, D. J. W. Klunder, A. Driessen, J. Greve, and C. Otto, "Sensor based on an integrated optical microcavity," Opt. Lett. **27**, 512 (2002). 83

[4] J. M. Gérard, B. Sermage, B. Gayral, B. Legrand, E. Costard, and V. Thierry-Mieg, "Enhanced spontaneous emission by quantum boxes in a monolithic optical microcavity," Phys. Rev. Lett. **81**, 1110 (1998). 83, 84, 94

[5] J. P. Reithmaier, G. Sęk, A. Löffler, C. Hoffmann, S. Kuhn, S. Reitzenstein, L. V. Keldysh, V. D. Kulakovskii, T. L. Reinecke, and A. Forchel, "Strong coupling in a single quantum dot-semiconductor microcavity system," Nature (London) **432**, 197 (2004). 83

[6] T. Yoshie, A. Scherer, J. Hendrickson, G. Khitrova, H. M. Gibbs, G. Rupper, C. Ell, O. B. Shchekin, and D. G. Deppe, "Vacuum Rabi splitting with a single quantum dot in a photonic crystal nanocavity," Nature (London) **432**, 200 (2004). 83

[7] E. Peter, P. Senellart, D. Martrou, A. Lemaître, J. Hours, J. M. Gérard, and J. Bloch, "Exciton-photon strong-coupling regime for a single quantum dot embedded in a microcavity," Phys. Rev. Lett. **95**, 067401 (2005). 83

[8] M. L. Gorodetsky, A. A. Savchenkov, and V. S. Ilchenko, "Ultimate Q of optical microsphere resonators," Opt. Lett. **21**, 453 (1996). 83

[9] D. W. Vernooy, V. S. Ilchenko, H. Mabuchi, E.W. Streed, and H. J. Kimble, "High-Q measurements of fused-silica microspheres in the near infrared," Opt. Lett. **23**, 247 (1998). 83

[10] M. Pelton, J. Vučkovíc, G. S. Solomon, A. Scherer, and Y. Yamamoto, "Three-dimensionally confined modes in micropost microcavities: quality factors and Purcell factors," IEEE J. Quantum Electron. **38**, 170 (2002). 83

[11] H. T. Miyazaki and Y. Kurokawa, "Squeezing visible light waves into a 3-nm-thick and 55-nm-long plasmon cavity," Phys. Rev. Lett. **96**, 097401 (2006). 83

[12] M. Kuttge, F. J. G. de Abajo, and A.Polman, "Ultrasmall mode volume plasmonic nanodisk resonators," Nano Lett. **10**, 1537 (2010). 83

[13] D. K. Armani, T. J. Kippenberg, S. M. Spillane, and K. J. Vahala, "Ultra-high-Q toroid microcavity on a chip," Nature (London) **421**, 925 (2003). 83

[14] B. Gayral, J. M. Gérard, A. Lemaître, C. Dupuis, L. Manin, and J. L. Pelouard, "High-Q wet-etched GaAs microdisks containing InAs quantum boxes," Appl. Phys. Lett. **75**, 1908 (1999). 83

[15] D. Englund, D. Fattal, E. Waks, G. Solomon, B. Zhang, T. Na- kaoka, Y. Arakawa, Y. Yamamoto, and J. Vučkovíc, "Controlling the spontaneous emission rate of single quantum dots in a two-dimensional photonic crystal," Phys. Rev. Lett. **95**, 013904 (2005). 83

[16] P. Velha, E. Picard, T. Charvolin, E. Hadji, J. Rodier, P. Lalanne, and D. Peyrade, "Deterministic design of wavelength scale, ultra-high Q photonic crystal nanobeam cavities," Opt. Express **15**, 16090 (2007). 83

[17] E. Yablonovitch, "Inhibited spontaneous emission in solid-state physics and electronics," Phys. Rev. Lett. **58**, 2059 (1987). 83

[18] S. John, "Strong localization of photons in certain disordered dielectric superlattices," Phys. Rev. Lett. **58**, 2486 (1987). 83

[19] P. R. Villeneuve, S. Fan, and J. D. Joannopoulos, "Microcavities in photonic crystals: Mode symmetry, tunability, and coupling efficiency," Phys. Rev. B **54**, 7837 (1996). 83

[20] E. Özbay, G. Tuttle, M. Sigalas, C. M. Soukoulis, and K. M. Ho, "Defect structures in a layer-by-layer photonic band-gap crystal," Phys. Rev. B **51**, 13961 (1995). 83

[21] M. Okano, A. Chutinan, and S. Noda, "Analysis and design of single-defect cavities in a three-dimensional photonic crystal," Phys. Rev. B. **66**, 165211 (2002). 83, 94

[22] J. D. Joannopoulos, S. G. Johnson, J. N. Winn, and R. D. Meade, *"Photonic crystals: Molding the flow of light,"* (Princeton University Press, Princeton NJ, 2008). 83, 85, 108

[23] K. M. Ho, C. T. Chan, C. M. Soukoulis, R. Biswas, and M. Sigalas, "Photonic band gaps in three dimensions: new layer-by-layer periodic structures," Solid State Commun. **89**, 413 (1994). 83

[24] R. Hillebrand, S. Senz, W. Hergert, and U. Gösele, "Macroporous-silicon-based three-dimensional photonic crystal with a large complete band gap," J. Appl. Phys. **94**, 2758 (2003). 83, 85

[25] L. A. Woldering, A. P. Mosk, R. W. Tjerkstra, and W. L. Vos, "The influence of fabrication deviations on the photonic band gap of three-dimensional inverse woodpile nanostructures," J. Appl. Phys. **105**, 093108 (2009). 83, 85

[26] L. A. Woldering, A. P. Mosk, and W. L. Vos, "Design of a three-dimensional photonic band gap cavity in a diamondlike inverse woodpile photonic crystal," Phys. Rev. B. **90**, 115140 (2014). 83, 84, 85, 86, 95, 96, 103, 104, 105, 108

[27] E. M. Purcell, H. C. Torrey, and R. V. Pound, "Resonance absorption by nuclear magnetic moments in a solid," Phys. Rev. **69**, 37 (1946). 84, 94

[28] A. F. Koenderink, L. Bechger, H. P. Schriemer, A. Lagendijk, and W. L. Vos, "Broadband fivefold reduction of vacuum fluctuations probed by dyes in photonic crystals," Phys. Rev. Lett. **88**, 143903 (2002). 84, 94

[29] S. Ogawa, M. Imada, S. Yoshimoto, M. Okano, and S. Noda, "Control of Light Emission by 3D Photonic Crystals," Science **305**, 227 (2004). 84, 94

[30] P. Lodahl, A. F. van Driel, I. S. Nikolaev, A. Irman, K. Overgaag, D. Vanmaekelbergh, and W. L. Vos, "Controlling the dynamics of spontaneous emission from quantum dots by photonic crystals," Nature (London) **430**, 654 (2004). 84, 94

[31] M. D. Leistikow, A. P. Mosk, E. Yeganegi, S. R. Huisman, A. Lagendijk, and W. L. Vos, "Inhibited spontaneous emission of quantum dots observed in a 3D photonic band gap," Phys. Rev. Lett. **107**, 193903 (2011). 84, 94

[32] S. G. Johnson and J. D. Joannopoulos, "Block-iterative frequency-domain methods for Maxwell's equations in a planewave basis," Opt. Express **8**, 3 (2001). 85, 103, 108

[33] L. A. Woldering, R. W. Tjerkstra, H. V. Jansen, I. D. Setija, and W. L. Vos, "Periodic arrays of deep nanopores made in silicon with reactive ion etching and deep UV lithography," Nanotechnology **19**, 145304 (2008). 85

[34] S. R. Huisman, R. V. Nair, L. A. Woldering, M. D. Leistikow, A. P. Mosk, and W. L. Vos, "Signature of a three-dimensional photonic band gap observed with silicon inverse woodpile photonic crystals," Phys. Rev. B **83**, 205313 (2011). 85

[35] "COMSOL Multiphysics® v. 5.2. www.comsol.com, COMSOL AB, Stockholm, Sweden". 85, 103

[36] J.M. Jin, *"The finite element method in electromagnetics,"* (Wiley-IEEE Press, New York, 2000). 85

[37] D. Devashish, S. B. Hasan, J. J. W. van der Vegt, and W. L. Vos, "Reflectivity calculated for a three-dimensional silicon photonic band gap crystal with finite support," Phys. Rev. B **95**, 155141 (2017). 85, 97

[38] Throughout this chapter, we express frequency as a reduced frequency $\tilde{\omega} = \omega a/(2\pi c')$, with ω the frequency, a the lattice parameter, c' the speed of light that is not to be confused with the lattice parameter c. In this definition, the reduced frequency $\tilde{\omega}$ is expressed in units of (a/λ). 86

[39] Serendipity is a high performance computing cluster made by Dell at MACS, University of Twente. It consists of 16 nodes, each node having 40 cores. Each node has infiniband 56 GBPS speed and memory equivalent to 256 GB. 86, 105

[40] O. S. Ojambati, *"Stirring the propagation and the absorption of light in complex nanophotonic systems,"* Chapter 6, PhD thesis (2016). 87

[41] D. J. Griffiths, *"Introduction to electrodynamics,"* (Prentice Hall, Upper Saddle River NJ, 1999). 93, 94

[42] U. Fano, "Effects of configuration interaction on intensities and phase shifts," Phys. Rev. **124**, 1866 (1961). 94, 99

[43] K. H. Drexhage, "Influence of a dielectric interface on fluorescence decay time," J. Lumin. **1-2**, 693 (1970). 94

[44] J. T. Robinson, C. Manolatou, L. Chen, and M. Lipson, "Ultrasmall mode volumes in dielectric optical microcavities," Phys. Rev. Lett. **95**, 143901 (2005). 95, 96

[45] S. Noda, M. Fujita, and T. Asano, "Spontaneous-emission control by photonic crystals and nanocavities," Nat. Photon. **1**, 449 (2007). 95

[46] S. Fan and J. D. Joannopoulos, "Analysis of guided resonances in photonic crystal slab," Phys. Rev. B. **65**, 235112 (2002). 99

[47] J. P. Vasco, H. Vinck-Posada, P. T. Valentim, and P. S. S. Guimaraes, "Modeling of Fano resonances in the reflectivity of photonic crystal cavities with finite spot size excitation," Opt. Express **21**, 31336 (2013). 99

4

[48] M. A. Green, "Self-consistent optical parameters of intrinsic silicon at 300K including temperature coefficient," Sol. Energy Mat. Sol. Cells, **92**, 1305 (2008). 99

[49] Edited by M. Ghulinyan and L. Pavesi, *"Light Localisation and Lasing: Random and Pseudorandom Photonic Structures,"* (Cambridge Univ. Press, Cambridge, 2015).

[50] J. D. Joannopoulos, P. R. Villeneuve, and S. Fan, "Photonic crystals: putting a new twist on light," Nature (London) **386**, 143 (1997).

[51] R. D. Meade, A. M. Rappe, K. D. Brommer, J. D. Joannopoulos, and O. L. Alerhand, "Accurate theoretical analysis of photonic band-gap materials," Phys. Rev. B **48**, 8434 (1993).

[52] I. Andonegui and A. J. Garcia-Adeva, "The finite element method applied to the study of two-dimensional photonic crystals and resonant cavities," Opt. Express **21**, 4072 (2013).

[53] E. A. Muljarov and W. Langbein, "Exact mode volume and Purcell factor of open optical systems," Phys. Rev. B **94**, 235438 (2016). 108

[54] P. T. Kristensen, C. van Vlack, and S. Hughes, "Generalized effective mode volume for leaky optical cavities," Opt. Lett. **37**, 1649 (2012). 108

CHAPTER 5

Div-DGMax: a discontinuous Galerkin finite element solver for the time-harmonic Maxwell equations with an explicitly enforced divergence constraint

5.1 Introduction

A wide range of numerical methods is available to model the propagation propagation of light in nanophotonic systems. The choice of a numerical method is, however, consequential for the accuracy of the results for nanophotonic structures with disrupted symmetries [1]. Several methods, *e.g.*, the multiple multipole technique for spheroidal particles [2] and the Fourier modal method for layered periodic structures [3, 4, 37], can only work with sufficient accuracy for the specific applications in nanophotonics they were primarily developed for.

The most sought-after and computationally efficient general purpose numerical method in nanophotonics is arguably the finite difference time domain (FDTD) method [6]. The FDTD method discretizes space using the Yee scheme [7] and works well in regions with a smooth solution. Near curved material interfaces and boundaries, the FDTD method, however, suffers from the staircase effect. This can be slightly alleviated using linear interpolation, but generally still results in loss of accuracy. Also, due to the use of Taylor expansions and a regular mesh the FDTD suffers from a loss in accuracy near singularities and is difficult to use for complex geometries. Moreover, it is hard to perform local mesh refinement in FDTD due to the staggered mesh. Despite several recent improvements, it is still a difficult research question to improve the spatial accuracy of FDTD beyond the limits of the basic algorithm [8–11].

The other notable general purpose method is the conforming finite element method (FEM) [12–20] that in general employs Nédélec elements, which satisfy the DeRham complex and allow for unstructured meshes. The conforming FEM is supported by an extensive mathematical theory, which gives it a solid theoretical basis. However, the conforming FEM requires curl-conforming finite element spaces and hence it becomes difficult to use it for local hp-adaptation, where h-adaptation refers to the local mesh refinement and p-adaptation to the local adjustment of the polynomial order.

The discontinuous Galerkin finite element method (DGFEM) [21–26, 29], is

mathematically proven to be much better suited, compared to the conforming FEM, for hp-adaptation. Locally increasing the spatial resolution (hp-refinement) accurately models strong, local variations in the electromagnetic fields, *e.g.*, in photonic crystals [30] with and without cavities. The discontinuities in the electromagnetic fields are naturally dealt with by the employed discontinuous basis functions. Moreover, the DG method treats elements individually due to the discontinuous basis function and hence is ideally suited for parallelization on multiple cores [1].

Accurate eigenvalue computations, however, require that the DG discretization satisfies the divergence constraint in the time-harmonic Maxwell equations [1, 28]. For the eigenvalue problem of the Maxwell equations, the neglect of the divergence condition leads to a large number of zero eigenvalues, which belong to the null space of the curl-curl operator. These zero-frequency solutions correspond to longitudinal fields [31]. Therefore, iterative eigenvalue solvers have difficulty to find the physical eigenvalues with the smallest frequencies due to the large spurious null space.

In this chapter, we study an accurate and efficient discontinuous Galerkin finite element (DGFEM) solver for the time-harmonic Maxwell equations for the periodic photonic nanostructures with disrupted symmetries. First, we provide a short description of the Maxwell equations. We explicitly incorporate the divergence constraint by introducing a new variable using a Lagrange multiplier and derive the mixed-formulation of the Maxwell equations. Next, we derive the DG weak formulation of the mixed-formulation, and use the Interior Penalty flux to obtain the discontinuous Galerkin discretization. Finally, we present the k shifted eigenvalue problem formulation with an explicitly enforced divergence condition for periodic dielectric materials. This method is well equipped for efficient photonic band structure calculations.

5.2 Model problem

5.2.1 Maxwell equations

The electromagnetic propagation of light is governed by the four macroscopic Maxwell equations [30, 32]. In S.I. units, these equations are

$$\nabla \cdot D = \rho \quad \text{(Gauss' law)}, \tag{5.1a}$$

$$\nabla \times E + \frac{\partial B}{\partial t} = 0 \quad \text{(Faraday's law of induction)}, \tag{5.1b}$$

$$\nabla \cdot B = 0 \quad \text{(Gauss' law of Magnetism)}, \text{ and} \tag{5.1c}$$

$$\nabla \times H - \frac{\partial D}{\partial t} = J \quad \text{(Ampere's circuit law with Maxwell's addition)}, \tag{5.1d}$$

where $E, H \in \mathbb{R}^3$, respectively, are the macroscopic electric and magnetic fields, $D, B \in \mathbb{R}^3$, respectively, are the displacement and magnetic induction fields, and $\rho \in \mathbb{R}$ and $J \in \mathbb{R}^3$ are the free charge and the current density. We consider a domain $\Omega \subseteq \mathbb{R}^3$ with a mixed dielectric medium, which is a composite of

regions of homogeneous dielectric material with the dielectric permittivity as a function of the position vector $\vec{r}$. The structure does not vary with time, and there are no free charges, therefore we take $\rho = 0$ for this medium. We use constitutive equations to relate the displacement field D to the electric field E and the magnetic induction field B to the magnetic field H. We assume that

1. the field strengths are sufficiently small to be in the linear regime,

2. the dielectric material is macroscopic and isotropic, so that $E(\vec{r}, \omega)$ and $D(\vec{r}, \omega)$, with $\omega \in \mathbb{R}$ the angular frequency, are related by the vacuum permittivity ϵ_0 times a scalar dielectric function $\epsilon(\vec{r}, \omega)$, known as the relative permittivity.

Assuming the validity of these two approximations, we obtain the following constitutive relation

$$D(\vec{r}) = \epsilon_0 \epsilon(\vec{r}, \omega) E(\vec{r}). \tag{5.2}$$

Using similar approximations for the magnetic induction field and the magnetic field, we obtain the constitutive relation

$$B(\vec{r}) = \mu_0 \mu(\vec{r}, \omega) H(\vec{r}). \tag{5.3}$$

Applying these assumptions in the macroscopic Maxwell equations (5.1), we obtain

$$\nabla \cdot \epsilon E(\vec{r}, t) = 0, \tag{5.4a}$$

$$\nabla \times E(\vec{r}, t) = -\mu \frac{\partial H(\vec{r}, t)}{\partial t}, \tag{5.4b}$$

$$\nabla \cdot \mu H(\vec{r}, t) = 0, \tag{5.4c}$$

$$\nabla \times H(\vec{r}, t) = J(\vec{r}, t) + \epsilon \frac{\partial E(\vec{r}, t)}{\partial t}, \tag{5.4d}$$

in the domain $\Omega \subset \mathbb{R}^3$, where $\nabla = (\frac{\partial}{\partial x}, \frac{\partial}{\partial y}, \frac{\partial}{\partial z})^\mathrm{T}$ is the gradient operator, $\epsilon = \epsilon_0 \epsilon(\vec{r}, \omega)$ is the electric permittivity, and $\mu = \mu_0 \mu(\vec{r}, \omega)$ is the magnetic permeability.

We observe that E, H, and J are functions of both space and time. Since we assume the linear regime of the Maxwell equations, we can separate the time dependence from the spatial dependence by expanding the fields into a set of harmonic modes [30]. These harmonic modes represent the field patterns that vary sinusoidally (harmonically) with time. We employ complex-valued fields and take the real part to obtain the physical fields. Therefore, we write a harmonic mode as a spatial pattern (or a mode profile) times a complex exponential

$$E(\vec{r}, t) = \bar{E}(\vec{r}) e^{i\omega t}, \tag{5.5a}$$

$$H(\vec{r}, t) = \bar{H}(\vec{r}) e^{i\omega t}, \tag{5.5b}$$

$$J(\vec{r}, t) = \bar{J}(\vec{r}) e^{i\omega t}, \tag{5.5c}$$

with $i = \sqrt{-1}$ and ω the angular frequency. Using (5.5) in (5.4), we obtain

$$\nabla \cdot \epsilon \bar{E}(\vec{r}) = 0, \tag{5.6a}$$
$$\nabla \times \bar{E}(\vec{r}) = -i\omega\mu\bar{H}(\vec{r}), \tag{5.6b}$$
$$\nabla \cdot \mu\bar{H}(\vec{r}) = 0, \tag{5.6c}$$
$$\nabla \times \bar{H}(\vec{r}) = i\omega\bar{J}(\vec{r}) + i\omega\epsilon\bar{E}(\vec{r}). \tag{5.6d}$$

When (5.6a) and (5.6c) hold for the initial conditions and $\nabla \cdot J = 0$, (5.6b) and (5.6d) will ensure that (5.6a) and (5.6c) are true at all later times [30]. This shows that the two divergence conditions (5.6a) and (5.6c) are consistency conditions and hence should also be employed to ensure the consistency of the numerical solution. The two curl equations (5.6b) and (5.6d) relate the electric field $E(\vec{r})$ to the magnetic field $H(\vec{r})$. To combine these two equations, we divide by μ, take the curl of (5.6b), and insert (5.6d) into (5.6b).

The resulting equation with $E(\vec{r})$ as the free variable is the time-harmonic Maxwell equation for the electric field

$$\nabla \times (\mu^{-1}\nabla \times \bar{E}) = i\omega\bar{J} - \omega^2\epsilon\bar{E}. \tag{5.7}$$

Let us write $j = i\omega\bar{J}(x)$ and drop the overhead bar for simplicity, we obtain

$$\nabla \times (\mu^{-1}\nabla \times E) - \omega^2\epsilon E = j, \tag{5.8}$$

which is commonly termed as the **master equation** in Ref. [30]. Combined with the divergence condition (5.6a), it gives the field profile of $E(\vec{r})$. To calculate a harmonic solution of (5.8) for a known current source j, we assume that the domain Ω has a perfectly conducting boundary. Therefore, the boundary condition is

$$n \times E = g \text{ at } \Gamma = \partial\Omega, \tag{5.9}$$

where $n \in \mathbb{R}^3$ denotes the outward normal unit vector at $\partial\Omega$, the boundary of Ω, and $g \in \mathbb{R}^3$ denotes the tangential trace of the electric field E.

We made the choice to use the E field as the free variable in the coupled equations (5.6b) and (5.6d). The H field, if explicitly needed, can always be retrieved using (5.6b) and the initial conditions.

5.2.2 Function spaces

We define notations and function spaces that will be used throughout this chapter. For a given open domain Ω in $\mathbb{R}^2$ or $\mathbb{R}^3$, we denote the Hilbertian Sobolev spaces of real or complex scalar- or vector-valued functions by $H^s(\Omega)^d$, $d = 1, 2, 3$, with regularity exponent $s \geq 0$. For $s = 0$ we denote $H^s(\Omega)$ as $L^2(\Omega)$, which has the standard inner product denoted as $(\cdot, \cdot)_\Omega$. We use $||\cdot||_{s,\Omega}$ to represent the norm for the space $H^s(\Omega)^d$, $d = 1, 2, 3$. In addition, we define the following function spaces

$$H^1(\Omega) := \{v \in L^2(\Omega) : |\nabla v| \in L^2(\Omega)\}, \tag{5.10a}$$

$$H_0^1(\Omega) := \{v \in H^1(\Omega) : v = 0 \text{ at } \partial\Omega\}, \tag{5.10b}$$

$$H(\text{div}; \Omega) := \{v \in L^2(\Omega)^3 : \nabla \cdot v \in L^2(\Omega)\}, \tag{5.10c}$$

$$H_0(\text{div}; \Omega) := \{v \in H(\text{div}; \Omega) : v \cdot n = 0 \text{ at } \partial\Omega\}, \tag{5.10d}$$

$$H(\text{div}^0; \Omega) := \{v \in H(\text{div}; \Omega) : \nabla \cdot v = 0 \text{ in } \Omega\}, \tag{5.10e}$$

$$H(\text{curl}; \Omega) := \{v \in L^2(\Omega)^3 : \nabla \times v \in L^2(\Omega)^3\}, \text{ and} \tag{5.10f}$$

$$H_0(\text{curl}; \Omega) := \{v \in H(\text{curl}; \Omega) : n \times v = 0 \text{ at } \partial\Omega\}. \tag{5.10g}$$

5.2.3 Mixed formulation of the Maxwell equations

Consider the domain $\Omega \subseteq \mathbb{R}^3$ with boundary Γ. The electric field $E \in H(\text{curl}; \Omega) \cap H(\text{div}^0; \Omega) \oplus H_0^1(\Omega)$ (see Sec. 5.2.2 for definitions of the Sobolev function spaces). We consider the $L^2(\Omega)^3$-orthogonal Helmholtz decomposition [14, 16, 17, 23, 26] of the function $E = u + \nabla\phi$ with $u \in H(\text{curl}; \Omega) \cap H(\text{div}^0; \Omega)$ and $\phi \in H_0^1(\Omega)$, where u represents the vector potential and ϕ represents the scalar potential of the system. Since the Helmholtz decomposition is orthogonal in $L^2(\Omega)^3$, it implies that $(u, \nabla\phi) = 0$ for all $q \in H_0^1(\Omega), u \in H(\text{curl}; \Omega) \cap H(\text{div}^0; \Omega)$. We define $p := \omega^2\phi$. Therefore, the wave equation (5.8) simplifies to

$$\nabla \times (\mu^{-1}\nabla \times u) - \omega^2\epsilon u - \epsilon\nabla p = 0.$$

Similarly, the divergence equation (5.6a) simplifies to

$$\nabla \cdot (\epsilon u) + \nabla \cdot \nabla\phi = 0.$$

We note that $\phi \in H_0^1(\Omega)$ requires $\phi = 0$ at $\partial\Omega$. This implies that the scalar potential ϕ is also zero in Ω, since $\phi = 0$ is the unique solution of

$$\nabla \cdot \nabla\phi = 0 \text{ in } \Omega \text{ with } \phi = 0 \text{ at } \Gamma.$$

Since $\phi \in H_0^1(\Omega)$, the perfectly conducting boundary condition given by (5.9) reduces to

$$n \times u = g \text{ at } \Gamma.$$

Therefore, the modified model problem, assuming $\nabla \cdot j = 0$, is to find a pair of (u, p), such that

$$\nabla \times (\mu^{-1}\nabla \times u) - \omega^2\epsilon u - \epsilon\nabla p = j \qquad \text{in } \Omega, \tag{5.11a}$$

$$\nabla \cdot (\epsilon u) = 0 \qquad \text{in } \Omega, \tag{5.11b}$$

$$n \times u = g \qquad \text{at } \Gamma, \tag{5.11c}$$

$$p = 0 \qquad \text{at } \Gamma. \tag{5.11d}$$

We now introduce the discontinuous Galerkin spaces, where we consider the Nédélec elements [27, 28]. Given a finite element tessellation $\mathcal{T}_h$ of the domain Ω in tetrahedral elements, we approximate the scalar- and vector-valued functions p and u, respectively, in the discontinuous finite element spaces Q_h and V_h, where

$$Q_h := \{q \in L^2(\Omega) : q|_K \in P^l(K), \forall K \in \mathcal{T}_h\}, \tag{5.12}$$

$$V_h := \{v \in L^2(\Omega)^3 : v|_K \in S^l(K), \forall K \in \mathcal{T}_h\}, \tag{5.13}$$

for an approximating order $l \geq 1$, with $P^l(K)$ denoting the space of Lagrange polynomials of degree at most l on K, $S^l(K)$ denoting the space of Nédélec elements of the first family [27].

5.2.4 Discontinuous Galerkin discretization

We consider shape-regular conforming meshes $\mathcal{T}_h$ that partition the domain Ω into tetrahedra. Here h denotes the granularity of the mesh $\mathcal{T}_h$, *i.e.*, $h = \max_{K \in \mathcal{T}_h} h_K$, where $h_K = \text{diameter}(K)$ for all $K \in \mathcal{T}_h$. We assume that the meshes are aligned with the discontinuities in the coefficients μ and ϵ. The set $\mathcal{F}_h^i$ represents the set of all internal faces in $\mathcal{T}_h$, and $\mathcal{F}_h^b$ represents the set of all boundary faces in $\mathcal{T}_h$. Therefore, the set of all faces is represented as $\mathcal{F}_h = \mathcal{F}_h^i \cup \mathcal{F}_h^b$.

For the piecewise smooth vector- and scalar-valued functions $v \in V_h$ and $q \in Q_h$, we introduce the following trace operators. Let us assume $F \in \mathcal{F}_h^i$ to be an internal face shared by two elements K^L and K^R. We define n^L as the unit outward normal vector of element K^L at a face F and n^R as the unit outward normal vector of element K^R at a face F. We note that $n_L = -n_R$. We define the tangential jump of a vector-valued function v at $F \in F_h^i$ by

$$[[v]]_T \equiv n^L \times v^L + n^R \times v^R$$

and the normal jump by

$$[[v]]_N \equiv n^L \cdot v^L + n^R \cdot v^R.$$

The normal jump of a scalar-valued function q is defined by

$$[[q]]_N \equiv n^L q^L + n^R q^R.$$

Similarly, we define the averages of v and q by

$$\{\{v\}\} \equiv \frac{1}{2}(v^L + v^R) \text{ and } \{\{q\}\} \equiv \frac{1}{2}(q^L + q^R).$$

For the boundary faces $F \in \mathcal{F}_h^b$, we define for a vector-valued function v the tangential jump $[[v]]_T \equiv n^L \times v^L$ and the normal jump $[[v]]_N \equiv n^L \cdot v^L$; for a scalar-valued function q we define the normal jump $[[q]]_N \equiv n^L q^L$. The averages are defined as $\{\{v\}\} \equiv v$ and $\{\{q\}\} \equiv q$.

We also define the following lifting operators [26],

$$(L(u), w)_\Omega \equiv \sum_{F \in \mathcal{F}_h^i} \int_F \{\{u\}\} \cdot [[w]]_T dS, \qquad (5.14)$$

$$(S(u), w)_\Omega \equiv \sum_{F \in \mathcal{F}_h} \int_F [[u]]_T \cdot \{\{w\}\} dS. \qquad (5.15)$$

These operators will later on be used to eliminate the auxiliary variables in the discontinuous Galerkin discretization. We use ∇_h to denote the elementwise spatial derivative ∇ operator.

5.2.5 Weak formulation

To obtain the discontinuous Galerkin discretization [17, 28] of the modified model problem (5.11a - 5.11d), we introduce an auxiliary variable M, such that the wave equation (5.11a) turns into a coupled first order system. We assume

$$M - \mu^{-1}\nabla \times u = 0 \text{ in } \Omega. \qquad (5.16)$$

Introducing (5.16) into (5.11a), we obtain

$$\nabla \times M - \omega^2 \epsilon u - \epsilon \nabla p = j \text{ in } \Omega. \qquad (5.17)$$

We assume arbitrary test functions $w, v \in V_h$. Multiplying (5.16) by the test function $w \in V_h$ and (5.17) by the test function $v \in V_h$, replacing u with $u_h \in V_h$ and p with $p_h \in Q_h$, and integrating over the domain Ω, we obtain

$$(M_h, w)_\Omega = \sum_{K \in \mathcal{T}_h} \int_K (\mu^{-1}(\nabla \times u_h)) \cdot w dx \qquad (5.18)$$

and

$$(j_h, v)_\Omega = \sum_{K \in \mathcal{T}_h} \int_K \left((\nabla \times M_h) \cdot v - \omega^2 \epsilon u_h \cdot v - \epsilon \nabla p_h \cdot v \right) dx. \qquad (5.19)$$

Using the identity

$$(\nabla \times A) \cdot B = \nabla \cdot (A \times B) + (\nabla \times B) \cdot A \qquad (5.20)$$

and the divergence theorem, we obtain

$$(M_h, w)_\Omega = \sum_{K \in \mathcal{T}_h} \int_K \nabla \times (\mu^{-1}w) \cdot u_h dx + \sum_{K \in \mathcal{T}_h} \int_{\partial K} (u_h^* \times \mu^{-1}w) \cdot n dS, \qquad (5.21)$$

where u^* denotes the numerical flux for u. The numerical flux u^* is introduced since $u_h \in V_h$ has a multivalued trace at the element faces.

Using (5.20), we can further transform (5.21) into

$$
(M_h, w)_\Omega = \sum_{K \in \mathcal{T}_h} \int_K \Big((\nabla \times u_h) \cdot \mu^{-1} w - \nabla \cdot (u_h \times \mu^{-1} w) \Big) dx
$$
$$
+ \sum_{K \in \mathcal{T}_h} \int_{\partial K} (u_h^* \times \mu^{-1} w) \cdot n \, dS.
$$

Applying the divergence theorem again on the second term on right hand side and using the fact that the test function w is zero outside element K, we get

$$
(M_h, w)_\Omega = \sum_{K \in \mathcal{T}_h} \int_K (\nabla \times u_h) \cdot \mu^{-1} w \, dx
$$
$$
+ \sum_{K \in \mathcal{T}_h} \int_{\partial K} (n \times (u_h^* - u_h)) \cdot \mu^{-1} w \, dS.
\tag{5.22}
$$

We now introduce two mathematical identities, which will be employed several times in this Chapter. First, for any $u_h, v_h \in V_h$, we have

$$
\sum_{K \in \mathcal{T}} \int_{\partial K} (n \times u_h) \cdot v_h \, ds \equiv \sum_{F \in \mathcal{F}_h^i} \int_F \Big([[u_h]]_T \cdot \{\{v_h\}\} - [[v_h]]_T \cdot \{\{u_h\}\} \Big) dS
$$
$$
+ \sum_{F \in \mathcal{F}_h^b} \int_F [[u_h]]_T \cdot \{\{v_h\}\} dS.
\tag{5.23}
$$

This relation can be easily verified by introducing the expression for the average and the tangential jump into the right hand side of (5.23), yielding

$$
= \sum_{F \in \mathcal{F}_h^i} \int_F \Big((n^L \times u_h^L) \cdot v_h^L + (n^R \times u^R) \cdot v_h^R \Big) dS + \sum_{F \in \mathcal{F}_h^b} \int_F (n \times u_h) \cdot v_h \, dS
$$

Since each internal face appears twice in the summation over all the faces ∂K and using $n^R = -n^L$, we immediately obtain the left hand side of (5.23). The second relation we use to simplify to the discontinuous Galerkin discretization is $\forall u_h \in V_h, \, q_h \in Q_h$

$$
\sum_{K \in \mathcal{T}} \int_{\partial K} q_h u_h \cdot n \, dS \equiv \sum_{F \in \mathcal{F}_h^i} \int_F \Big([[q_h]]_N \cdot \{\{u_h\}\} + [[u_h]]_N \{\{q_h\}\} \Big) dS
$$
$$
+ \sum_{F \in \mathcal{F}_h^b} \int_F [[q_h]]_N \cdot \{\{u_h\}\} dS.
\tag{5.24}
$$

This relation can also be easily verified by introducing the jumps and the averages for scalar- and vector-valued functions defined in Section 5.2.4 on the right hand

side of (5.24) and using $n^R = -n^L$. Using (5.23) in (5.22), we now obtain

$$
\begin{aligned}
(M_h, w)_\Omega = {} & \sum_{K \in \mathcal{T}_h} \int_K (\nabla \times u_h) \cdot \mu^{-1} w dx \\
& + \sum_{F \in \mathcal{F}_h^i} \int_F \Big([[u_h^* - u_h]]_T \cdot \{\{\mu^{-1} w\}\} \\
& \qquad\qquad - [[\mu^{-1} w]]_T \cdot \{\{u_h^* - u_h\}\} \Big) dS \\
& + \sum_{F \in \mathcal{F}_h^b} \int_F [[u_h^* - u_h]]_T \cdot \{\{\mu^{-1} w\}\} dS.
\end{aligned}
\tag{5.25}
$$

Introducing the lifting operators, defined in (5.14) and (5.15), into (5.25), we obtain

$$
(M_h, w)_\Omega = (\mu^{-1} \nabla_h \times u_h, w)_\Omega + (\mu^{-1} S(u_h^* - u_h), w)_\Omega - (\mu^{-1} L(u_h^* - u_h), \ w)_\Omega.
$$

Since $w \in V_h$ is an arbitrary test function, we deduce the expression

$$
M_h = \mu^{-1} \nabla_h \times u_h + \mu^{-1} S(u_h^* - u_h) - \mu^{-1} L(u_h^* - u_h)
\tag{5.26}
$$

almost everywhere in Ω. Next, we consider (5.19), rewritten as

$$
(j_h, v)_\Omega = \sum_{K \in \mathcal{T}_h} \int_K \Big(\nabla \cdot (M_h \times v) + M_h \cdot (\nabla \times v) - \omega^2 \epsilon u_h \cdot v - \epsilon \nabla p_h \cdot v \Big) dx.
$$

Using the divergence theorem on the first term, we obtain

$$
\begin{aligned}
(j_h, v)_\Omega = {} & \sum_{K \in \mathcal{T}_h} \int_K \Big(M_h \cdot (\nabla \times v) - \omega^2 \epsilon u_h \cdot v - \epsilon \nabla p_h \cdot v \Big) dx \\
& + \sum_{K \in \mathcal{T}_h} \int_{\partial K} (n \times M_h^*) \cdot v dS,
\end{aligned}
$$

with M_h^* the numerical flux for M_h. Now, using identity (5.23) we can express the contribution from the element boundaries as a sum over all faces in $\mathcal{T}_h$.

$$
\begin{aligned}
(j_h, v)_\Omega = {} & (M_h, \nabla_h \times v)_\Omega - (\omega^2 \epsilon u_h, v)_\Omega - (\nabla_h p_h, \epsilon v)_\Omega \\
& + \sum_{F \in \mathcal{F}_h^i} \int_F \Big([[M_h^*]]_T \cdot \{\{v\}\} - [[v]]_T \cdot \{\{M_h^*\}\} \Big) dS \\
& + \sum_{F \in \mathcal{F}_h^b} \int_F [[M_h^*]]_T \cdot \{\{v\}\} dS.
\end{aligned}
\tag{5.27}
$$

Next, we substitute the expression for M_h, given by (5.26), into (5.27) and obtain

$$
\begin{aligned}
(j_h, v)_\Omega = {} & (\mu^{-1}\nabla_h \times u_h, \nabla_h \times v)_\Omega - (\omega^2 \epsilon u_h, v)_\Omega - (\nabla_h p_h, \epsilon v)_\Omega \\
& + (S(u_h^* - u_h), \mu^{-1}\nabla_h \times v)_\Omega - (L(u_h^* - u_h), \mu^{-1}\nabla_h \times v)_\Omega \\
& + \sum_{F \in \mathcal{F}_h^i} \int_F \Big([[M_h^*]]_T \cdot \{\{v\}\} - [[v]]_T \cdot \{\{M_h^*\}\}\Big)dS \\
& + \sum_{F \in \mathcal{F}_h^b} \int_F [[M_h^*]]_T \cdot \{\{v\}\}dS.
\end{aligned}
$$

Replacing the lifting operators with their respective definitions given by (5.14) and (5.15), we obtain

$$
\begin{aligned}
(j_h, v)_\Omega = {} & (\mu^{-1}\nabla_h \times u_h, \nabla_h \times v)_\Omega - (\omega^2 \epsilon u_h, v)_\Omega - (\nabla_h p_h, \epsilon v)_\Omega \\
& + \sum_{F \in \mathcal{F}_h^i} \int_F \Big([[M_h^*]]_T \cdot \{\{v\}\} - [[v]]_T \cdot \{\{M_h^*\}\} \\
& \qquad\qquad + [[u_h^* - u_h]]_T \cdot \{\{\mu^{-1}\nabla \times v\}\} \\
& \qquad\qquad - \{\{u_h^* - u_h\}\} \cdot [[\mu^{-1}\nabla \times v]]\Big)dS \\
& + \sum_{F \in \mathcal{F}_h^b} \int_F \Big([[M_h^*]]_T \cdot \{\{v\}\} + [[u_h^* - u_h]]_T \cdot \{\{\mu^{-1}\nabla \times v\}\}\Big)dS.
\end{aligned}
\tag{5.28}
$$

The Lagrange multiplier contribution can be further evaluated using integration by parts and identity (5.24) yielding

$$
\begin{aligned}
(\nabla_h p_h, \epsilon v)_\Omega = {} & \sum_{F \in \mathcal{F}_h^i} \int_F \Big([[p_h^*]]_N \cdot \{\{\epsilon v\}\} + [[\epsilon v]]_N \{\{p_h^*\}\}\Big)dS \\
& + \sum_{F \in \mathcal{F}_h^b} \int_F [[p_h^*]]_N \cdot \{\{\epsilon v\}\}dS - (p_h, \nabla_h \cdot (\epsilon v))_\Omega.
\end{aligned}
\tag{5.29}
$$

Now, substituting relation (5.29) for $(\nabla_h p_h, \epsilon v)_\Omega$ into (5.28) and a second inte-

gration by parts of the Lagrange multiplier contribution containing p gives

$$
\begin{aligned}
(j_h, v)_\Omega = {} & (\mu^{-1} \nabla_h \times u_h, \nabla_h \times v) - (\omega^2 \epsilon u_h, v)_\Omega - (\nabla_h p_h, \epsilon v)_\Omega \\
& - \sum_{F \in \mathcal{F}_h^i} \int_F \Big([\![p_h^* - p_h]\!]_N \cdot \{\{\epsilon v\}\} + [\![\epsilon v]\!]_N \{\{p_h^* - p_h\}\} \Big) dS \\
& - \sum_{F \in \mathcal{F}_h^b} \int_F [\![p_h^* - p_h]\!]_N \cdot \{\{\epsilon v\}\} dS \\
& + \sum_{F \in \mathcal{F}_h^i} \int_F \Big([\![M_h^*]\!]_T \cdot \{\{v\}\} - [\![v]\!]_T \cdot \{\{M_h^*\}\} \\
& \qquad\qquad + [\![u_h^* - u_h]\!]_T \cdot \{\{\mu^{-1} \nabla \times v\}\} \\
& \qquad\qquad - \{\{u_h^* - u_h\}\} \cdot [\![\mu^{-1} \nabla \times v]\!] \Big) dS \\
& + \sum_{F \in \mathcal{F}_h^b} \int_F \Big([\![M_h^*]\!]_T \cdot \{\{v\}\} + [\![u_h^* - u_h]\!]_T \cdot \{\{\mu^{-1} \nabla \times v\}\} \Big) dS.
\end{aligned}
\tag{5.30}
$$

In the expression (5.30) we still need to define the numerical fluxes u_h^*, p_h^*, M_h^*. There are many ways to do this. Here, we use the Interior Penalty (IP) numerical fluxes defined in [21, 23, 26, 28, 29]. For an interior face $F \in \mathcal{F}_h^i$, we define

$$
\begin{aligned}
u_h^* &:= \{\{u_h\}\}, \\
M_h^* &:= \{\{\mu^{-1} \nabla \times u_h\}\} - a_F [\![u_h]\!]_T, \\
p_h^* &:= \{\{p_h\}\} - b_F [\![\epsilon u_h]\!]_N, \\
\epsilon u_h^* &:= \{\{\epsilon u_h\}\} - c_F [\![p_h]\!]_N,
\end{aligned}
$$

with $a_F, b_F, c_F \in \mathbb{R}^+$ the penalty coefficients. For a boundary face $F \in \mathcal{F}_h^b$, we define

$$
\begin{aligned}
n \times u_h^* &:= g_h, \\
M_h^* &:= \{\{\mu^{-1} \nabla \times u_h\}\} + a_F g_h - a_F [\![u_h]\!]_T, \\
p_h^* &:= 0, \\
\epsilon u_h^* &:= \{\{\epsilon u_h\}\} - c_F [\![p_h]\!]_N,
\end{aligned}
$$

with $c_F \in \mathbb{R}^+$ the penalty coefficients and $g_h \in V_h$ the L_2 approximation of the boundary value at Γ.

Introducing the Interior Penalty numerical fluxes into (5.30), using the relations for the jumps and averages, *e.g.*, $[\![\{\{u_h\}\}]\!] = 0$, and using $[\![M_h^*]\!]_T \cdot \{\{v\}\} =$

$-[[v]]_T \cdot \{\{M_h^*\}\}$ for $F \in \mathcal{F}_h^b$ gives

$$
(\mu^{-1}\nabla_h \times u_h, \nabla_h \times v)_\Omega - (\omega^2 \epsilon u_h, v)_\Omega - (\nabla_h p_h, \epsilon v)_\Omega
$$

$$
+ \sum_{F \in \mathcal{F}_h} \int_F [[p_h]]_N \cdot \{\{\epsilon v\}\} dS + \sum_{F \in \mathcal{F}_h^i} \int_F b_F [[\epsilon v]]_N [[\epsilon u_h]]_N dS
$$

$$
+ \sum_{F \in \mathcal{F}_h} \int_F \Big(- \{\{\mu^{-1}\nabla \times u_h\}\} \cdot [[v]]_T - \{\{\mu^{-1}\nabla \times v\}\} \cdot [[u_h]]_T
$$

$$
+ a_F [[u_h]]_T \cdot [[v]]_T \Big) dS \qquad (5.31)
$$

$$
+ \sum_{F \in \mathcal{F}_h^b} \int_F \Big(- a_F [[v]]_T \cdot g_h + g_h \cdot \{\{\mu^{-1}\nabla \times v\}\} \Big) dS = (j_h, v)_\Omega.
$$

The discontinuous Galerkin formulation for the divergence constraint

$$
\nabla \cdot (\epsilon u) = 0 \text{ in } \Omega \qquad (5.32)
$$

can be obtained analogously. Multiplying (5.32) with arbitrary test functions $q \in Q_h$, integrating over each element $K \in \mathcal{T}_h$ and using identity (5.24) gives

$$
- \sum_{K \in \mathcal{T}_h} \int_K \nabla q \cdot (\epsilon u_h) dx + \sum_{F \in \mathcal{F}_h^i} \int_F \Big([[q]]_N \cdot \{\{(\epsilon u_h^*)\}\} + [[\epsilon u_h^*]]_N \{\{q\}\} \Big) dS
$$

$$
+ \sum_{F \in \mathcal{F}_h^b} \int_F [[q]]_N \cdot \{\{\epsilon u_h^*\}\} ds = 0.
$$

First, we introduce the Interior Penalty flux, i.e., $\epsilon u_h^* = \{\{\epsilon u_h\}\} - c_F [[p_h]]_N$ on the faces $F \in \mathcal{F}_h$. Second, we eliminate double jumps and average operators, resulting in

$$
-(\epsilon u_h, \nabla_h q)_\Omega + \sum_{F \in \mathcal{F}_h} \int_F \Big(\{\{\epsilon u_h\}\} \cdot [[q]]_N - c_F [[p_h]]_N \cdot [[q]]_N \Big) dS = 0. \quad (5.33)
$$

We can now write the weak formulation of the time-harmonic mixed Maxwell equations with the divergence condition as: Find $(u_h, p_h) \in V_h \times Q_h$, such that $\forall (v, q) \in V_h \times Q_h$,

$$
a_h(u_h, v) - (\omega^2 \epsilon u_h, v)_\Omega + b_h(v, p_h) = (j_h, v)_\Omega + d_h(g_h, v)
$$

$$
b_h(u_h, q) - c_h(p_h, q) = 0, \qquad (5.34)
$$

with

$$
a_h(u_h, v) = (\mu^{-1}\nabla_h \times u_h, \nabla_h \times v)_\Omega
$$

$$
- \sum_{F \in \mathcal{F}_h} \int_F \Big(\{\{\mu^{-1}\nabla \times u_h\}\} \cdot [[v]]_T + \{\{\mu^{-1}\nabla \times v\}\} \cdot [[u_h]]_T \Big) dS
$$

$$
+ \sum_{F \in \mathcal{F}_h} \int_F a_F [[u_h]]_T \cdot [[v]]_T dS + \sum_{F \in \mathcal{F}_h^i} \int_F b_F [[\epsilon v]]_N [[\epsilon u_h]]_N dS,
$$

$$
(5.35)
$$

$$b_h(v, p_h) = -(\nabla_h p_h, \epsilon v)_\Omega + \sum_{F \in \mathcal{F}_h} \int_F [[p_h]]_N \cdot \{\{\epsilon v\}\} dS, \qquad (5.36)$$

$$c_h(p_h, q) = \sum_{F \in \mathcal{F}_h} \int_F c_F [[p_h]]_N \cdot [[q]]_N dS, \qquad (5.37)$$

$$d_h(g_h, v) = \sum_{F \in \mathcal{F}_h^b} \int_F \left(a_F [[v]]_T \cdot g_h - g_h \cdot \{\{\mu^{-1} \nabla \times v\}\} \right) dS. \qquad (5.38)$$

As described in the Section 5.2.4, ∇_h denotes the elementwise ∇ operator. We note that the bilinear form a_h corresponds to the interior penalty discretization of the curl-curl operator with an additional normal jump term. The bilinear form b_h discretizes the divergence constraint in the mixed Maxwell formulation using a discontinuous Galerkin scheme. The bilinear form c_h is a stabilization term, which controls the jumps in the scalar potential p. The parameters a_F, b_F, and c_F are positive stabilization parameters, which depend on the mesh size and the polynomial order.

5.2.6 Eigenvalue problem formulation

Let us consider light propagation inside an infinite domain Ω without any external current source, namely $j = 0$ on an infinite periodic domain. Therefore, (5.34) gives us a generalized eigenvalue problem in ω^2 as: Find $(u_h, p_h, \omega) \in V_h \times Q_h \times \mathbb{C}$, such that $\forall (v, q) \in V_h \times Q_h$,

$$\begin{aligned} a_h(u_h, v) + b_h(v, p_h) &= (\omega_h^2 \epsilon u_h, v)_\Omega, \\ b_h(u_h, q) - c_h(p_h, q) &= 0. \end{aligned} \qquad (5.39)$$

Ref. [28] presents the complete convergence theory for the eigenvalue problem given by (5.39). In order to consider a unit cell, which is infinitely repeated in all directions, we employ Bloch-Floquet periodic boundaries in the $\pm X$, $\pm Y$ and $\pm Z$ directions for the domain $\bar{\Omega}$, which denotes the unit cell with infinite periodicity to describe an infinite periodic crystal [28, 30] and introduce the Bloch mode expansion

$$u_h(r) = e^{ik \cdot r} \tilde{u}_h(r) \text{ and } p_h(r) = e^{ik \cdot r} \tilde{p}_h(r), \qquad (5.40)$$

with wave vector k. Here $\tilde{u}$ and $\tilde{p}$ are periodic, such that the period fits in the domain $\bar{\Omega}$, *i.e.*,

$$\tilde{u}_h(r) = \tilde{u}_h(r + R) \text{ and } \tilde{p}_h(r) = \tilde{p}_h(r + R) \qquad (5.41)$$

for all lattice vectors R. Introducing the Bloch mode expansion in (5.39), we obtain the eigenvalue problem: Find $(\tilde{u}_h, \tilde{p}_h, \omega_h) \in V_h \times Q_h \times \mathbb{C}$, such that $\forall (v, q) \in V_h \times Q_h$,

$$\begin{aligned} a_{k,h}(\tilde{u}_h, v) + b_{k,h}(v, \tilde{p}_h) &= (\omega^2 \epsilon \tilde{u}_h, v)_{\bar{\Omega}}, \\ b_{k,h}(\tilde{u}_h, q) - c_{k,h}(\tilde{p}_h, q) &= 0, \end{aligned} \qquad (5.42)$$

where

$$
\begin{aligned}
a_{k,h}(\tilde{u}_h, v) = {}& (\mu^{-1}\nabla_{k,h} \times \tilde{u}_h, \nabla_{k,h} \times v)_{\bar{\Omega}} \\
& - \sum_{F\in\mathcal{F}_h} \int_F \Big(\{\{\mu^{-1}\nabla_k \times \tilde{u}_h\}\} \cdot [[v]]_T \\
& \qquad\qquad + \{\{\mu^{-1}\nabla_k \times v\}\} \cdot [[\tilde{u}_h]]_T \Big) dS \\
& + \sum_{F\in\mathcal{F}_h} \int_F a_F [[\tilde{u}_h]]_T \cdot [[v]]_T\, dS \\
& + \sum_{F\in\mathcal{F}_h^i} \int_F b_F [[\epsilon v]]_N [[\epsilon\tilde{u}_h]]_N\, dS,
\end{aligned}
\tag{5.43}
$$

$$
b_{k,h}(v, \tilde{p}_h) = -(\nabla_{k,h}\tilde{p}_h, \epsilon v)_{\bar{\Omega}} + \sum_{F\in\mathcal{F}_h} \int_F [[\tilde{p}_h]]_N \cdot \{\{\epsilon v\}\}\, dS,
\tag{5.44}
$$

$$
c_{k,h}(\tilde{p}_h, q) = \sum_{F\in\mathcal{F}_h} \int_F c_F [[\tilde{p}_h]]_N \cdot [[q]]_N\, dS,
\tag{5.45}
$$

with $\nabla_k = \nabla + ik$. (5.42) represents the model problem to calculate a photonic band structure. The discontinuous Galerkin discretization of (5.42) results in the following matrices:

$$
\begin{aligned}
a_{k,h}(v_j, v_i) &\to A_{i,j}, \\
b_{k,h}(v_i, q_j) &\to B_{i,j}, \\
c_{k,h}(q_j, q_i) &\to C_{i,j}, \\
(v_j, \epsilon v_i) &\to M_{i,j}.
\end{aligned}
$$

Therefore, the generalized eigenvalue problem, in terms of above matrices, appears as:

$$
\begin{pmatrix} A & B \\ B^T & C \end{pmatrix} \begin{pmatrix} u_h \\ p_h \end{pmatrix} = \omega^2 \begin{pmatrix} M & 0 \\ 0 & 0 \end{pmatrix} \begin{pmatrix} u_h \\ p_h \end{pmatrix},
\tag{5.46}
$$

which first finds the smallest eigenvalue ω_h. Here, we are mainly interested in the smaller non-zero eigenvalues related to possible bands gaps. For an efficient computation of the photonic bandstructure, Ref. [28] reports that it is beneficial to rewrite the generalized eigenvalue problem (5.46) as:

$$
\begin{pmatrix} M & 0 \\ 0 & 0 \end{pmatrix} \begin{pmatrix} u_h \\ p_h \end{pmatrix} = \tilde{\omega}_h^2 \begin{pmatrix} A & B \\ B^T & C \end{pmatrix} \begin{pmatrix} u_h \\ p_h \end{pmatrix}.
\tag{5.47}
$$

with $\omega_h^2 = \frac{1}{\tilde{\omega}_h^2}$. The main benefit of this formulation is that it is much easier to efficiently compute the largest eigenvalues of a matrix than the non-zero eigenvalues close to zero as is commonly done in photonic crystal band gap computations. This is possible because the mixed formulation satisfies the divergence constraint (5.32). This eliminates the large null space of the curl-curl operator and we will only obtain non-zero eigenvalues.

5.3 Numerical results

The implementation of the discontinuous Galerkin finite element solver for the Maxwell equations by our research group is called DGMax. Being a first step, the DGMax software does not yet incorporate the divergence constraint and is implemented using C++ programming language within a software library for discontinuous Galerkin methods, known as hpGEM [33]. We employ open source softwares PETSc [34] as a linear system solver and SLEPc [35] as an eigenvalue solver. Building on the primitive code of DGMax, we are working on implementing the mixed formulation of Maxwell equations in (5.42) with the name Div-DGMax, which explicitly enforces the divergence constraint. However, we are currently still testing a part of the Div-DGMax solver, which corresponds to computing eigenvalues using SLEPc. Therefore, this chapter consists of results from the DGMax solver, which is a fully working version.

In order to validate the implementation of the DGMax solver, we calculate photonic band structures for known systems that can be accurately analyzed by analytical or numerical methods, such as a homogenous cube and a Bragg stack [29]. We use tetrahedra as basic elements in our finite element mesh to subdivide the 3D computational cell into elements. To compute accurate eigenvalues, we employ a mesh with **2560** tetrahedra for a homogenous cube and a Bragg stack. We approximate the vector-valued function u using the 1st order of hierarchic basis functions of $H(\text{curl})$ conforming finite elements proposed by Ainsworth and Coyle [36]. The DGMax solver only incorporates the vector-valued function u, and hence in (5.42) we use only $a(u, v)$, but not $b(u, q)$ and $c(p, q)$. We set the scalar-valued function as $p = 0$ and the stabilization parameters [29] as $a_F = 64$, $b_F = 0$, and $c_F = 0$. To compare with a well known numerical solver for photonic band structure, we use the MPB plane-wave expansion method [37] with a spatial resolution of $32 \times 32 \times 32 = $ **32768**, which is nearly 12 times larger than the mesh resolution of the DGMax solver.

Figure 5.1 (A) shows the 3D photonic band structure [38] between $\tilde{\omega} = 0$ to $\tilde{\omega} = 1.25$ for a homogenous cube with a constant dielectric permittivity $\epsilon = 1$ obtained using the analytical method (discussed in Appendix 5.A), the DGMax solver, and the MPB solver. We note that the MPB method calculates several non-physical eigenvalues, which are not present in the analytical solution. These spurious eigenvalues can be removed by assuming the homogeneous cube as a fictitious Bragg stack with $\epsilon_1 = 1$ and $\epsilon_2 = 1.00001$. But these spurious eigenvalues will again show up in computation by the MPB method for higher eigenvalues. We observe that eigenvalues computed by DGMax match very well with the analytical solution. However, Fig. 5.1 (A) exhibits small differences near $\tilde{\omega} = 1.1$ between eigenvalues computed by both the solvers and the analytically computed eigenvalues. These differences follow a systematic trend and hence are not statistical error. Since wavelength decreases with increasing frequency, an eigenvalue solver need higher spatial (or mesh) resolution to approximate the wave. Therefore, a higher spatial resolution will reduce this small systematic error. We note that DGMax computes many zero eigenvalues, since the divergence constraint is not explicitly enforced. These zero values contribute to nearly 60%
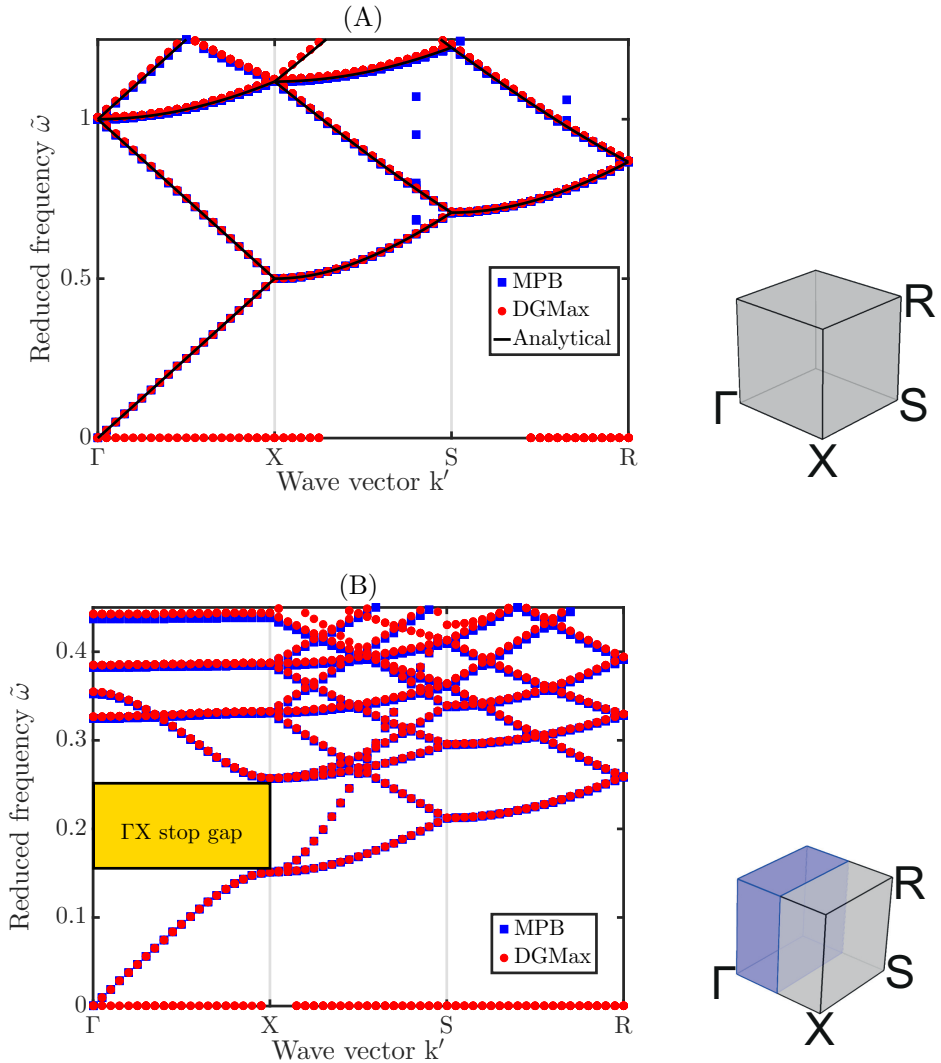
Figure 5.1: 3D photonic band structures for (A) a homogeneous cube and (B) a Bragg stack with the dielectric contrast along the ΓX direction in the wave vector space. The reduced frequency [38] $\tilde{\omega}$ is expressed in units of (a/λ), with a the lattice parameter. The wave vector is expressed as $k' = (ka/2\pi)$. The grey color indicates the air with the dielectric permittivity $\epsilon = 1$. The blue color indicates the high-index material with the dielectric permittivity $\epsilon = 13$. Black solid lines in (A) represent the analytically computed eigenvalues. Blue square represent eigenvalues computed by the MPB plane-wave expansion method [37]. Red circles represent eigenvalues computed by the DGMax solver. The DGMax solver is the discontinuous Galerkin software library for solving the Maxwell equations, where the divergence constraint is not yet explicitly enforced. The yellow bar marks the stop gap in the ΓX direction for a Bragg stack.

of all eigenvalues and hence cause a major waste of the computational time. Due to these zero values, smaller eigenvalues cannot be computed accurately for complex geometries by the DGMax solver using an iterative solver. We surmise that the mixed Maxwell formulation with an explicitly enforced divergence constraint will remove these zero eigenvalues.

In order to characterize the effect of a material interface, we calculate the 3D photonic band structure of a Bragg stack with dielectric permittivities $\epsilon_1 = 13$ and $\epsilon_2 = 1$ in the ΓX direction, as shown in Fig. 5.1 (B). A stop gap appears from $\tilde{\omega} = 0.15$ to $\tilde{\omega} = 0.26$ in the ΓX direction. We observe that the band structure computed by the MPB method matches very well with the one computed by the DGMax solver. However, we observe small statistical error near $\tilde{\omega} = 0.4$ between eigenvalues computed by both the solvers, which confirms that an eigenvalue solver needs a higher spatial resolution at higher frequencies. Again, we note that DGMax computes many zero eigenvalues, since the divergence constraint is not explicitly enforced. Based on results for a homogeneous cube and a Bragg stack, we consider the DGMax solver to be converged and validated. In near future, we will present results with an explicitly enforced divergence condition.

5.4 Conclusion

We describe an accurate and efficient discontinuous Galerkin finite element solver for the time-harmonic Maxwell equations for periodic photonic nanostructures with disrupted symmetries. We derived the mixed-formulation of Maxwell equations by explicitly incorporating the divergence constraint using a Lagrange multiplier. We employ the Interior penalty flux to obtain the discontinuous Galerkin discretization. We turn the k shifted eigenvalue formulation around by first computing for the largest eigenvalues of $\frac{1}{\omega_h}$, and subsequently the non-zero eigenvalues ω_h close to zero. Therefore, our eigenvalue formulation is well suited for the efficient calculation of the photonic band structures without the large null space of the curl-curl operator.

5.A Analytical photonic band structure calculation

Let us assume a homogenous cube with a constant dielectric permittivity $\epsilon = 1$. Therefore, the electric field $\bar{E}$ is constant and orthogonal to the wave vector k in (5.8), which can be rewritten for $j = 0$ as an eigenvalue problem

$$ik \times ik \times \bar{E} = \omega^2 \bar{E}. \tag{5.48}$$

(5.48) reduces to $||k||^2 = \omega^2$. To mimic an infinitely extended crystal, we employ Bloch-Floquet periodic boundary conditions in all three dimensions. Hence, eigenvalues for a 3D homogeneous crystal are $||k + 2\pi l|| = \omega^2 \ \forall l \in Z^3$, where $l = 0, 1, 2$, and so on. Figure 5.1 (A) exhibits the analytically calculated eigenvalues for a 3D homogeneous crystal with $\epsilon = 1$ and $\mu = 1$.

Bibliography

[1] K. Busch, M. König, and J. Niegemann, "Discontinuous Galerkin methods in nanophotonics," Laser Photon. Rev. **5**, 773 (2011). 115, 116

[2] C. Hafner, "Boundary methods for optical nano structures," Phys. Stat. Sol. B **244**, 3435 (2007). 115

[3] L. Li, "Use of Fourier series in the analysis of discontinuous periodic structures," J. Opt. Soc. Am. A **13**, 1024 (1996). 115

[4] L. Li, "New formulation of the Fourier modal method for crossed surface-relief gratings," J. Opt. Soc. Am. A **14**, 2758 (1997). 115

[5] S. G. Johnson and J. D. Joannopoulos, "Block-iterative frequency-domain methods for Maxwell's equations in a planewave basis," Opt. Express **8**, 3 (2001). 115, 129, 130

[6] A. Taflove and S. C. Hagness, *"Computational Electrodynamics: The Finite-Difference Time-Domain Method,"* (Artech House, Boston, 2005). 115

[7] K. S. Yee, "Numerical solution of initial boundary value problems involving Maxwell's equations in isotropic media," IEEE Trans. Antennas Propag. **14**, 302 (1966). 115

[8] A. Farjadpour, D. Roundy, A. Rodriguez, M. Ibanescu, P. Bermel, J. D. Joannopoulos, and S. G. Johnson, "Improving accuracy by subpixel smoothing in the finite-difference time domain," Opt. Lett. **31**, 2972 (2006). 115

[9] A. Deinega and I. Valuev, "Subpixel smoothing for conductive and dispersive media in the finite-difference time-domain method," Opt. Lett. **32**, 3429 (2007). 115

[10] A.F. Oskooi, C. Kottke, and S. G. Johnson, "Accurate finite-difference time-domain simulation of anisotropic media by subpixel smoothing," Opt. Lett. **34**, 2778 (2009). 115

[11] A.F. Oskooi, D. Roundy, M. Ibanescu, P. Bermel, J.D. Joannopoulos, and S.G. Johnson, "MEEP: A flexible free-software package for electromagnetic simulations by the FDTD method," Comput. Phys. Commun. **181**, 687 (2010). 115

[12] P. Monk, "A finite element method for approximating the time-harmonic Maxwell equations," Numer. Math. **63**, 243 (1992). 115

[13] J. -M. Jin, *"The finite element method in electromagnetics,"* (Wiley, 1993). 115

[14] S. Caorsi, P. Fernandes, and M. Raffetto, "On the convergence of Galerkin finite element approximations of electromagnetic eigenproblems," SIAM J. Numer. Anal. **38**, 580 (2000). 115, 119

[15] P. Monk and L. Demkowicz, "Discrete compactness and the approximation

of Maxwell's equations in $\mathbb{R}^3$," Math. Comp. **70**, 507 (2001). 115

[16] L. Demkowicz and L. Vardapetyan, "Modeling of electromagnetic absorption/scattering problems using hp-adaptive finite elements," Comput. Methods Appl. Mech. Eng. **152**, 103 (1998). 115, 119

[17] L. Vardapetyan and L. Demkowicz, "hp-adaptive finite elements in electromagnetics," Comput. Methods Appl. Mech. Eng. **169**, 331 (1999). 115, 119, 121

[18] F. Ihlenburg and I. Babuška, "Finite element solution of the Helmholtz equation with high wave number, Part I: The h-version of the FEM," Comput. Math. Appl. **30**, 9 (1995). 115

[19] F. Ihlenburg and I. Babuška, "Finite element solution of the Helmholtz equation with high wave number, Part II: The h-p version of the FEM," SIAM J. Numer. Anal. **34**, 315 (1997). 115

[20] M. Costabel and M. Dauge, "Singularities of electromagnetic fields in polyhedral domains," Arch. Ration. Mech. Anal. **151**, 221 (2000). 115

[21] D. Arnold, "An interior penalty finite element method with discontinuous elements," SIAM J. Numer. Anal. **19**, 742 (1982). 115, 125

[22] D. N. Arnold, F. Brezzi, B. Cockburn, and L. D. Marini, "Unified analysis of discontinuous Galerkin methods for elliptic problems," SIAM J. Numer. Anal. **39**, 1749 (2002). 115

[23] I. Perugia, D. Schötzau, and P. Monk, "Stablized interior penalty methods for the time-harmonic Maxwell equations," Comput. Methods Appl. Mech. Eng. **191**, 4675 (2002). 115, 119, 125

[24] I. Perugia and D. Schötzau, "The hp-local discontinuous Galerkin method for low-frequency time-harmonic Maxwell equations," Math. Comp. **72**, 1179 (2003). 115

[25] P. Houston, I. Perugia, and D. Schötzau, "hp-DGFEM for Maxwell's equations," pp. 785 - 794 in F. Brezzi, A. Buffa, S. Corsaro, and A. Murli, *"Numerical mathematics and advanced applications,"* (Springer-Verlag, New York, 2001). 115

[26] P. Houston, I. Perugia, and D. Schötzau, "Mixed discontinuous Galerkin Approximation of the Maxwell Operator," SIAM J. Numer. Anal. **42**, 434 (2004). 115, 119, 121, 125

[27] J. C. Nédélec, "Mixed finite elements in $\mathbb{R}^3$," Numer. Math. **35**, 315 (1980). 120

[28] Z. Lu, A. Cesmelioglu, J. J. W. van der Vegt, and Y. Xu, "Discontinusous Galerkin approximations for computing electromagnetic Bloch modes in photonic crystals," J. Sci. Comput. **44**, 219 (2010). 116, 120, 121, 125, 127, 128

[29] D. Sàrmàny, F. Izsàk, and J. J. W. van der Vegt, "Optimal penalty parameters for symmetric discontinuous Galerkin discretisations of the time-harmonic Maxwell equations," J. Sci. Comput. **44**, 219 (2010). 115, 125, 129

[30] J. D. Joannopoulos, S. G. Johnson, J. N. Winn, and R. D. Meade, *"Photonic crystals: Molding the flow of light,"* (Princeton University Press, Princeton NJ, 2008). 116, 117, 118, 127

[31] K. M. Leung, "Plane-wave calculation of photonic band structure," p. 269

in "Photonic band gaps and localization," edited by C. M. Soukoulis, NATO Advanced Research Studies on Localizations and Propagations (Plenum Press, New York, 1993). 116

[32] D. J. Griffiths, *"Introduction to electrodynamics,"* (Prentice Hall, Upper Saddle River NJ, 1999). 116

[33] L. Pesch, A. Bell, W.E.H. Solie, V.R. Ambati, O. Bokhove, and J.J.W. van der Vegt, "hpGEM — A sofware framework for discontinuous Galerkin finite element Methods," ACM Trans. Math. Softw. **33**, 1 (2007). 129

[34] S. Balay, W. D. Gropp, L. C. McInnes, and B. F. Smith, "Efficient Management of Parallelism in Object Oriented Numerical Software Libraries," in "Modern Software Tools in Scientific Computing," edited by E. Arge, A. M. Bruaset, and H. P. Langtangen, p163–202 (Birkhäuser Press, Switzerland, 1997). 129

[35] V. Hernandez, J.E. Roman, and V. Vidal, " SLEPc: A scalable and flexible toolkit for the solution of eigenvalue problems," ACM Trans. Math. Softw. **31**, 351 (2005). 129

[36] M. Ainsworth and J. Coyle, "Hierarchic finite element bases on unstructured tetrahedral meshes," Int. J. Numer. Meth. Eng. **58**, 2103 (2003). 129

[37] S. G. Johnson and J. D. Joannopoulos, "Block-iterative frequency-domain methods for Maxwell's equations in a planewave basis," Opt. Express **8**, 3 (2001). 115, 129, 130

[38] Throughout this chapter, we express frequency as a reduced frequency $\tilde{\omega} = \omega a/(2\pi c')$), with ω the frequency, a the lattice parameter, c' the speed of light that is not to be confused with the lattice parameter c. In this definition, the reduced frequency $\tilde{\omega}$ is expressed in units of (a/λ). 129, 130

5

CHAPTER 6
Summary and outlook

In order to understand light-matter interactions in complex nanophotonic systems, it is crucial to accurately model light at the nanoscale. This thesis, therefore, studies light propagation in experimentally relevant 3D periodic photonic nanostructures with several types of disrupted symmetries. We investigate unintentional symmetry-disruption, such as finite size and material absorption, as well as intentional symmetry-disruption, such as a point defect. Once our numerical models are validated with respect to analytical models, we interpret our results using the fundamental laws of physics. All results are presented in well-defined reduced units and their corresponding experimentally employed units. In order to move the computational modeling of light propagation in nanophotonic media forward, we present our work on developing a software tool employing a novel numerical method.

We have started with accurately computing the optical properties of a 3D photonic band gap crystal with finite support, which has two interfaces and hence disrupted symmetries. We observe that the stop band hardly changes with incident angle, which supports the experimental notion that strong reflectivity peaks measured with a large numerical aperture gives a faithful signature of the 3D band gap. We observe an intriguing hybridization of the Fabry-Pérot resonances and the Brewster angle in our calculations, which seems a characteristic property of 3D photonic band gap crystals. We assessed previously invoked experimental limitations to reflectivity, such as crystal thickness, angle of incidence, and Bragg attenuation length, and find that they are not very compelling. From the intense reflectivity peaks, we infer that the maximum reflectivity observed in the experiments is not limited by the finite size of the crystal. Our calculated polarization-resolved reflectivity spectra show that the frequency ranges of the s- and p-stop bands agree well with the corresponding stop gaps in the photonic band structure. We find that the Bragg attenuation lengths in the stop bands are smaller than earlier estimates based on the width of the stop band by a factor of 6 to 9. The comparison between angle-independent numerical calculations and experimental results provides an improved interpretation of the reflectivity measurements and new insight in the crystal structure (unequal pore sizes in different directions). Consequently, our numerical study provides an improved understanding of the experimental studies.

Building on our understanding of finite-size effects, we have investigated a 3D photonic band gap crystal with finite support as a potential back reflector to a thin silicon film in the visible regime. For an experimentally relevant study, we

have implemented the refractive index of real silicon, including dispersion and absorption. We observe that a 3D inverse woodpile photonic crystal enhances the absorption of a thin silicon film by (i) behaving as a perfect reflector, exhibiting nearly 100% reflectivity in the stop bands, as well as (ii) generating guided resonant modes at many discrete wavelengths. For a 2400 nm thin silicon film, our absorption results show nearly 2.6 times enhanced frequency-, angle-, polarization-averaged absorption between $\lambda = 680$ nm and $\lambda = 890$ nm. We find that the optical absorption is enhanced by positioning an inverse woodpile back reflector at the back end of a thin silicon film, which will keep the length of the solar cell unchanged and make the thin film solar cell lighter. For a sub-wavelength thin absorbing layer with a photonic crystal back reflector, we identify and demonstrate two physical mechanisms causing the giant absorption enhancement at discrete wavelengths: (i) a guided resonance due to the Bragg attenuation length and (ii) confinement due to a surface-defect.

To understand the impact of resonant cavities, we have modeled a point defect inside a 3D inverse woodpile photonic band gap crystal with finite support. We find a large electric-field energy enhancement at the cavity resonances. By comparing resonance bands in the band structure for an infinite crystal and troughs in the reflectivity spectra for a finite crystal, we identify cavity resonances and their field patterns. Out of five observed cavity resonances, one is s-polarized and four are p-polarized. These cavity resonances are angle-independent, indicating a strong confinement of light in the crystal slab. The P1, P2, and P4 resonances reveal normal behavior with single cross-correlation peaks (between field distributions) and single reflectivity resonances. The P3 and S1 resonances in finite crystals reveal an intriguing splitting into 2 sub-resonances, for which we have currently no explanation. We observe Fano resonances below the band gap due to the electromagnetic interference between the discrete contribution of the fundamental cavity mode and the continuum contribution of the light scattered by the photonic crystal. Our results indicate that 3D photonic band gap crystals with resonant cavities are interesting candidates for the absorbing medium of a solar cell in order to enhance the photovoltaic efficiency. Consequently, our analysis of the resonant cavity provides a novel insight in various resonances appearing due to locally disrupted lattice symmetry in 3D periodic photonic nanostructures.

Finally, we have developed a novel solver using the discontinuous Galerkin finite-element method (DGFEM) for the time-harmonic Maxwell equations with periodic dielectric materials. For accurate eigenvalue computations, we have explicitly implemented the divergence constraint.

Based on this thesis, we present the following outlook for further studies:

1. In order to understand the frequency dependence of finite-size effects, the Bragg attenuation length versus frequency should be calculated in the stop bands from transmission versus crystal thickness in the limit of large thickness. With these data, the known-how will advance on stop bands beyond Bragg stacks.

2. In order to further improve the match of our numerical model with the reflectivity experiments, one should study a crystal having finite size in all

three dimensions. However, since such a calculation requires 1000 times greater resources one needs to employ a memory-efficient version of the numerical method, while maintaining the convergence to a correct numerical result.

3. We have observed an intriguing hybridization of Fabry-Pérot resonances and the Brewster angle, which has not yet been observed in experiments. As an answer to the scientific challenge of light selectivity, this hybridization effect can be measured and employed as an optical filter for frequency- and angle-selectivity.

4. We found that positioning an inverse woodpile back reflector at the back surface of a thin silicon film enhances the optical absorption, keeps the length of the solar cell unchanged, and makes the thin film solar cell lighter. However, it is a generally advised regarding thin silicon film solar cells to not etch features directly into the active region. Therefore, experimental and numerical studies are needed to ascertain the impact of fabricating a 3D inverse woodpile photonic crystal back reflector in a thin silicon film on the overall photovoltaic efficiency.

5. To enhance the absorption of light over a wavelength range broader than reported in this thesis, we propose to employ a 3D inverse woodpile photonic crystal with the light incident in the ΓY direction as a back reflector for a thin film since the ΓY stop gap is about $1.3\times$ broader than the ΓZ or symmetry-related ΓX stop gap.

6. The stop gap of an inverse woodpile crystal depends on the lattice parameters and gives perfect reflectivity, provided the Bragg attenuation length of an inverse woodpile crystal is smaller than the absorption length of silicon. Therefore, one can investigate a novel back reflector consisting of a series of inverse woodpile crystals with varying lattice parameters and different stop gaps to enhance the absorption over a broad wavelength range, which will be the combination of individual stop gaps.

7. We observed that a 3D inverse woodpile photonic crystal with a resonant cavity is a nearly 80% light-weight candidate for the absorbing medium of a solar cell in order to enhance the photovoltaic efficiency at multiple discrete frequencies in the visible regime. Since an inverse woodpile photonic crystal has a large surface area per unit cell compared to a thin silicon film, an efficient numerical model needs to be developed to ascertain the surface recombination factor before predicting the photovoltaic efficiency enhancement.

8. In order to compute reflectivity spectra, the Div-DGMax code needs to be supplemented by the implementation of absorbing boundaries.

6

Nederlandse samenvatting

Om de licht-materie interactie in complexe fotonische systemen te begrijpen, is het heel belangrijk om licht nauwkeurig te modelleren op de nanoschaal. Dit proefschrift bestudeert daarom lichtvoortplanting in experimenteel relevante 3D periodieke fotonische nanostructuren met verstoorde symmetrieën. We onderzoeken onbedoelde symmetrie verstoording, zoals eindige grootte en materiële absorptie, als ook intentionele symmetrie verstoording, zoals een puntdefect. Nadat onze numerieke modellen zijn gevalideerd in vergelijking tot analytische modellen, interpreteren we onze resultaten met behulp van de fundamentele wetten van de natuurkunde. Alle resultaten worden gepresenteerd in helder gedefinieerde gereduceerde eenheden en hun overeenkomstige experimentele eenheden. Om de computationele modellering van lichtvoortplanting in nanofotonische media te verbeteren, presenteren wij ons werk omtrent het ontwikkelen van een software-gereedschap die gebruik maakt van een nieuwe numerieke methode.

We zijn begonnen met het nauwkeurig berekenen van de optische eigenschappen van een 3D fotonische band gap kristal met eindige dikte en twee grensvlakken en daarom verstoorde symmetrieën. We nemen waar dat de stop band nauwelijks varieert met de invalshoek, hetgeen de experimentele opvatting ondersteunt dat sterke reflectiviteitspieken die gemeten zijn met een grote numerieke apertuur ons een betrouwbare signatuur van de 3D band gap geven. We nemen een intrigerende hybridisatie waar van de Fabry-Pérot resonanties en de Brewsterhoek, die een karakteristieke eigenschap van 3D fotonische band gap kristallen lijkt te zijn. We hebben in het verleden genoemde beperkingen van de reflectiviteit beoordeeld, zoals de dikte van het kristal, de invalshoek en de Bragg verval lengte. Uit de intense reflectiviteitspieken leiden we af dat de maximale waargenomen reflectiviteit in de experimenten niet beperkt wordt door de eindige grootte van het kristal. Onze berekende polarisatie-omvattende reflectiviteitsspectra laten zien dat de frequentiebereiken van de s- en p-stop banden goed overeenkomen met de overeenkomstige stop gaps in de fotonische bandstructuur. We vinden dat de Bragglengten in de stop banden een factor 6 tot 9 kleiner zijn dan eerdere schattingen gebaseerd op de breedte van de stop band. De vergelijking tussen hoek-onafhankelijke numerieke berekeningen en experimentele resultaten geeft een verbeterde interpretatie van de reflectiviteitsmetingen en een nieuw inzicht in de kristalstructuur namelijk ongelijke poriegroottes in verschillende richtingen. Daarom geeft ons numerieke onderzoek een nieuw en verbeterd inzicht in de experimentele studies.

Voortbouwend op ons inzicht in eindige grootte effecten, hebben we een 3D fotonische band gap kristal met eindige grootte onderzocht als een potentiële

reflector voor een dun laagje silicium in het zichtbare frequentie bereik. Om een experimenteel relevante studie te bewerkstelligen, hebben we de brekingsindex van echt silicium gebruikt, met inbegrip van dispersie en absorptie eigenschappen. We nemen waar dat voor een 3D inverse woodpile fotonisch kristal de absorptie van een dun laagje silicium verhoogd wordt door (i) zich te gedragen als een perfecte reflector, die bijna 100% reflectie vertoont in de stop banden, alsook (ii) geleide resonerende modes te genereren bij vele discrete golflengtes. Voor een 2400 nm dunne laag silicium laten, onze absorptie-resultaten een bijna 2.6 maal verhoogde frequentie-, hoek- en polarisatie-gemiddelde absorptie zien tussen $\lambda = 680$ nm en $\lambda = 890$ nm. We vinden dat de fotovoltaïsche efficiëntie verhoogd wordt door een inverse woodpile reflector te plaatsen aan de achterkant van een dunne laag silicium, terwijl de dikte van de zonnecel gelijk blijft en de dunne-laag zonnecel lichter maakt. Voor een sub-golflengte dunne absorberende laag met een fotonisch kristal back-reflector, identificeren en demonstreren we twee fysieke mechanismen die deze gigantische verhoging veroorzaken bij discrete golflengten: (i) een geleide resonantie door de Bragg verval lengte en (ii) ruimtelijke beperking door een oppervlakte-defect.

Om de invloed van resonerende trilholtes te begrijpen, hebben we een puntdefect binnen een 3D fotonische band gap kristal met eindige dikte gemodelleerd. We vinden een grote verhoging van de elektrische-veld energie bij de trilholte-resonanties. Door resonantiebanden in de bandstructuur voor een oneindig kristal en de dalen in de reflectiviteitsspectra voor een eindig kristal te vergelijken, identificeren we trilholte-resonanties en hun veldpatronen. Van de vijf waargenomen trilholte-resonanties, is er één s-gepolariseerd en zijn er vier p-gepolariseerd. Deze trilholte-resonanties zijn hoek-onafhankelijk, hetgeen duidt op een sterke ruimtelijke beperking van het licht in het fotonisch kristal. De P1, P2 en P4 resonanties laten normaal gedrag zien met enkelvoudige kruiscorrelatiepieken (tussen de veldverdelingen) en enkelvoudige reflectiviteitsresonanties. De P3 en S1 resonanties in eindige kristallen laten een intrigerende splitsing zien in 2 subresonanties, waarvoor we op dit moment geen verklaring hebben. We nemen Fano resonanties waar onder de band gap door de elektromagnetische interferentie tussen de discrete bijdrage van de fundamentele trilholte mode en de continuum bijdrage van het licht dat verstrooid wordt door het kristal. Onze resultaten geven aan dat 3D fotonische band gap kristallen met resonerende trilholtes interessante kandidaten zijn voor het absorberend medium van een zonnecel om zodoende de fotovoltaïsche efficiëntie te verhogen. Onze analyse van de resonerende trilholte geeft daarom een nieuw inzicht in de diverse resonanties die ontstaan door plaatselijk onderbroken rooster-symmetrie in 3D periodieke fotonische nanostructuren.

Tot slot hebben we een nieuwe computerprogramma ontwikkeld dat gebruik maakt van de discontinue Galerkin eindige-elementen methode (DGFEM) voor de tijdharmonische Maxwell vergelijkingen met periodieke diëlektrische materialen. Voor nauwkeurige eigenwaarde-berekeningen, hebben we expliciet de divergentie-beperking opgelegd.

Op basis van dit proefschrift presenteren wij de volgende suggesties voor verder onderzoek:

1. Om de frequentie-afhankelijkheid van eindige-grootte effecten beter te begrijpen, kan men de Bragglengte berekenen ten opzichte van de frequentie in de stop banden op basis van de transmissie in de limiet van dikke kristallen.

2. Om de overeenkomst van ons numerieke model met de reflectiviteitsexperimenten verder te verbeteren, dient men een kristal te modelleren dat een eindige grootte heeft in alle drie dimensies. Aangezien dit véél meer rekencapaciteit vergt, dientmen echter een geheugen-efficiënte versie van de numerieke methode te gebruiken, waarbij de convergentie naar een juist numeriek resultaat behouden blijft.

3. We hebben een intrigerende hybridisatie van de Fabry-Pérot resonanties en de Brewsterhoek waargenomen, die nog niet waargenomen is in experimenten. Als antwoord op deze wetenschappelijke uitdaging van lichtselectiviteit kan deze hybridisatie gemeten worden en mogelijk gebruikt worden als een optisch filter voor frequentie- en hoeksensitiviteit.

4. We hebben gevonden dat het plaatsen van een inverse woodpile backreflector aan de achterkant van een dunne laag silicium de fotovoltaïsche efficiëntie verhoogt, de lengte van de zonnecel niet verandert, en de dunnelaag silicium zonnecel lichter maakt. Daarentegen is het over het algemeen niet aangeraden om voor dunne-laag silicium zonnecellen de kenmerken direct in het actieve gebied te etsen. Daarom zijn experimentele en numerieke studies nodig om te bepalen wat de invloed is van het fabriceren van een 3D inverse woodpile fotonisch kristal back-reflector in een dunne laag silicium op de algehele fotovoltaïsche efficiëntie.

5. Om de absorptie van licht te verhogen over een golflengte-gebied groter dan dat gerapporteerd is in dit proefschrift, stellen wij voor om een 3D inverse woodpile fotonisch kristal toe te passen waarbij het licht invalt in de ΓY richting als een back-reflector voor de een dunne laag silicium. De reden is dat de ΓY stop gap is ongeveer 1.3 breder dan de ΓZ of symmetriegerelateerde ΓX stop gap.

6. De stop gap van een inverse woodpile fotonisch kristal hangt af van de roosterparameters en geeft een perfecte reflectiviteit, als aangenomen wordt dat de Bragg verval lengte van een inverse woodpile fotonisch kristal kleiner is dan de absorptie-lengte van silicium. Daarom kan men een nieuwe reflector onderzoeken die bestaat uit een reeks van inverse woodpile fotonische kristallen met variërende rooster parameters en verschillende stop gaps om zodoende de absorptie over een breed golflengte-gebied te verhogen, hetgeen een resultaat zal zijn van de combinatie van de individuele stop gaps.

7. We hebben waargenomen dat een 3D inverse woodpile fotonisch kristal met een resonerende trilholte een bijna 80% lichtere kandidaat is voor het absorberend medium van een zonnecel om de fotovoltaïsche efficiëntie te verhogen bij meerdere discrete frequenties in het zichtbare gebied. Omdat een inverse woodpile groot oppervlak per eenheidscel heeft in vergelijking

N

met een dunne laag silicium, dient er een numeriek model ontwikkeld te worden om te bepalen wat de oppervlakte recombination factor is voordat de fotovoltaïsche efficiëntie verhoging voorspeld kan worden wordt.

8. Om reflectiviteitsspectra te berekenen, heeft de Div-DGMax code de implementatie van absorberende randen nodig.

Acknowledgements

"You there! Define sublimation", asks a high school teacher pointing to a shy kid, who is trying to hide behind the front row students. The obedient kid stands up, but remains tongue-tied with his eyes fixed to the floor. At age 10, he is clearly weak in learning, with no knowledge of any subject except intriguing numbers and geometries. "What does your father do? Your ...father..., *Papa kya karte hai*?,"comes the next question, which is asked by the teacher in a pacifying blend of English, Hindi, and hand gesture. Breaking silence in the classroom, the kid whispers in Hindi "*mere Papa science padhate hai*". Swiftly, the room fills with the loud voice of the high school teacher, analyzing how inferior the kid's father is, who teaches science to others and his own son can neither speak English nor explain the unique phase transition of sublimation. Unfortunately, the *delicate* analysis by the teacher is in English and the kid again understands nothing. Finding himself at the center of laughter among 50 classmates, answers finally sneak out of his eyes and roll down his cheeks. Foolish kid indeed! While it is scary how fast time flies, however, some memories last forever and navigate our lives. To quote J. K. Rowling, the writer of the Harry Potter series: *We've all got both light and dark inside us. What matters is the part we choose to act on. That's who we really are.* I, who happen to be that kid, am therefore immensely pleased to pen the final section of my PhD thesis in Mathematics and Physics.

Exhibiting only one name on the title page, this thesis would not have seen the light of day without direct and indirect contribution of several people. This section gives me an opportunity to acknowledge all those people.

It has been a stimulating experience to work in a joint research project of the Mathematics of Computational Science (MACS) and Complex Photonic Systems (COPS) groups. Both groups provide a unique environment, which accelerates the learning curve of a budding researcher. Furthermore, I learnt the skill to customize my presentations for Mathematicians as well as Physicists. I feel blessed to be mentored and trained by the duo of Jaap van der Vegt, a Mathematician, and Willem Vos, a Physicist. Jaap and Willem are exceptionally dedicated to research, *e.g.*, Jaap correcting last bits of equations on a very early morning before his long flight to China, and Willem ailing, but still correcting chapters on a late Sunday night.

From helping on my first day in Enschede to teaching the art of numerical calculation, Jaap has been a backbone of my research life. He always reminded me of the importance of planning and advised to focus on one task at a time, while keeping an eye on the goal. Sometimes, he feels like a family doctor, whom different students reach out for different numerical problems. Many times, I

A